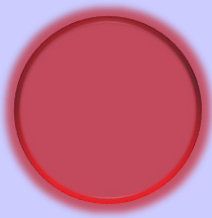# Spatiotemporal mapping

of lipid and protein oxidation

in food emulsions

Suyeon Yang

Propositions

1. Sub-micron resolution microscopy holds tremendous potential for elucidating the relationship between lipid oxidation and proteins at colloidal interfaces.
   (this thesis)

2. Spatiotemporal mapping is the most promising tool for revealing mass transport phenomena in lipid oxidation.
   (this thesis)

3. Scientific quality is jeopardized by monetary compensation to chair groups for PhD graduations.

4. Artificial intelligence will make psychotherapists redundant.

5. Apologies for historical events that caused injustice and suffering are meaningless if individual victims are not recognized.

6. Taxing feminine hygiene products (*tampon tax*, Crawford 2017) is a discriminatory practice.

Propositions belonging to the thesis, entitled

Spatiotemporal mapping of lipid and protein oxidation in food emulsions

Suyeon Yang
Wageningen, 1 September 2023

Spatiotemporal mapping of lipid and protein oxidation in food emulsions

Suyeon Yang

Thesis committee

Promotors
Prof. Dr John P.M. van Duynhoven
Special professor, Magnetic Resonance in relation to Food
Wageningen University & Research

Dr Johannes Hohlbein
Associate professor, Laboratory of Biophysics
Wageningen University & Research

Other members
Prof. Dr Joris H.B. Sprakel, Wageningen University & Research
Dr Lorenzo Albertazzi, Eindhoven University of Technology
Dr Pierre Villeneuve, CIRAD, Montpellier, France
Prof. Dr Niklas Lorén, RISE, Göteborg, Sweden

Spatiotemporal mapping of lipid and protein oxidation in food emulsions

Suyeon Yang

Thesis

submitted in fulfilment of the requirements for the degree of doctor

at Wageningen University

by the authority of the Rector Magnificus,

Prof. Dr A.P.J. Mol,

in the presence of the

Thesis Committee appointed by the Academic Board

to be defended in public

on Friday 1 September 2023

at 1:30 p.m. in the Omnia Auditorium.

Contents

1

General Introduction

1.1 Oil-in-water (O/W) food emulsions

Lipids play crucial roles in the functioning of human bodies such as moving and storing energy. Moreover, they provide structure and compartments to cells and tissues[1]. Some lipids, such as omega-3 and omega-6 fatty acids, are essential to our diet as they cannot be synthesized by our bodies. These fatty acids play important roles in several physiological processes, including the regulation of blood pressure, inflammation, and blood clotting[2]. Furthermore, consuming a diet high in healthy fatty acids, such as monounsaturated and polyunsaturated fatty acids (PUFAs), has been linked to a reduced risk of developing chronic diseases like heart disease, stroke, and type 2 diabetes[3,4]. In food products, PUFAs often exist in the oil phase of oil-in-water (O/W) emulsions, such as mayonnaise, salad dressing, and milk. Due to the immiscibility of the phases, O/W emulsions require emulsification, which involves high shear mixing and the addition of emulsifiers to stabilize the droplet interfaces. Oil droplets tend to have a spherical shape when dispersed in water to minimize the contact area between the oil and water phases[5,6]. Due to the thermodynamically unfavorable contact between oil and water molecules, the Laplace pressure (ΔP_L) arises from the interfacial tension between the inside (oil phase) and the outside (water phase) of droplets. The Laplace pressure can be expressed as[5]

$$\Delta P_L = \frac{4\gamma}{d} ,\qquad(1.1)$$

where γ (N/m) is the oil-water interfacial tension and d is the diameter of the oil droplets. During emulsification, the rapid adsorption of emulsifiers at the oil droplet surfaces reduces the interfacial tension (γ). Consequently, smaller oil droplets are generated when the disruptive stresses generated during homogenization exceed ΔP_L[7–9].

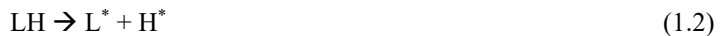### 1.1.1 Mechanisms of lipid oxidation

For oil-in-water food emulsions, lipid oxidation leads to the deterioration in the taste, texture, and nutritional content[10], thus impacting quality and shelf-life. Especially edible vegetable oils that contain unsaturated fatty acids featuring double bonds in the chain are prone to oxidation as their lower dissociation energy of the C-H bond makes the abstraction of hydrogen easier[11]. Having multiple unsaturated bonds in a fatty acid further enhances the rates of lipid oxidation[12].

Auto-oxidation is considered the primary lipid oxidation process in oil-in-water food emulsions. Auto-oxidation can occur in the presence of oxygen at any temperature above the freezing point of lipids. The reaction between unsaturated lipids and oxygen is a free radical chain reaction, often described as three stages; initiation, propagation, and termination[13]. In the initiation stage, oxidation begins with the abstraction of a hydrogen atom from the first carbon atom next to the double bond (**Equation. 1.2**). This reaction rarely occurs spontaneously because it has a high

activation energy[14,15]. Therefore, fatty acid oxidation is mainly initiated by the presence of heat or initiators. At this stage, lipid oxidation remains slow due to fewer lipid radicals (L^*) being available that can react with the present oxygen (O_2). Moreover, the rate constant of this reaction is typically at least ten times lower than the rate constant of reactions that occur during the propagation stage[16].

In the propagation stage, the rate of oxidation increases as more lipid radicals (L^*) are formed and more oxygen is consumed, resulting in the generation of lipid peroxyl radicals (LOO^*) (**Equation 1.3**)[17]. Since peroxyl radicals (LOO^*) have higher bond dissociation energy than lipid radicals (L^*) due to the presence of the unstable oxygen-oxygen bond in peroxyl radicals, they can abstract hydrogen atoms from another unsaturated fatty acid ($L'H$) to produce hydroperoxides (LOOH) and new lipid radicals (**Equation 1.4**). Evaluation of lipid oxidation is often determined in this propagation stage by measuring the concentration of hydroperoxides[18,19], spin trapped free radicals[20,21], or the determination of the peroxide value (POV)[22]. Finally, in the termination stage, radicals react with each other and form stable nonradical compounds that can no longer participate in the reaction cycle (**Equation 1.5**).

Initiation

$$LH \rightarrow L^* + H^* \qquad (1.2)$$

Propagation

$$L^* + O_2 \rightarrow LOO^* \qquad (1.3)$$

$$LOO^* + L'H \rightarrow LOOH + L'^* \qquad (1.4)$$

Termination

$$L^* + L^* \rightarrow LL, L^* + LOO^* \rightarrow LOOL,$$
$$LOO^* + LOO^* \rightarrow \text{non-radical products} \qquad (1.5)$$

Another factor that can influence the lipid oxidation mechanism in O/W emulsions is the presence of transition metals in the aqueous phase. In foods, concentrations of transition metals up to 1 mmol kg^{-1} have been reported[23]. Transition metal ions, especially those of iron and copper, can produce free radicals through Fenton reactions[24]. Among different species of metal ions, Fe^{2+} ion has the highest pro-oxidant effect. In the presence of transition metal ions, a direct reaction between unsaturated lipids (LH) and transition metal ions (M^{3+}) can occur (**Equation 1.6**). Alternatively, hydroperoxides can form lipid radicals by metal reduction (**Equations 1.7 and 1.8**). This metal-catalyzed decomposition of hydroperoxides can be a main source of radicals

in O/W emulsions. Also, lipid radicals can be generated from hydroperoxides by thermal degradation (**Equations 1.9** and **1.10**).

In the presence of metal ions

$$LH + M^{3+} \rightarrow L^* + H^+ M^{2+} \tag{1.6}$$

$$LOOH + M^{2+} \rightarrow LO^* + H^* + M^{3+} \tag{1.7}$$

$$LOOH + M^{3+} \rightarrow LOO^* + H^* + M^{2+} \tag{1.8}$$

Thermal decomposition

$$LOOH \rightarrow LO^* + {}^*OH \tag{1.9}$$

$$2LOOH \rightarrow LO^* + H_2O + LOO^* \tag{1.10}$$

1.1.2 Lipid-protein co-oxidation at the interfacial region

Within oil-in-water food emulsions, three distinct spatial regions can be discerned: oil phase, aqueous phase, and interface. In the oil phase, lipid oxidation, including the reaction with transition metal ions (M^{2+}, M^{3+}), has been studied for decades, as described above[19,25]. The composition of, and possible oxidation mechanisms within the aqueous phase are also gaining more research attention[26–29] because it includes non-adsorbed emulsifiers and oxidation initiators such as transition metal ions and antioxidants[12,30]. Especially, proteins that act as emulsifiers in oil-in-water food emulsions are known to have antioxidant roles since they are capable of scavenging free radicals[30–33] or binding to the metal ions above their isoelectric point, thus retarding lipid oxidation[33,34]. Finally, the interest in studying interfacial properties has increased[12,35,36] as it can alter the oxidation speed at the oil-water interface where pro-oxidants such as transition metals come into contact with hydroperoxides[12,29].

At the droplet interface, proteins can co-oxidize with lipid substrates. In the presence of lipid peroxyl radicals (LOO*), radical transfer to proteins take place (**Equation 1.11**). By scavenging free radicals from lipids, proteins (PH) can delay the free radical chain propagation process in lipid oxidation[37].

$$LO(O)^* + PH \rightarrow LO(O)H + P^* \tag{1.11}$$

In addition, proteins can bind transition metals, preventing them from inhibiting the radical formation and decomposition of surface-active hydroperoxides (**Figure 1.1**). When free radicals and unbound metal ions reach the interface to react with unsaturated fatty acids, adsorbed proteins can quench the free radicals and chelate metal ions. The protein radicals (P^*) also react with other proteins, lipids, and other molecules like vitamins (**Equation 1.12**). Moreover,

protein radicals also react with oxygen molecules and produce protein hydroperoxides resulting in peptide scission and side chain oxidation (**Equation 1.13**). The aggregation of proteins that alters protein conformation and solubility occurs since protein radical species are reactive (**Equation 1.14**). The methods for detection of protein oxidation will be described later in this Chapter.
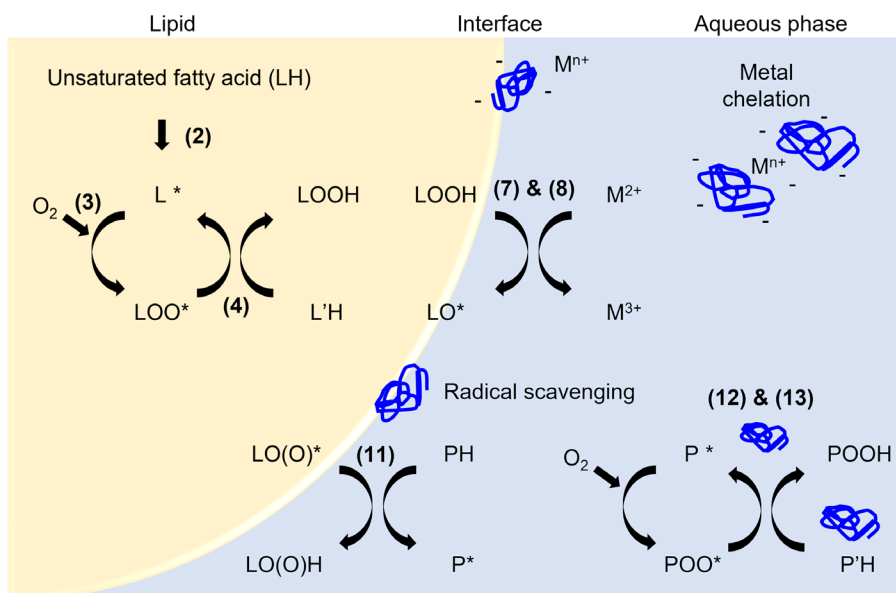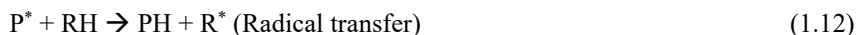
$$P^* + RH \rightarrow PH + R^* \text{ (Radical transfer)} \tag{1.12}$$

$$P^* + O_2 \rightarrow POOH \rightarrow PO^* \rightarrow P\text{-}C\text{=}O \text{ (Oxidation)} \tag{1.13}$$

$$P^* + P^* \rightarrow PP, \; P^* + PO_2^* \rightarrow POOP \text{ (Aggregation)} \tag{1.14}$$

Figure 1.1. Schematic figure of lipid and protein oxidation in oil-in-water food emulsions. Lipid oxidation is initiated by hydrogen abstraction from unsaturated fatty acid (LH). Then, lipid radicals (L*) react with oxygen molecules (O$_2$), leading to peroxyl radicals (LOO*). LOO* can react with other unsaturated fatty acids (L'H) and produce surface active hydroperoxides (LOOH) molecules. The surface-active molecules, LOOH, located at the interface react with metal ions (M^{2+}) from the aqueous phase. Proteins (PH) at the interface can scavenge the free radicals from lipids. Moreover, proteins in the continuous phase can chelate metal ions and react with oxygen.

1.1.3 Physiochemical parameters that influence lipid oxidation

Understanding the properties of the interfacial layer surrounding the droplets is of importance as initial reactions take place there. Among the many parameters influencing lipid oxidation, pH and droplet size are the most pronounced. The pH of the emulsions can influence the charge, solubility, and stability of emulsions[12,17]. For instance, in protein-stabilized emulsions, proteins

are negatively charged at a pH higher than the isoelectric point of proteins, attracting pro-oxidant metals at the interface and promoting lipid oxidation[12].

As another critical lipid oxidation parameter, droplet size determines the interfacial area that is intact with the aqueous phase[12]. The surface area (A) of the droplet in an emulsion is proportional to the dispersed phase volume fraction ($\emptyset$) and reciprocal of the surface-volume mean diameter (d_{32}), which is related to the average surface area of droplets exposed to the continuous phase per unit volume of emulsions (**Equation 1.15**)[6].

$$A = \frac{6\emptyset}{d_{32}} \qquad (1.15)$$

For instance, in a 10% oil-in-water emulsion with 1 μm diameter sized droplets, the total surface area of the lipid phase exposed to the aqueous phase is 10 times larger than the surface area of a 10% emulsion with 10 μm droplets[35].

1.1.4   Transport mechanism during lipid oxidation

In oil-in-water emulsions, lipid oxidation is primarily an interfacial phenomenon since the interface is the contact region between unsaturated lipid targets (in the droplet phase) and pro-oxidant compounds, such as metal ions in the aqueous phase. It is, however, still unclear how oxidation spreads throughout the system. Here we describe two suggested mass transport pathways[17,38].

One possible way of accelerating lipid oxidation between droplets is the diffusion of lipid-derived free radicals from one particle to another (**Figure 1.2a**). Thus it is important to consider the short life span of lipid radicals. The relationship between distance and time for diffusion can be described as **Equation 1.16**.

$$x = \sqrt{2Dt_{1/2}}, \qquad (1.16)$$

where x is the average distance of diffusion, D is the diffusion coefficient, and $t_{1/2}$ is the half-life of the intermediate. Considering that the half-life span of alkoxyl radicals is 10^{-6} s in oil and the diffusion coefficient is $5 \cdot 10^{-5}$ cm^2/s for non-viscous media (water phase) and $1 \cdot 10^{-10}$ cm^2/s for viscous media (oil phase), the possible diffusion distance (x) of alkoxyl radicals in the intermediate between viscous and non-viscous media is less than 0.1 μm[39,40], which does not allow them to transfer from one lipid droplet to another.

For peroxyl radicals, the half-life span is 0.5-7 s in the oil substrate[17] and longer travel in the range of 0.2 (viscous media) to 100 μm (non-viscous media) is possible depending on the viscosity of media as media will change the diffusion coefficient[38]. Although their diffusion behavior is favorable, hydrophobicity and low solubility may prohibit transfer to other oil droplets.

The second possible route is micelle-assisted transfer[17,38] (**Figure 1.2b**). In oil-in-water food emulsions, the amount of emulsifiers used often exceeds the amount needed to cover the interface of the droplets[12], leading to an excess of unadsorbed surfactants in the aqueous phase. When the concentration of unadsorbed surfactants in the aqueous phase is higher than their critical micelle concentration (CMC), they can form surfactant micelles acting as carriers to transfer antioxidants, hydroperoxides and iron from the oil phase to the aqueous phase and/or the interface. Especially when LOOHs are present at the emulsion droplet interface, surfactant micelles can enable their transfer to other lipid droplets.
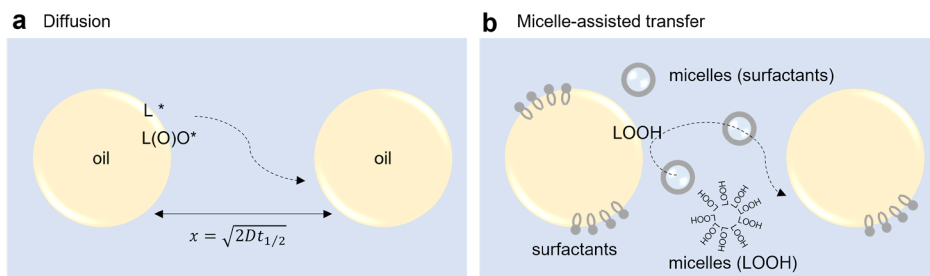

Figure 1.2. Possible pathways of mass transport. (**a**) Diffusion of lipid-derived radicals. The distance (x) of lipid alkyl radicals (L*) and peroxyl radicals (LOO*) during their life span can be calculated with the diffusion coefficient (D) and half-life span ($t_{1/2}$). The peroxyl radical might be transferred due to its relatively long half-span, but hydrophobicity may prohibit this. (**b**) Micelle-assisted transfer. At high concentrations of surfactants in the aqueous phase, micelles can be formed and act as carriers to transfer lipid-derived oxidants.

1.1.5   The complex case of mayonnaise

One of the most consumed oil-in-water (O/W) food emulsions is mayonnaise. The main ingredients of mayonnaise are vegetable oil, water, egg yolk, vinegar, and salt. Egg yolk, as the emulsifier in mayonnaise, has a complex composition[41] comprising lipoprotein particles and phosvitin as an iron-binding protein (**Figure 1.3**). Via the lipoproteins, strong emulsifiers such as apoproteins and phospholipids are introduced. Phosvitin is another protein with emulsifying capacity but also introduces iron ions, which can act as pro-oxidants[42,43]. As mayonnaise comprises multiple emulsifiers, the coverage of droplet interfaces is likely heterogeneous, both at the intra- as well as at the inter-droplet level. Since protein and phospholipid emulsifiers are abundant in the continuous aqueous phase of mayonnaise, they can also influence the transport of reactive oxidation intermediates, thus adding another level of complexity. Heterogeneity exists not only at the interface coverage level but also in droplet size distribution, which can also impact on the oxidation rate.
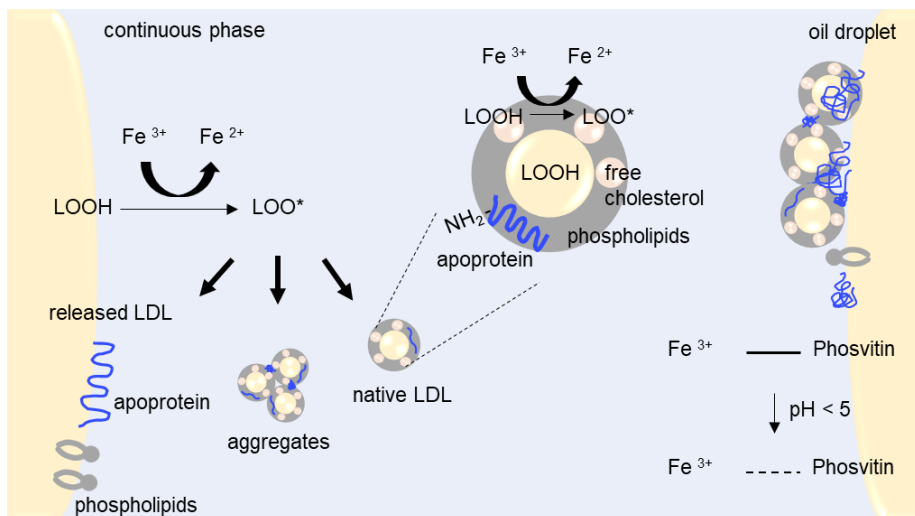
Figure 1.3. Schematic representation of the compositional and structural complexity of mayonnaise. Egg yolk is the main emulsifier in mayonnaise and introduces iron ions. In the presence of these transition metal ions, hydroperoxides can undergo iron-catalyzed decomposition, which boosts the overall rate of lipid oxidation. As a main ingredient of egg yolk, low density lipoprotein (LDL) particles are dispersed as phospholipids and apoproteins at the interface during the emulsification. Part of the LDL particles can stay intact and engage in their own lipid and protein oxidation mechanisms. The affinity of phosvitin for iron becomes weaker in acidic conditions (pH < 5).

1.1.6   Bulk measurements of oxidation products

Lipid and protein oxidation has been studied using many different detection methods. The most commonly used methods for detecting and assessing lipid oxidation are thiobarbituric acid-reactive substances (TBARS)[44,45], determining the peroxide value (POV)[22], nuclear magnetic resonance (NMR) spectroscopy[19,43], and electron spin resonance (ESR)[46]. Briefly, TBARS detects the level of malondialdehyde (MDA) which is one of the final products of polyunsaturated fatty acids peroxidation using thiobarbituric acid (TBA) as a reagent. TBA reacts with MDA, forming a pink or red-colored complex which is called TBARS. The absorbance of this complex can be measured using a spectrophotometer at a specific wavelength (usually at 532 nm). The absorbance is proportional to the amount of MDA or other aldehydes present. However, not all peroxidation reactions generate MDA, and TBA can react with other compounds, such as proteins and carbohydrates, thereby sometimes leading to false positive results. Assessment of the peroxide value is based on the reaction of peroxides with iodide ions in the presence of acid[47]. This reaction leads to the formation of iodine, which can be quantified by titration with a standardized solution of sodium thiosulfate. The amount of peroxides present in the sample is determined by the amount of iodine formed during the reaction, which is directly proportional to the concentration of peroxides in the sample. However, the lack of specificity in

POV measurements cannot distinguish between hydroperoxides and secondary products such as aldehydes[48]. NMR spectroscopy allows for determining the concentration of lipid oxidation products such as hydroperoxides and aldehydes. NMR spectroscopy can detect these lipid oxidation species simultaneously and is easy to automate, but results can be sensitive to the extraction steps used. ESR spectroscopy detects the unpaired electrons in radical species, providing high sensitivity and quantification of free radicals in the sample. The short lifetime of free radicals hampers detection, but this issue can be overcome by using spin traps[49], which results in stable adducts. On the other hand, spin trapping can perturb the oxidation reactions, thus biasing the view of overall mechanisms.

To determine protein oxidation and structural changes, measurements of the carbonyl content of proteins, intrinsic tryptophan fluorescence, and sodium dodecyl sulfate-polyacrylamide gel electrophoresis (SDS-PAGE) are often used. Protein carbonyl content can be calculated from the maximum absorbance using a UV-vis spectrophotometer with a carbonyl reagent, 2,4-dinitrophenylhydrazine (DNPH)[50]. Intrinsic tryptophan fluorescence uses the natural tryptophan fluorescence determined with a fluorescence spectrophotometer. Changes in tryptophan fluorescence indicate the potential conformational of proteins upon oxidation[51]. SDS-PAGE uses the electrophoretic pattern of non-oxidized and oxidized proteins from changes in molecular weights, conformation, and aggregation of proteins[52].

1.1.7   Localization of oxidation events

Bulk measurements of oxidation products mentioned above (**section 1.1.6**) can provide general and global oxidation information in both the oil and the water phase after separating the phase from the emulsion. However, these bulk measurement methods do not provide a view of local oxidation events, such as protein oxidation at the interface, lipid oxidation at the single droplet level, and the transport mechanism of oxidation products.

For further investigations on the spatial localization of oxidation products, the use of non-invasive optical microscopy methods provides the following advantages: (1) no extraction steps are required to study lipid and protein oxidation and the involvement of interfaces, (2) lipid and protein oxidation can be studied locally and in a time-dependent manner and (3) lipid and protein co-oxidation can be examined simultaneously.

Due to these advantages, the interest in using optical microscopy for food oxidation studies has increased[53–57]. Combination of optical microscopy with lipophilic oxidation-sensitive fluorescent dyes enabled the detection of radicals in single droplets[55] and provided evidence for the transfer of radicals between droplets[56]. Another study revealed the heterogeneous oxidation at interfaces using structured illumination microscopy (SIM)[57]. Despite the increasing interest,

studies on the spatiotemporal aspects of lipid and protein oxidation are still rare due to the lack of robust and validated measurement approaches.

In this thesis, I will tailor multiple microscopy techniques, such as standard confocal laser scanning microscopy (CLSM), re-scanning confocal microscopy (RCM), direct Stochastic reconstructed microscopy (dSTORM), and cryogenic correlative light and electron microscopy (cryo-CLEM) for the spatiotemporal assessment of lipid and protein oxidation in food emulsions. A more detailed explanation of these microscopic techniques will follow in **Chapter 2**.

1.2   Project Aim

In oil-in-water food emulsions, proteins and surfactants are often used as emulsifiers to stabilize the emulsion. As these emulsifiers can also act as anti-/pro-oxidants depending on their concentration, charge, and distribution at the interface[12,58], lipid oxidation should be studied in conjunction with protein oxidation. By assessing lipid and protein oxidation only globally (**section 1.1.6**), the view on the interplay between them at the interface remains limited as there is no clear evidence of whether it comes from the interface or the aqueous phase that includes unadsorbed proteins and pro-oxidants. Here, we will perform direct local assessments of lipid and protein oxidation to obtain a detailed view on the involved mechanisms. Local assessment can also provide clues for understanding the role of lipid transport by localizing the oxidation at the level of individual droplets and interfaces.

This thesis introduces and tailors new methodologies and assays for localizing lipid and protein oxidation using microscopic methods; the project aim is to improve the methodology for the local detection of early-stage lipid oxidation and provide insights into protein-lipid co-oxidation at the interface to enable rational design of strategies that delay food oxidation.

1.3   Outline of this thesis

This thesis describes the development and application of microscopic methodologies to detect local lipid and protein oxidation at multi-scale ranges. In **Figure 1.4**, we briefly show the thesis outline from Chapter 2 to Chapter 7. First, relevant microscopic techniques will be explained and discussed (**Chapter 2**), next lipid and protein oxidation will be studied at individual droplet levels in mayonnaise as polydisperse emulsions (**Chapter 3**), then protein oxidation will be assessed in the early and late stages of oxidation in mayonnaise (**Chapter 4**). Subsequently, lipid and protein oxidation in mono- and polydisperse model system will be discussed (**Chapter 5**). Then we will introduce a new correlative approach to assess lipid and protein co-oxidation in model emulsions (**Chapter 6**). Finally, a general discussion on our findings and an outlook will be presented (**Chapter 7**).
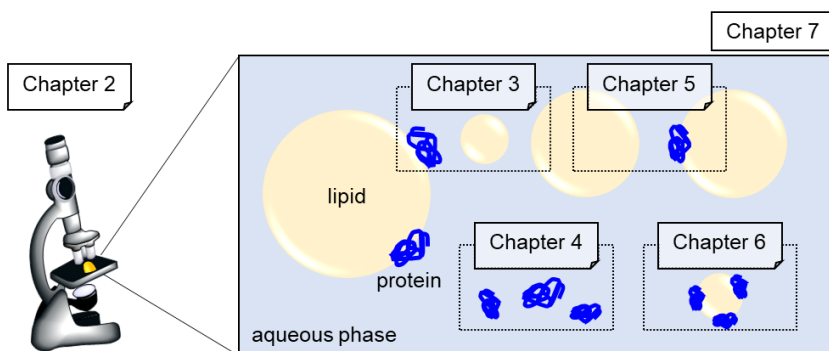
Figure 1.4. Overview of this thesis. Chapter 2 describes the principles and applications of microscopy to food oxidation studies, and Chapter 3 demonstrates the mapping of lipid and protein oxidation in the same oil droplets over many days using a tracking method. Chapter 4 introduces the newly developed fluorescent labeled spin trap, CAMPO-AFDye 647, for detecting protein oxidation in the early stage. In Chapter 5, the impact of droplet sizes, emulsifier types, and heterogeneity of proteins at the interface is evaluated in poly- and mono-disperse systems. Chapter 6 shows the feasibility of cryo-CLEM work for lipid oxidation and protein structural changes at the interface upon oxidation. In Chapter 7, the findings will be discussed and an outlook will be presented.

Chapter 2 describes the methodology for visualizing local lipid and protein oxidation events in food systems. Different types of fluorophores and microscope techniques for food oxidation studies will be introduced. The principles of standard and advanced microscopy techniques used in this thesis are explained, and applications to food oxidation studies are demonstrated.

Chapter 3 describes the mapping of local lipid and protein oxidation in mayonnaise. A new method for tracking the same oil droplets over 14 days will be introduced. Measurements of droplet specific oxidation rates will be performed by segmenting and tracking the same oil droplets over time. Moreover, the local pro-/anti-oxidant effects of L-ascorbic acid and α-tocopherol on lipids and proteins are investigated, as well as co-oxidation between lipids and proteins at the interface.

In **Chapter 4**, a newly developed water-soluble fluorescent labeled spin trap (CAMPO-AFDye 647) will be introduced to detect the early oxidation stage in dilute mayonnaise. As autofluorescence in proteins is only detectable at the late stage of oxidation, we will monitor the accumulation of the CAMPO-AFDye 647 fluorescent spin trap as a proxy of lipid oxidation in the early stage at the oil-water droplet interface. Moreover, low-density lipoprotein particles (LDLs) and their aggregates upon oxidation will be visualized using cryo-transmission electron microscopy (cryo-TEM) and bright field microscopy.

Chapter 5 continues the study of local lipid and protein oxidation in mono-/poly-disperse whey protein isolate (WPI)-stabilized emulsions. First, quantitative kinetic modeling will be used for mechanistic validation that the lipid oxidation sensitive dye (BODIPY 665/676) can be used as

a probe for local primary lipid oxidation. Next, we focus on finding the determining factors influencing lipid oxidation, such as the emulsification method impacting on the distribution of proteins at the interface and the droplet size distribution. Furthermore, the co-localization of lipid oxidation in oil droplets and protein oxidation at the oil-water interface will be visualized simultaneously.

In **Chapter 6**, we show the feasibility of visualizing lipid-protein co-oxidation at droplet interfaces using cryo-CLEM. This novel correlative imaging technique combines the ultra high-resolution achievable with electron microscopy (EM) and with the chemical specificity of fluorescence microscopy (FM) to provide clues for understanding the lipid-protein co-oxidation mechanism at the oil-water droplet interfacial region.

Chapter 7 describes a general discussion of the main findings in this thesis and the outlook for future microscopy work in food oxidation studies.

References

1. Calder, P. C. Functional Roles of Fatty Acids and Their Effects on Human Health. *J. Parenter. Enter. Nutr.* **39**, 18S-32S (2015).
2. Calder, P. C. Omega-3 Fatty Acids and Inflammatory Processes. *Nutrients* **2**, 355–374 (2010).
3. Calder, P. C. Nutritional benefits of omega-3 fatty acids. *Food Enrichment with Omega-3 Fatty Acids* 3–26 (2013).
4. Michas, G., Micha, R. & Zampelas, A. Dietary fats and cardiovascular disease: Putting together the pieces of a complicated puzzle. *Atherosclerosis* **234**, 320–328 (2014).
5. McClements, D. J., Lu, J. & Grossmann, L. Proposed Methods for Testing and Comparing the Emulsifying Properties of Proteins from Animal, Plant, and Alternative Sources. *Colloids and Interfaces 2022, Vol. 6, Page 19* **6**, 19 (2022).
6. McClements, D. J. Food Emulsions: Principles, Practices, and Techniques. *CRC press* (2015).
7. Håkansson, A., Innings, F., Trägårdh, C. & Bergenståhl, B. A high-pressure homogenization emulsification model-Improved emulsifier transport and hydrodynamic coupling. *Chem Eng Sci* **91**, 44–53 (2013).
8. Raikar, N. B., Bhatia, S. R., Malone, M. F., McClements, D. J. & Henson, M. A. Predicting the effect of the homogenization pressure on emulsion drop-size distributions. *Ind Eng Chem Res* **50**, 6089–6100 (2011).
9. Håkansson, A. Emulsion Formation by Homogenization: Current Understanding and Future Perspectives. **10**, 239–258 (2019).
10. McClements, D. J. & Decker, E. A. Lipid oxidation in oil-in-water emulsions: Impact of molecular environment on chemical reactions in heterogeneous food systems. *J Food Sci* **65**, 1270–1282 (2000).
11. Schaich, K. M., Shahidi, F., Zhong, Y. & Michael Eskin, N. A. Biochemistry of foods. *London: Academic Press* 419–478 (2013).
12. Berton-Carabin, C. C., Ropers, M. H. & Genot, C. Lipid Oxidation in Oil-in-Water Emulsions: Involvement of the Interfacial Layer. *Compr Rev Food Sci Food Saf* **13**, 945–977 (2014).
13. Farmer, E. H., Bloomfield, G. F., Sundralingam, A. & Sutton, D. A. The Course and Mechanism of Autoöxidation Reactions in Olefinic and Polyolefinic Substances, Including Rubber. *Rubber Chemistry and Technology* **15**, 756–764 (1942).
14. Ghnimi, S., Budilarto, E. & Kamal-Eldin, A. The New Paradigm for Lipid Oxidation and Insights to Microencapsulation of Omega-3 Fatty Acids. *Compr Rev Food Sci Food Saf* **16**, 1206–1218 (2017).
15. Gardner, H. W. Oxygen radical chemistry of polyunsaturated fatty acids. *Free Radic Biol Med* **7**, 65–86 (1989).
16. Schroën, K. & Berton-Carabin, C. C. A unifying approach to lipid oxidation in emulsions: Modelling and experimental validation. *Food Research International* **160**, (2022).
17. Villeneuve, P. *et al.* Lipid oxidation in emulsions and bulk oils: a review of the importance of micelles. *Critical Reviews in Food Science and Nutrition* (2021).
18. Martínez-Yusta, A. & Guillén, M. D. Deep-frying food in extra virgin olive oil: A study by 1H nuclear magnetic resonance of the influence of food nature on the evolving composition of the frying medium. *Food Chem* **150**, 429–437 (2014).
19. Merkx, D. W. H., Hong, G. T. S., Ermacora, A. & van Duynhoven, J. P. M. Rapid Quantitative Profiling of Lipid Oxidation Products in a Food Emulsion by 1H NMR. *Anal Chem* **90**, 4863–4870 (2018).
20. Merkx, D. W. H. *et al.* Evaluation of PBN spin-trapped radicals as early markers of lipid oxidation in mayonnaise. *Food Chem* **334**, (2021).
21. Cui, L., Lahti, P. M. & Decker, E. A. Evaluating Electron Paramagnetic Resonance (EPR) to Measure Lipid Oxidation Lag Phase for Shelf-Life Determination of Oils. *JAOCS, Journal of the American Oil Chemists' Society* **94**, 89–97 (2017).
22. Shantha, N. C. & Decker, E. A. Rapid, Sensitive, Iron-Based Spectrophotometric Methods for Determination of Peroxide Values of Food Lipids. *JAOAC Int* **77**, 421–424 (1994).
23. Hellwig, M. The Chemistry of Protein Oxidation in Food. *Angewandte Chemie - International Edition* **58**, 16742–16763 (2019).
24. Winterbourn, C. C. Toxicity of iron and hydrogen peroxide: the Fenton reaction. *Toxicol Lett* **82–83**, 969–974 (1995).
25. ten Klooster, S. *et al.* Lipid Oxidation in Food Emulsions: Analytical Challenges and Recent Developments. *Lipid Oxidation in Food and Biological Systems* 3–29 (2022).
26. Gumus, C. E., Decker, E. A. & McClements, D. J. Impact of legume protein type and location on lipid oxidation in fish oil-in-water emulsions: Lentil, pea, and faba bean proteins. *Food Research International* **100**, 175–185 (2017).
27. Berton, C., Ropers, M. H., Guibert, D., Solé, V. & Genot, C. Modifications of interfacial proteins in oil-in-water emulsions prior to and during lipid oxidation. *J Agric Food Chem* **60**, 8659–8671 (2012).

28. Berton, C., Genot, C. & Ropers, M. H. Quantification of unadsorbed protein and surfactant emulsifiers in oil-in-water emulsions. *J Colloid Interface Sci* **354**, 739–748 (2011).

29. Laguerre, M., Tenon, M., Bily, A. & Birtić, S. Toward a Spatiotemporal Model of Oxidation in Lipid Dispersions: A Hypothesis-Driven Review. *European Journal of Lipid Science and Technology* **122**, (2020).

30. Gumus, C. E., Decker, E. A. & McClements, D. J. Impact of legume protein type and location on lipid oxidation in fish oil-in-water emulsions: Lentil, pea, and faba bean proteins. *Food Research International* **100**, 175–185 (2017).

31. Costa, M. *et al.* Interfacial kinetics in olive oil-in-water nanoemulsions: Relationships between rates of initiation of lipid peroxidation, induction times and effective interfacial antioxidant concentrations. *J Colloid Interface Sci* **604**, 248–259 (2021).

32. Feng, J., Berton-Carabin, C. C., Fogliano, V. & Schroën, K. Maillard reaction products as functional components in oil-in-water emulsions: A review highlighting interfacial and antioxidant properties. *Trends in Food Science and Technology* vol. 121 129–141 (2022).

33. Liu, J. *et al.* Effects of Chelating Agents and Salts on Interfacial Properties and Lipid Oxidation in Oil-in-Water Emulsions. *J Agric Food Chem* **67**, 13718–13727 (2019).

34. Chen, J., Li, X., Kong, B., Chen, Q. & Liu, Q. Comparative study of protein-lipid co-oxidation in whey protein isolate-stabilised oil-in-water emulsions prepared by different homogenisation methods. *Colloids Surf A Physicochem Eng Asp* **633**, (2022).

35. McClements, D. J. & Decker, E. Interfacial Antioxidants: A Review of Natural and Synthetic Emulsifiers and Coemulsifiers That Can Inhibit Lipid Oxidation. *Journal of Agricultural and Food Chemistry* vol. 66 20–25 (2018).

36. Aslam, A. & Schroën, K. Lipid oxidation in food emulsions; a review dedicated to the role of the interfacial area. *Curr Opin Food Sci* 101009 (2023).

37. Schaich, K. Schaich, K.M. 2008. Co-oxidations of oxidizing lipids: Reactions with proteins, in Lipid Oxidation Pathways, Chapter 8, Vol 2, ed. Kamal-Eldin, A. and Min, D., AO.... **2**, (2015).

38. Laguerre, M., Bily, A., Roller, M. & Birtić, S. Mass Transport Phenomena in Lipid Oxidation and Antioxidation. *Annu Rev Food Sci Technol* **8**, 391–411 (2017).

39. Pryor, W. A. Oxy-radicals and related species: their formation, lifetimes, and reactions. *Annu Rev Physiol* **48**, 657–667 (1986).

40. Termini, J. Peroxyl and alkoxyl radical mediated DNA damage. in *Critical reviews of oxidative stress and aging. Advances in basic science, diagnostics and intervention* vol. 1 39–53 (2003).

41. Anton, M. Egg yolk: structures, functionalities and processes. *J Sci Food Agric* **93**, 2871–2880 (2013).

42. Takeuchi, M. *et al.* Characterization of hen phosvitin in aqueous salt solutions: Size, structure, and aggregation. *Food Hydrocoll* **129**, 107545 (2022).

43. Merkx, D. W. H., Delić, F., Wieringa, P. A., Hennebelle, M. & van Duynhoven, J. P. M. 31P NMR assessment of the phosvitin-iron complex in mayonnaise. *Magnetic Resonance in Chemistry* **57**, 540–547 (2019).

44. Sinnhuber, R. O. & Yu, T. C. *The 2-Thiobarbituric Acid Reaction, An Objective Measure of the Oxidative Deterioration Occurring in Fats and Oils*.

45. Srinivasan, S., Xiong, Y. L. & Decker, E. A. *Inhibition of Protein and Lipid Oxidation in Beef Heart Surimi-like Material by Antioxidants and Combinations of pH, NaCl, and Buffer Type in the Washing Media †*. https://pubs.acs.org/sharingguidelines (1996).

46. Merkx, D. W. H. *et al.* Evaluation of PBN spin-trapped radicals as early markers of lipid oxidation in mayonnaise. *Food Chem* **334**, 127578 (2021).

47. Innawong, B., Mallikarjunan, P. & Marcy, J. E. The determination of frying oil quality using a chemosensory system. *LWT - Food Science and Technology* **37**, 35–41 (2004).

48. Barriuso, B., Astiasarán, I. & Ansorena, D. A review of analytical methods measuring lipid oxidation status in foods: a challenging task. *European Food Research and Technology 2012 236:1* **236**, 1–15 (2012).

49. Janzen, E. G., Jandrisits, L. T., Shetty, R. V., Larry Haire, D. & Hilborn, J. W. Synthesis and purification of 5,5-dimethyl-1-pyrroline-N-oxide for biological applications. *Chem Biol Interact* **70**, 167–172 (1989).

50. Levine, R. L. *et al.* 464 *ASSAY AND REPAIR OF BIOLOGICAL DAMAGE [49] [49] Determination of Carbonyl Content in Oxidatively Modified Proteins*. (1990).

51. Ehrenshaft, M., Deterding, L. J. & Mason, R. P. Tripping up Trp: Modification of protein tryptophan residues by reactive oxygen species, modes of detection, and biological consequences. *Free Radical Biology and Medicine* vol. 89 220–228 (2015).

52. Liu, G. & Xiong, Y. L. Electrophoretic pattern, thermal denaturation, and in vitro digestibility of oxidized myosin. *J Agric Food Chem* **48**, 624–630 (2000).

53. Raudsepp, P., Brüggemann, D. A., Knudsen, J. C. & Andersen, M. L. Localized lipid autoxidation initiated by two-photon irradiation within single oil droplets in oil-in-water emulsions. *Food Chem* **199**, 760–767 (2016).

54. Raudsepp, P. & Brüggemann, D. A. Spatiotemporal studies of lipid oxidation by optical microscopy. *Omega-3 Delivery Systems: Production, Physical Characterization and Oxidative Stability* 215–238 (2021).

55. Raudsepp, P., Brüggemann, D. A. & Andersen, M. L. Detection of radicals in single droplets of oil-in-water emulsions with the lipophilic fluorescent probe BODIPY665/676 and confocal laser scanning microscopy. *Free Radic Biol Med* **70**, 233–240 (2014).

56. Raudsepp, P., Brüggemann, D. A. & Andersen, M. L. Evidence for transfer of radicals between oil-in-water emulsion droplets as detected by the probe (E, E)-3, 5-bis (4-phenyl-1, 3-butadienyl)-4, 4-difluoro-4-bora-3a, 4a-diaza-s-indacene, BODIPY665/676. *J Agric Food Chem* **62**, 12428–12435 (2014).

57. Banerjee, C., Westberg, M., Breitenbach, T., Bregnhøj, M. & Ogilby, P. R. Monitoring Interfacial Lipid Oxidation in Oil-in-Water Emulsions Using Spatially Resolved Optical Techniques. *Anal Chem* **89**, 6239–6247 (2017).

58. Rietjens, I. M. C. M. *et al.* The pro-oxidant chemistry of the natural antioxidants vitamin C, vitamin E, carotenoids and flavonoids. *Environ Toxicol Pharmacol* **11**, 321–333 (2002).

2

Principles and application of fluorescence microscopy to food oxidation studies

2.1 General introduction

Lipid oxidation is one of the main causes of quality deterioration in food emulsions, leading to the generation of off-flavors and a concomitant reduction in shelf-life. Over the past decades, it has been recognized that droplet interfacial composition and colloidal transport mechanisms play important roles[1] in emulsions, besides the radical chain reaction pathway. However, the mainstream methods currently used to assess lipid oxidation in food products, such as peroxide value, para-anisidine, TBARs, and assessment of volatiles in the headspace, focus on a single type of oxidation product and fail to grasp the multiscale complexity of lipid oxidation reactions[2]. This contrasts the methodological advances of imaging techniques in the biomedical field[3,4] that enabled breakthroughs in understanding the role of lipids in mediating biological processes[5,6]. The multi-scale complexity of food emulsions has raised the need to obtain more insights into the spatiotemporal resolution of the chemical reactions [1] and the role of interfacial composition. Although the role of emulsifiers like proteins in mediating lipid oxidation at droplet interfaces has been recognized[7], it has remained challenging to directly localize these at colloidal interfaces and establish mechanistic links with oxidation reactions. To address the multiscale challenges of localizing proteins and oxidation events at interfaces, different types of electron- and fluorescence microscopy can be implemented (**Figure 2.1**). Transmission electron microscopy (TEM) and scanning electron microscopy (SEM) can cover the nm to µm range, whereas fluorescence microscopy, specifically confocal laser scanning microscopy (CLSM), provides access to the µm to mm range allowing the direct observation of lipid oxidation as well as studying structural changes upon oxidation. To connect the resolution gap between electron and standard light microscopy, super-resolution microscopy techniques can be applied[8,9].
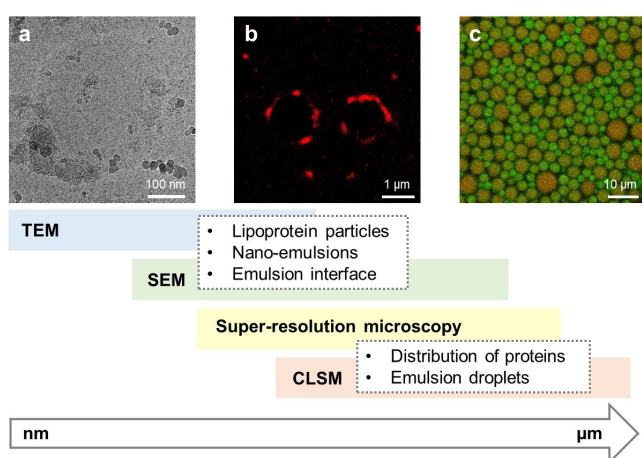

Figure 2.1. Summary of microscopy techniques and key features found in food emulsions. (**a**) Cryo-TEM image of oxidized oil droplets with lipoprotein particle aggregates at the interface in egg yolk stabilized emulsions. (**b**) Super-resolution image of oxidized proteins at droplet interfaces stabilized with egg yolk. Fluorescently labeled spin traps were used to localize the oxidized proteins. (**c**) CLSM image of lipid droplets in mayonnaise in the presence of the lipophilic and oxidation sensitive fluorophore BODIPY 665/676. Green and orange color indicates oxidized and non-oxidized lipid droplets, respectively[10].

2.2   Introduction to optical microscopy

Microscopy has greatly impacted the study of human life, playing a crucial role in various fields, such as medicine and the semiconductor industry. While the human eye has a limited resolution of 200 µm (0.2 mm)[11], light microscopes can magnify images up to 1000 times, resulting in a resolution of 0.2 µm. This section first introduces the principles of different optical microscopy techniques, from standard to super-resolution microscopy. Then, we will briefly introduce methods for localizing protein oxidation. Lastly, recent examples will be presented to demonstrate the potential use of these techniques for localizing oxidation in food emulsions.

2.2.1   Principles of optical microscopy

A setup for basic optical microscopy, such as bright field light microscopy, is depicted in **Figure 2.2a**. The sample is illuminated with a light source, and an objective collects the transmitted light. Then, this light is projected on a camera via a lens. Bright field microscopy is useful for resolving the structure of objects that are a few µm in size and is often complemented with fluorescence microscopy, which provides specificity and improved contrast over transmission bright field microscopy. Compared to bright field microscopy, fluorescence microscopy techniques such as wide-field or epifluorescence microscopy require additional components and specific labels (**Figure 2.2b**). In wide-field or epifluorescence microscopy, the light from colored LEDs or lasers is first collimated with a lens and then focused into the objective's back focal plane leading to the maximum illumination area on the sample. As fluorescence microscopy requires labeling samples with fluorophores, it is important to understand the basic principles of fluorescence.

A fluorophore is a molecule that can be specifically attached to target proteins and lipids or can probe its environmental surrounding. The principle of fluorescence can be explained using a Jablonski diagram (**Figure 2.2c**). A fluorophore is excited to a higher vibrational energy state (S_1^{vib}) by absorbing a photon with an energy of a specific wavelength region, often called the excitation range. The relaxation of the fluorophore occurs almost instantly from S_1^{vib} without radiation to the lowest vibrational energy level of S_1. The lowest vibrational energy of this state in S_1 has a much longer lifetime (~ ns) compared to a vibrational state (S_1^{vib}) (~ ps). In the next transition stage, the molecule returns to the ground state (S_0) via either non-radiative decay or spontaneous emission. In other words, energy is released as heat (non-radiative decay) or a photon (spontaneous emission, often called emission). Emitted photons have a lower energy level than excitation photons, as energy is lost during the emission process via solvent relaxation[12]. The solvent relaxation is due to the reorientation of solvent molecules surrounding the excited fluorophores. The solvent-dependent spectral shift that occurs due to solvent relaxation leads to a red shift of the emission spectrum profile compared to the excitation. As a

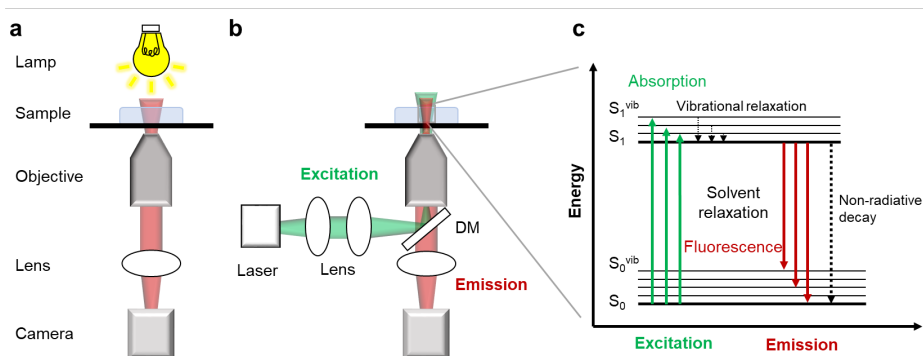result, the emission spectrum typically resembles a shifted mirrored version of the absorption profile.

Figure 2.2. Optical setups for microscopy. (**a**) Schematic of conventional bright-field microscopy. A lamp illuminates the samples, and the transmitted light is collected via an objective. Then, the light is focused on a detector (camera) by a lens. (**b**) Schematic of fluorescence microscopy, such as wide-field or epi-fluorescence microscopy. (Excitation path, green) The laser is collimated with a lens and is focused on the back focal plane of the objective by another lens via a dichroic mirror (DM). (Emission path, red) The fluorescence signal is collected with the same objective, then passes the dichroic mirror and is focused on the detector via a lens. (**c**) Jablonski diagram of energy state transitions for fluorescence and non-radiative decay. The molecule in the ground state (S_0) is excited by absorbing a photon to a higher electronic and vibrational energy state (S_1^{vib}). After the absorption, relaxation to the lowest vibrational energy level of S_1 occurs in the ps time range. The molecule then decays to the ground state (S_0) via either non-radiative decay (in the form of heat) or spontaneous emission (fluorescence).

2.2.2   Resolution in fluorescence microscopy

The resolution in a microscope is defined as the shortest distance between two points that can be distinguished by a detector as separate objects. Several factors decide the resolution of the microscope, and here we introduce two factors, objective lens and light source. An objective can contribute to the resolution in the optics system via the numerical aperture (NA). The NA of the objective lens determines the range of angles from which the objective lens can accept the light from the sample plane (**Figure 2.3a**) and is defined as

$$NA = n \cdot \sin\theta, \tag{2.1}$$

where n is the refractive index of the medium between the objective lens and the sample, and θ is the half-angle of the light cone accessible for collection by the objective. In theory, the maximum angle of the light cone collected by the objective lens is 180° ($\theta = 90°$), and thus the theoretical NA can reach unity in a medium of air ($n_{air} = 1$). However, a collection angle of 90° cannot be achieved as light is refracted between two media, such as glass and air. Refraction is a direction change of light waves and can be described in a formula known as 'Snell's Law' (**Equation 2.2**).

$$n_1 \sin\theta_1 = n_2 \sin\theta_2 \tag{2.2}$$

29

Snell's Law explains that the ratio of the angles of the incident (θ_1) and refracted light (θ_2) is equivalent to the reciprocal of the ratio of the refractive indices (n_1 and n_2) which the light passes through. When light propagates from one medium to another, its velocity changes; for example, light slows down when passing from air to water. The frequency (f) of light does not change, but the wavelength (λ) is determined by the refractive index of the medium (n). In optical microscopy, the light from a specimen refracts from the sample, often in water, to glass and air (**Figure 2.3b**). The refractive index is the limiting factor for achieving high NA in an objective. Consequently, the NA can be maximized by matching the refractive indices between the sample, the mounting medium and the objective with its glass surface (**Figure 2.3b**).

The NA of the objective determines the characteristics of the point spread function (PSF). In the wave description of light, the light emitted by a single fluorophore seen through an optical microscope will undergo diffraction as it travels through the microscope optics. Once the light reaches the detector, it will be observed as a diffraction pattern, the PSF (**Figure 2.3c**). The PSF can be considered as the light intensity distribution in the image acquired by the microscope from a point source (**Figure 2.3c**). In the image plane of a standard optical system, the PSF is shaped as an Airy diffraction pattern with the first minimum at $r = w/2$, where w is the width of the Zeroth order Airy pattern. The PSF forms a series of concentric disks (the Airy disk pattern) with the highest intensity at its center, the Airy disk of order 0 (**Figure 2.3c**). The shape of the PSF depends on the wavelength of the traveling light (λ) and the NA of the microscope objective.

Two Airy discs separated by the distance $r \geq w/2$ can be resolved as separate entities, but not at smaller r (**Figure 2.3d**). This limit is often called the Rayleigh criterion or the diffraction limit and defines the lateral resolution of the objective as

$$r_{\text{lateral}} = \frac{0.61\,\lambda}{NA}. \tag{2.3}$$

According to the Rayleigh criterion, the resolution limit at which two light-emitting objects cannot be resolved is the distance at which the peak of the Airy pattern of one emitter overlaps with the first minimum of the Airy disk and the zero-order of the other Airy pattern. At higher NA values, the width of the zero-order disk on the PSF equals approximately half of the wavelength of the light emitted by the fluorophore, and thus the resolution limit of an optical microscope is commonly $200 - 350$ nm.

Another factor determining the optical resolution is the wavelength of light (λ), as seen in **Equation 2.3**. Shorter wavelengths provide better resolution (**Figure 2.3e**). Simply, the resolution of electron microscopy is higher than in fluorescence microscopy due to the smaller associated wavelength of electrons. A combination of light and electron microscopy will be discussed in **Chapter 6**.
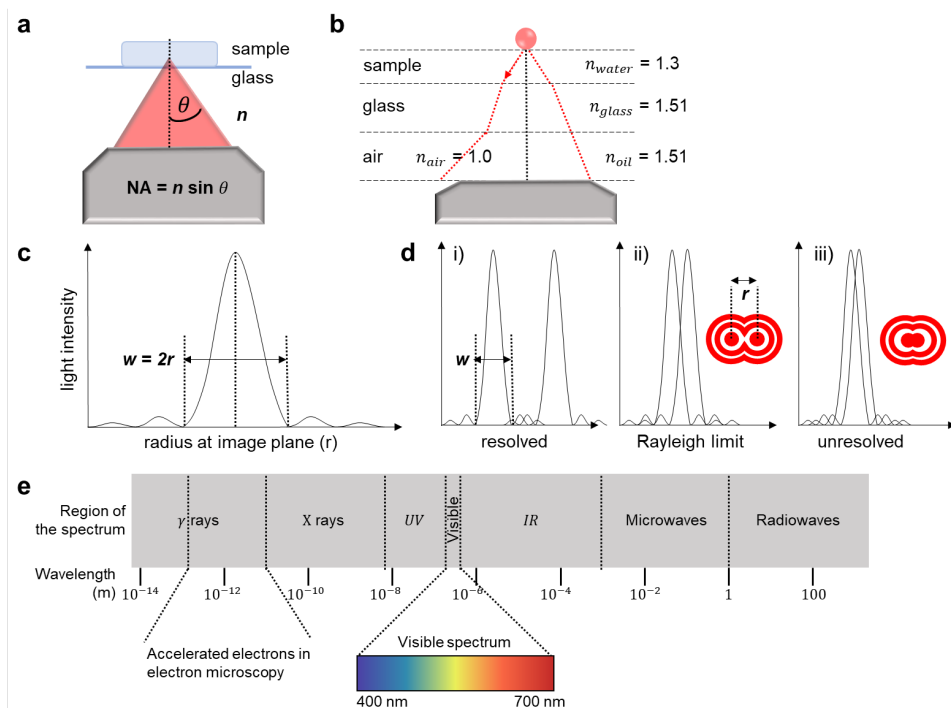
Figure 2.3. Schematic description of resolution in microscopes. (**a**) Definition of numerical aperture (NA). The NA defines the accessible angle (θ) of collecting light from the sample, which can be maximized by matching the refractive index (n) between the material light passes through. (**b**) Refracted light passing through different materials. The NA is maximized by matching the refractive index between mediums. (**c**) Airy patterns in the image plane. "w" indicates the width of the zeroth order Airy pattern with the first minimum at $r = w/2$ (**d**) Two Airy patterns of resolved (i), Rayleigh limit (ii), and unresolved (iii) images. "r" shows the separation distance between the centers of Airy discs. (**e**) The region of the spectrum and the following wavelength is described. Electron microscopy has a higher resolution than fluorescence microscopy due to the shorter wavelength of accelerated electrons.

2.2.3 Confocal microscopy

Confocal laser scanning microscopy (CLSM) is used extensively in the life, food, and material sciences. CLSM is an imaging technique for improving optical resolution based on optical sectioning (**Figure 2.4a**). CLSM introduces a point illumination using a scanning unit (often mirrors) in the excitation path (**Figure 2.4b**). Additionally, the aperture (pinhole) in an optically conjugate plane (image plane) in front of the camera allows for the effective suppression of out-of-focus signal. Using an aperture, light is only collected from a small volume around the focal plane. Re-scan confocal microscopy (RCM)[13] is based on standard confocal microscopy but uses an additional re-scan mirror in the emission path (**Figure 2.4c**). RCM does not require any computational reconstruction process of the image, which is often necessary for super-resolution techniques. The main key to the super-resolution properties of RCM is the de-coupling of the

scanning magnification of the object (M_{obj}) and the magnification of the scanning spot (M_{spot}). RCM improves lateral resolution with optical sectioning using this de-coupling of magnification. The sweep factor M can be defined as; $M = M_{obj} / M_{spot}$. The minimum spot width W, Full Width at Half Maximum (FWHM), can be achieved[13,14] when the decoupling factor is roughly $M = 2$.

$$W_{RCM} = \frac{\sqrt{(M-1)^2 + 1}}{M} \times W_{WF} \tag{2.4}$$
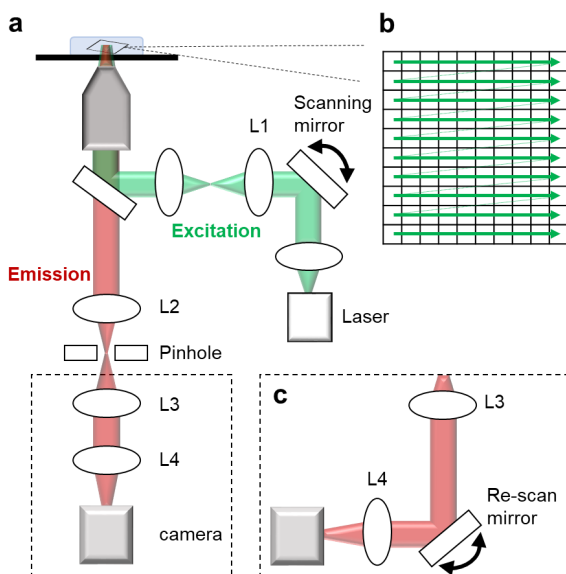

Figure 2.4. Schematic of confocal laser scanning microscopy (CLSM) and re-scan confocal microscopy (RCM). (**a**) Optical setup of CLSM. The laser is collimated with a lens and passes through a scanning mirror, one of the main components of CLSM. The laser is focused in the first image plane with a lens (L_1) and expanded via another lens. The beam illuminates the samples via the objective, and the emission from fluorophores will be collected with the same objective. The emitted light is focused with a lens (L_2), and the pinhole (aperture) blocks all light that originates from outside the focus. The light passing through the pinhole is again collimated with a lens (L_3) and focused on a point detector via a lens (L_4). (**b**) Schematic of laser spots in the field of view from the scanning mirror in CLSM. (**c**) Optical setup of the RCM. The excitation path is the same as CLSM, but an additional re-scan mirror is inserted in the emission path.

2.2.4 Stochastic optical reconstruction microscopy

As we explained in the previous section, the spatial resolution of standard optical fluorescence microscopy is limited to ~200 nm, resulting in blurred images of smaller structures. To overcome the resolution limit, different microscopy methods have emerged over the past two decades. The most well-known super-resolution microscopy methods are stimulated emission depletion (STED)[15], structured illumination microscopy (SIM)[16,17], and single-molecule localization microscopy (SMLM)[18–21]. Single-molecule localization microscopy (SMLM) usually implements a conventional wide-field microscopy system (**Figure 2.2b**) and achieves super-resolution by reconstructing images after localizing individual molecules[22]. The basic principle of SMLM is to find conditions that avoid the overlap of the point spread function (PSF). For each PSF, the spatial coordinate can be obtained with high precision by fitting, for example, a

2D Gaussian function over the PSF. To minimize the overlapping of PSFs, the emission of fluorescent molecules is separated in time.

As one type of single molecule localization microscopy (SMLM), stochastic optical reconstruction microscopy (STORM) imaging achieves temporal separation by exploiting the phenomenon of photoswitching[18,19]. Photoswitching is a stochastic event in which fluorescent molecules switch between an active 'ON' state, emitting fluorescence after excitation, and an 'OFF' state, where they do not fluoresce (**Figure 2.5a**). The switching probabilities can be optimized using laser illumination or changing the chemical environment[23]. Under proper conditions, only a subset of molecules in the sample will be in the 'ON' state and appear as spatially resolved, non-overlapping PSFs. The basic steps of STORM imaging consist of measurements and computational processing. In the measurement steps, the original structure of the target subject is labeled with fluorophores (**Figure 2.5b-i**), and these fluorophores show 'blinking' events by ON and OFF switching (**Figure 2.5b-ii**). For instance, the fluorophore shows an ON state in the first frame ($t = 1$) but an OFF state in the second frame ($t = 2$). Many image frames in the same field of view are acquired (**Figure 2.5b-iii**), after which images are processed computationally. In the computational processing steps, all ON molecules are detected, and their coordinates are determined (**Figure 2.5c**) with sub-pixel localization precision[24]. Ultimately, all localizations are combined into a single image (**Figure 2.5d-i**). The resolution and quality of the final image are determined by the accuracy and precision of localizations, which depend on the density of molecules, the percentage of localization events, and many other things, most importantly, the number of detected photons per localization. Photoswitching can occur either in the presence (STORM) or in the absence of an activator dye (direct STORM, dSTORM). (d)STORM can achieve nm-resolution[25] whereas in conventional wide-field microscopy, all fluorophores are illuminated simultaneously, resulting in diffraction-limited images (**Figure 2.5d-ii**).
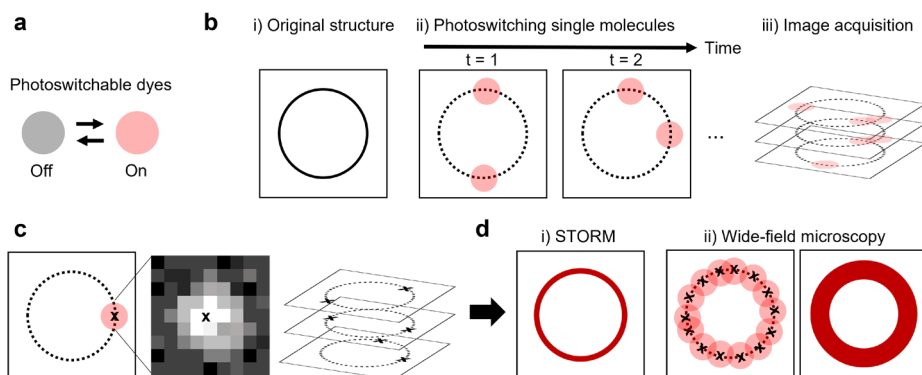
Figure 2.5. The principle of single-molecule localization microscopy (SMLM). (**a**) Schematic of photoswitchable dyes. ON and OFF states show a fluorescent and dark state, respectively. (**b**) Measurement process of stochastic optical reconstruction microscopy (STORM). The original structure (i) is labeled with fluorophores, and single molecules are photoswitching in each frame (ii). Thousands of frames in the same field of view are acquired (iii). (**c**) Computational processing of STORM images. The precise location is determined using the intensity distribution of the point spread function (PSF), and many different localizations are combined into a single image. (**d**) Schematic of the final image from STORM (i) and wide-field imaging (ii). All fluorophores are illuminated simultaneously in wide-field imaging resulting in the diffraction limits.

2.3   Determination of protein oxidation using autofluorescence

Intrinsic tryptophan fluorescence has been exploited to study protein oxidation in food emulsions[26,27]. Spectro-fluorometry has been successfully applied to determine the oxidation of bovine serum albumin (BSA) and dairy proteins using the decrease in the fluorescence of natural tryptophan and the increase in fluorescence from protein oxidation products[28–31]. Tryptophan emits at around 350 nm after excitation at 280 nm. Changes in the fluorescence intensity of tryptophan have been used to monitor physio-chemical changes in proteins, including those derived from oxidative stress[28]. The decrease in tryptophan fluorescence is due to the oxidative degradation of tryptophan and electron transfers[32]. On the other hand, carbonyl compounds produced from protein oxidation are included in cross-linking of damaged proteins via Schiff base formation. Schiff bases are formed by reactions between aldehydes and amino groups from proteins. These compounds form conjugated fluorophores[33], which can be detected by emission at around 450 nm when excited at around 350 nm. The measurement of their fluorescence has been implemented as a protein oxidation index[31].

An example of how autofluorescence can be used as a measure for studying protein oxidation in mayonnaise is shown in **Figure 2.6**. This figure presents the experiments performed with the water phase of mayonnaise, where egg yolk is the main emulsifier. Low-density lipoprotein (LDL) particles present in egg yolk have been reported to show autofluorescence in the ultraviolet region[10,28]. **Figure 2.6** shows the intensity changes observed in the fluorescence

spectrum of fresh and oxidized (1, 3, and 5 days) water phases separated from mayonnaise. The autofluorescence of these aqueous phases was measured using a fluorescence spectrometer with three different excitation wavelengths (300, 360, and 405 nm). Upon oxidation of the samples and excitation at 300 nm, we observed a decrease of fluorescence emission at around 340 nm. With excitation at 360 or 405 nm, an increase of fluorescence can be observed originating from the reaction between aldehyde-apolipoprotein adducts (**Figure 2.6**). The emission peak of non-oxidized tryptophan is typically found between 300 to 350 nm, depending on the polarity of the local environment. This signal is primarily attributed to oxidized LDL because phosvitin, which also exists in the continuous phase of mayonnaise, contains much less tryptophan[34,35]. We note that the observed red shift of the peak might represent conformational transitions, sub-unit association or denaturation of the proteins present in the sample. In these cases, the redshift could be caused by tryptophan moving from a hydrophobic surrounding to a hydrophilic environment, such as from the protein interior towards the aqueous media[36].
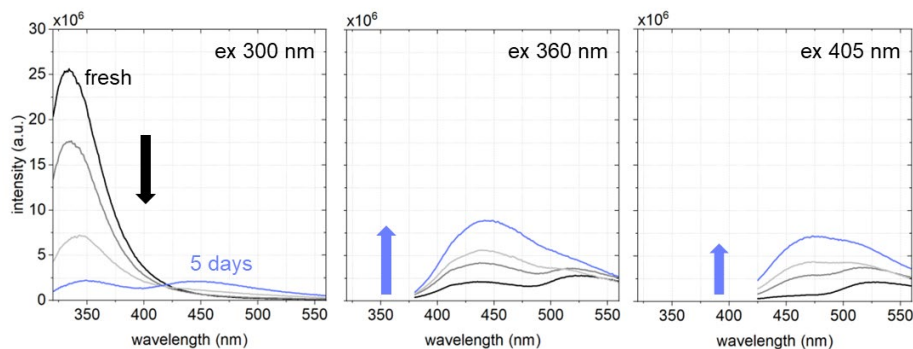

Figure 2.6. Changes in the fluorescence spectrum of the aqueous phase separated from mayonnaise in fresh (black) and after one (grey), three (light grey), and five (blue) days of oxidation of the sample incubated at 40 °C. The arrows indicate the changes in the peak intensity upon excitation 300 nm (left), 360 nm (middle) and 405 nm (right). The increase of emission after excitation at 360 and 405 nm upon oxidation indicates the Schiff base reaction between amino groups from tryptophan and aldehydes.

Examples of how autofluorescence can also be used to localize protein oxidation are shown in **Figure 2.7.** In the oxidized WPI-stabilized O/W emulsion, autofluorescence from oxidized proteins is heterogeneously distributed at the droplet interface (**Figure 2.7a**). Also, the infant formula prepared with WPI showed noticeable changes in autofluorescence after 77 days of oxidation. (**Figure 2.7b**). On the other hand, the fresh PPI-infant formula already had a high level of autofluorescence and did not show further increase upon oxidation (**Figure 2.7c**), which in this case limits the applicability of autofluorescence as an indicator of protein oxidation during shelf-life. These examples show the potential of autofluorescence for localizing protein oxidation in food emulsions. It should be noted that caution is required when comparing results between emulsions prepared with different proteins, as all proteins do not have the same initial

intensity levels. In **Chapter 3** and **4**, we will link local changes in protein autofluorescence with the formation of protein radicals and lipid oxidation in a systematic manner.
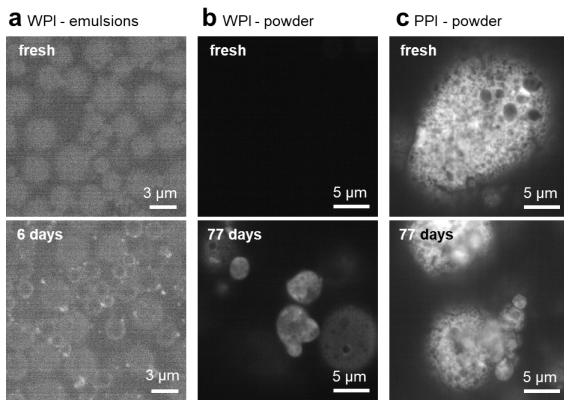

Figure 2.7. Autofluorescence in different food products. Autofluorescence in whey protein isolate (WPI)-stabilized oil-in-water emulsions (**a**), WPI-infant formula (**b**), and pea protein isolate (PPI)-infant formula (**c**). The images were acquired with excitation at 405 nm in re-scan confocal microscopy (RCM). WPI-stabilized O/W emulsions were prepared with colloid mills and oxidized at 25 ºC in the presence of 5 mM AAPH. The WPI- and PPI-infant formulas were oxidized at 40 ºC.

2.4   Current fluorescence microscopy studies of food oxidation

Fluorescence microscopy has been applied in many research areas allowing for multi-color detection and measurements under ambient conditions. Confocal laser scanning microscopy (CLSM) is a widely used variant reaching a lateral resolution of ~200 nm and featuring effective optical sectioning capabilities by removing the out-of-focus light with a pinhole placed in the first conjugated image plane. In food research, CLSM is an established technique that allows for studying the stability of emulsions and observing dynamic changes in food structures[37]. Furthermore, fluorescence microscopy enables the characterization of oxidation processes in food emulsions. Also, fluorophores offer additional readouts on polarity, pH, and sensitivity to oxygen and free radicals within the target sample. Fluorophores are either specifically attached to biomolecules, such as fluorescently labeled secondary antibodies targeting primary antibodies attached to proteins of interest, or the fluorophores are directly monitored while freely diffusing in the lipid or aqueous phase of food emulsions. Due to the presence of oxidizable proteins in foods, detecting autofluorescence also provides an additional read-out that can be used to co-localize lipids and proteins. In the following section, we will provide a short overview of fluorophores suitable to monitor the structural impact of lipid oxidation processes and localize oxidation events. The chemical structure of fluorophores is illustrated in **Table 2.1**.

2.4.1   Assessment of the microstructural impact of oxidation using non-covalently bound organic fluorophores

The fluorophore Nile red is frequently used for staining intracellular lipid droplets and neutral lipids[38,39]. Its fluorescence emission spectrum ranges from yellow to deep red depending on the

polarity of the solvent. Nile red is non-fluorescent in water but turns fluorescent when entering lipid-rich or hydrophobic environments. Therefore, Nile red is suitable for studying the microstructural stability of emulsions that contain lipids. Zafeiri et al. used Nile red with CLSM to study the potential of solid lipid particles as Pickering stabilizers in O/W emulsions[40]. The fluorophore Nile blue, structurally similar to Nile red, is also suitable for staining lipid structures. Nile blue was used to elucidate the oil volume fraction impact on the formation and properties of cold-set soy protein isolate (SPI)-stabilized emulsion gels[41]. BODIPY 493/503 (4,4-Difluoro-1,3,5,7,8-Pentamethyl-4-Bora-3a,4a-Diaza-s-Indacene) is a stain for neutral lipids and has maximum emission at 515 nm. Barden et al. studied the relationship between physical structure and oxidative stability in crackers using CLSM and BODIPY 493/503[42]. For evaluating the distribution of natural antioxidants in poultry meals and extruded kibbles, the BODIPY dye was applied in the work of Ye et al.[43]. Rhodamine B can be added to the water phase to detect proteins via non-specific staining of proteins. In several studies, Rhodamine B was combined with lipid-staining fluorophores (e.g., Nile red, Nile blue, BODIPY) to simultaneously study lipid and protein structures[40–43].

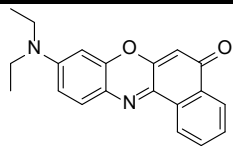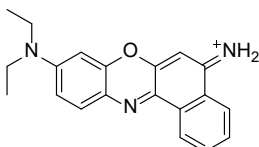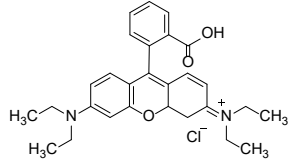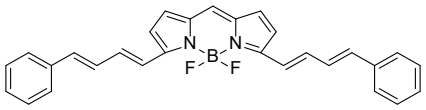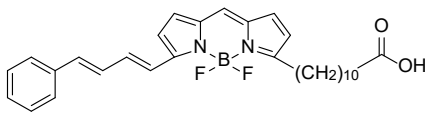### 2.4.2 Localization of lipid oxidation events using organic fluorophores

BODIPY 665/676 is a lipid peroxidation sensor that exhibits a spectral change in fluorescence after interaction with peroxyl radicals. In a non-oxidized environment, the fluorophore shows fluorescence emission in the red spectral region (650 - 720 nm) but shifts the emission to green (580 - 650 nm) after being oxidized. Raudsepp et al. used CLSM and BODIPY 665/676 to detect radicals at the single droplet level in O/W emulsions[44,45]. Due to the long excitation wavelength, BODIPY 665/676 minimizes the potential spectral overlap with the autofluorescence of oxidized proteins, making it ideal for detecting lipid oxidation in food systems comprising both lipids and proteins[44]. BODIPY 665/676 is resistant to photobleaching, does not diffuse into the aqueous phase or between lipid droplets and can be combined with additional fluorescent probes[44]. In **Chapter 3**, we will quantitatively map lipid and protein oxidation in mayonnaise by monitoring the green and red spectral regions of BODIPY 665/676 emission together with autofluorescence in the blue detection channel from oxidized proteins[10]. BODIPY 581/591 C-11 is another free radical sensor that changes fluorescence intensity upon oxidation. This fluorophore shifts its peak emission and excitation wavelength from 581/591 nm to 500/510 nm upon oxidation. BODIPY 581/591 C-11 is, however, less sensitive toward peroxyl radicals than BODIPY 665/676 due to its lower number of conjugated dienes[46,47]. Banerjee et al. showed lipid oxidation reactions at oil-water interfaces featuring polyunsaturated fatty acids from the cod liver cell with BODIPY 581/591 C-11 and high-resolution, structured-illumination microscopy (SIM)[48]. DPPP (diphenyl-1-Pyrenylphosphine) allows for direct fluorometric detection of hydroperoxides in lipids. In its unoxidized state, DPPP is non-fluorescent but turns fluorescent after oxidation by

peroxides with a peak fluorescence at 380 nm and excitation at 352 nm. Mosca et al. investigated the effect of the emulsifiers' layer structure in olive oil-in-water emulsions by comparing the changes in fluorescence intensity of DPPP upon oxidation[49]. **Table 2.1** provides an overview of the chemical structures of the fluorophores discussed, which can be used to monitor structural changes and localize oxidation events.

2.5   Conclusions

This chapter summarized the principles of fluorescence microscopy techniques, such as bright field, epi-fluorescence imaging, CLSM, RCM, and super-resolution microscopy. Furthermore, the recent development of microscopy techniques for characterizing protein oxidation at the interface and in the continuous phase of food emulsions has been reviewed. Microscopy is an emerging tool that can provide a more comprehensive overview of lipid and protein co-oxidation pathways and structural features. Specifically, microscopy provides spatial information showing, for instance, where oxidation is initiated. Moreover, readouts on both lipid and protein oxidation can be obtained simultaneously. In terms of sample preparation, time-consuming extraction steps are unnecessary, and samples can be measured in their native state. These advantages will be exploited in this thesis, together with other analytical approaches for spatiotemporally resolved characterization of events related to lipid oxidation in food emulsions.

Table 2.1. Summary of fluorophores for studying food microstructure and lipid oxidation. Overview of chemical structures of fluorophores with excitation/emission information. Emission peaks can vary in different solvents.

Target	Fluorophores (excitation/emission) nm	Chemical structure
Structure — Lipid	Nile red (λ_{ex} 532/ λ_{em} 585)	
	Nile blue (λ_{ex} 633/ λ_{em} 660)	
	BODIPY 493/503 (λ_{ex} 488/ λ_{em} 515)	
Structure — Protein	Rhodamine B (λ_{ex} 553/ λ_{em} 627)	
Oxidation mapping	BODIPY 665/676 (λ_{ex} 580 & 675/ λ_{em} 605/635 & 685)	
	BODIPY 581/591 C-11 (λ_{ex} 488 & 561/ λ_{em} 500-545 & 570-640)	
	DPPP (λ_{ex} 352/ λ_{em} 380)	

2

39
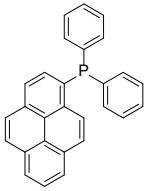
References

1. Laguerre, M., Tenon, M., Bily, A. & Birtić, S. Toward a Spatiotemporal Model of Oxidation in Lipid Dispersions: A Hypothesis-Driven Review. *European Journal of Lipid Science and Technology* **122**, (2020).
2. Frankel, E. N. & Meyer, A. S. Review The problems of using one-dimensional methods to evaluate multifunctional food and biological antioxidants. *Journal of the Science of Food and Agriculture* **80** (2000)
3. Hell, S. W. *et al.* The 2015 super-resolution microscopy roadmap. *J Phys D Appl Phys* **48**, 443001 (2015).
4. Schermelleh, L. *et al.* Super-resolution microscopy demystified. *Nat Cell Biol* **21**, 1 (2019)
5. Moon, S. *et al.* Spectrally Resolved, Functional Super-Resolution Microscopy Reveals Nanoscale Compositional Heterogeneity in Live-Cell Membranes. *J Am Chem Soc* **139**, 10944–10947 (2017).
6. Gemmink, A. *et al.* Super-resolution microscopy localizes perilipin 5 at lipid droplet-mitochondria interaction sites and at lipid droplets juxtaposing to perilipin 2. *Biochimica et Biophysica Acta (BBA) - Molecular and Cell Biology of Lipids* **1863**, 1423–1432 (2018).
7. Berton-Carabin, C. C., Ropers, M. H. & Genot, C. Lipid Oxidation in Oil-in-Water Emulsions: Involvement of the Interfacial Layer. *Compr Rev Food Sci Food Saf* **13**, 945–977 (2014).
8. Hohlbein, J. Single-molecule localization microscopy as an emerging tool to probe multiscale food structures. *Food Structure* **30**, 100236 (2021).
9. Jabermoradi, A., Yang, S., Gobes, M. I., Van Duynhoven, J. P. M. & Hohlbein, J. Enabling single-molecule localization microscopy in turbid food emulsions. *Philosophical Transactions of the Royal Society A* **380**, (2022).
10. Yang, S., Verhoeff, A. A., Merkx, D. W. H., van Duynhoven, J. P. M. & Hohlbein, J. Quantitative spatiotemporal mapping of lipid and protein oxidation in mayonnaise. *Antioxidants* **9**, 1–13 (2020).
11. Ul-Hamid, A. Introduction. *A Beginners' Guide to Scanning Electron Microscopy* 1–14 (2018).
12. Lakowicz, J. R. Principles of fluorescence spectroscopy. *Principles of Fluorescence Spectroscopy* 1–954 (2006).
13. De Luca, G. M. *et al.* Re-scan confocal microscopy: scanning twice for better resolution. *Biomedical Optics Express, Vol. 4, Issue 11, pp. 2644-2656* **4**, 2644–2656 (2013).
14. Roth, S., Sheppard, C. J. R., Wicker, K. & Heintzmann, R. Optical photon reassignment microscopy (OPRA). *Opt Nanoscopy* **2**, 1–6 (2013).
15. Donnert, G. *et al.* Macromolecular-scale resolution in biological fluorescence microscopy. *Proc Natl Acad Sci U S A* **103**, 11440–11445 (2006).
16. Heintzmann, R., Jovin, T. M. & Cremer, C. Saturated patterned excitation microscopy—a concept for optical resolution improvement. *JOSA A, Vol. 19, Issue 8, pp. 1599-1609* **19**, 1599–1609 (2002).
17. Gustafsson, M. G. L. Surpassing the lateral resolution limit by a factor of two using structured illumination microscopy. *J Microsc* **198**, 82–87 (2000).
18. Rust, M. J., Bates, M. & Zhuang, X. Sub-diffraction-limit imaging by stochastic optical reconstruction microscopy (STORM). (2006).
19. Heilemann, M. *et al.* Subdiffraction-Resolution Fluorescence Imaging with Conventional Fluorescent Probes. *Angew. Chem. Int. Ed* **47**, 33 (2008).
20. Hess, S. T., Girirajan, T. P. K. & Mason, M. D. Ultra-high resolution imaging by fluorescence photoactivation localization microscopy. *Biophys J* **91**, 4258–4272 (2006).
21. Betzig, E. *et al.* Imaging intracellular fluorescent proteins at nanometer resolution. *Science (1979)* **313**, 1642–1645 (2006).
22. Lelek, M. *et al.* Single-molecule localization microscopy. *Nature Reviews Methods Primers* **1**, (2021).
23. Li, Y. *et al.* Optimal 3D single-molecule localization in real time using experimental point spread functions. *Nat Methods* **15**, 367 (2018).
24. A Martens, K. J., Bader, A. N. & Baas, S. Phasor based single-molecule localization microscopy in 3D (pSMLM-3D): An algorithm for MHz localization rates using standard CPUs. *J. Chem. Phys* **148**, 123311 (2018).
25. Endesfelder, U. & Heilemann, M. Direct stochastic optical reconstruction microscopy (Dstorm). *Methods in Molecular Biology* **1251**, 263–276 (2014).
26. Berton, C. *et al.* Modifications of Interfacial Proteins in Oil-in-Water Emulsions Prior to and During Lipid Oxidation. (2012).
27. Estévez, M., Kylli, P., Puolanne, E., Kivikari, R. & Heinonen, M. Fluorescence spectroscopy as a novel approach for the assessment of myofibrillar protein oxidation in oil-in-water emulsions. *Meat Sci* **80**, 1290–1296 (2008).
28. Gießauf, A., Steiner, E. & Esterbauer, H. Early destruction of tryptophan residues of apolipoprotein B is a vitamin E-independent process during copper-mediated oxidation of LDL. *Biochimica et Biophysica Acta (BBA)/Lipids and Lipid Metabolism* **1256**, 221–232 (1995).

29. Viljanen, K., Kylli, P., Kivikari, R. & Heinonen, M. Inhibition of Protein and Lipid Oxidation in Liposomes by Berry Phenolics. *J Agric Food Chem* **52**, 7419–7424 (2004).

30. Viljanen, K., Kivikari, R. & Heinonen, M. Protein−Lipid Interactions during Liposome Oxidation with Added Anthocyanin and Other Phenolic Compounds. *J Agric Food Chem* **52**, 1104–1111 (2004).

31. Heinonen, M. *et al.* Effect of Protein on the Antioxidant Activity of Phenolic Compounds in a Lecithin−Liposome Oxidation System. *J Agric Food Chem* **46**, 917–922 (1998).

32. Ghisaidoobe, A. B. T. & Chung, S. J. Intrinsic Tryptophan Fluorescence in the Detection and Analysis of Proteins: A Focus on Förster Resonance Energy Transfer Techniques. *Int. J. Mol. Sci* **15**, 22518–22538 (2014).

33. Davies, M. J., Fu, S. & Dean, R. T. Protein hydroperoxides can give rise to reactive free radicals. *Biochemical Journal* **305**, 643–649 (1995).

34. Byrne, B. M. *et al.* Amino Acid Sequence of Phosvitin Derived from the Nucleotide Sequence of Part of the Chicken Vitellogenin Gene. *Biochemistry* **23**, 4275–4279 (1984).

35. Olofsson, S. O. *et al.* Apolipoprotein B: structure, biosynthesis and role in the lipoprotein assembly process. *Atherosclerosis* **68**, 1–17 (1987).

36. Miriani, M., Keerati-u-rai, M., Corredig, M., Iametti, S. & Bonomi, F. Denaturation of soy proteins in solution and at the oil-water interface: A fluorescence study. *Food Hydrocoll* **25**, 620–626 (2011).

37. Blonk, J. C. G. & van Aalst, H. Confocal scanning light microscopy in food research. *Food Research International* **26**, 297–311 (1993).

38. Greenspan, P., Mayer, E. P. & Fowler, S. D. Nile red: a selective fluorescent stain for intracellular lipid droplets. *J Cell Biol* **100**, 965–973 (1985).

39. Rumin, J. *et al.* The use of fluorescent Nile red and BODIPY for lipid measurement in microalgae. *Biotechnol Biofuels* **8**, 1–16 (2015).

40. Zafeiri, I., Smith, P., Norton, I. T. & Spyropoulos, F. Fabrication, characterisation and stability of oil-in-water emulsions stabilised by solid lipid particles: the role of particle characteristics and emulsion microstructure upon Pickering functionality. *Food Funct* **8**, 2583 (2017).

41. Yang, M., Liu, F. & Tang, C. H. Properties and microstructure of transglutaminase-set soy protein-stabilized emulsion gels. *Food Research International* **52**, 409–418 (2013).

42. Barden, L., Vollmer, D., Johnson, D. & Decker, E. Impact of iron, chelators, and free fatty acids on lipid oxidation in low-moisture crackers. *J Agric Food Chem* **63**, 1812–1818 (2015).

43. Ye, L. *et al.* Using Confocal Microscopy to Estimate the Distribution of Natural Antioxidants in Poultry Meal and Extruded Kibbles. *European Journal of Lipid Science and Technology* **121**, (2019).

44. Raudsepp, P., Brüggemann, D. A. & Andersen, M. L. Detection of radicals in single droplets of oil-in-water emulsions with the lipophilic fluorescent probe BODIPY665/676 and confocal laser scanning microscopy. *Free Radic Biol Med* **70**, 233–240 (2014).

45. Raudsepp, P., Brüggemann, D. A. & Andersen, M. L. Evidence for transfer of radicals between oil-in-water emulsion droplets as detected by the probe (E, E)-3, 5-bis (4-phenyl-1, 3-butadienyl)-4, 4-difluoro-4-bora-3a, 4a-diaza-s-indacene, BODIPY665/676. *J Agric Food Chem* **62**, 12428–12435 (2014).

46. Naguib, Y. M. A. Antioxidant activities of astaxanthin and related carotenoids. *J Agric Food Chem* **48**, 1150–1154 (2000).

47. Laguerre, M., Lecomte, J. & Villeneuve, P. Evaluation of the ability of antioxidants to counteract lipid oxidation: Existing methods, new trends and challenges. *Prog Lipid Res* **46**, 244–282 (2007).

48. Banerjee, C., Westberg, M., Breitenbach, T., Bregnhøj, M. & Ogilby, P. R. Monitoring Interfacial Lipid Oxidation in Oil-in-Water Emulsions Using Spatially Resolved Optical Techniques. *Anal Chem* **89**, 6239–6247 (2017).

49. Mosca, M., Cuomo, F., Lopez, F. & Ceglie, A. Role of emulsifier layer, antioxidants and radical initiators in the oxidation of olive oil-in-water emulsions. *Food Research International* **50**, 377–383 (2013).

3

Quantitative spatiotemporal mapping of lipid and protein oxidation in mayonnaise

Abstract

Lipid oxidation in food emulsions is mediated by emulsifiers in the water phase and at the oil-water interface. To unravel the physico-chemical mechanisms and to obtain local lipid and protein oxidation rates, we used confocal laser scanning microscopy (CLSM), thereby monitoring changes in both the fluorescence emission of a lipophilic dye BODIPY 665/676 and protein autofluorescence. Our data show that the removal of lipid-soluble antioxidants from mayonnaises promotes lipid oxidation within oil droplets as well as protein oxidation at the oil-water interface. Furthermore, we demonstrate that ascorbic acid acts as either a lipid antioxidant or pro-oxidant depending on the presence of lipid-soluble antioxidants. The observed protein oxidation at the oil-water interface was spatially heterogeneous, which is in line with the heterogeneous distribution of lipoprotein granules from the egg yolk used for emulsification. The impact of the droplet size on local lipid and protein oxidation rates was significant (p < 0.0001) but minor compared to the effects of ascorbic acid addition and lipid-soluble antioxidant depletion. The presented results demonstrate that CLSM can be applied to unravel the roles of colloidal structure and transport in mediating lipid oxidation in complex food emulsions.

3.1   Introduction

Unsaturated fatty acids are nutritionally important[1] and often consumed in emulsified form, such as infant formula, milk, mayonnaise, and dressings. The physical stability of these food emulsions is enhanced by surface-active lipids and proteins at the oil-water interface[2,3]. The presence of these emulsifiers, however, compromises chemical stability by promoting lipid oxidation, which leads to off-flavors and compromised nutritional value[4]. Consequently, understanding and controlling lipid oxidation is an area of active research, with studies predominantly focusing on the chemical fate of lipids upon oxidation[2,5–7]. At the initial stage of lipid oxidation, unsaturated lipids produce lipid free radicals. During the propagation phase, these radicals react with oxygen and produce peroxyl radicals, which produce hydroperoxides that ultimately degrade to volatile off-flavors. In food emulsions, it is known that these reactions are catalyzed at the droplet interface and that antioxidants can be active in the lipid droplet phase, the water phase, and at the oil-water interface[8,9]. Furthermore, there is growing evidence that colloidal surface heterogeneity and the transport of oxidation reaction intermediates also play a critical role in the onset and the rate of oxidation[10,11].

Several routes for the role of mass transport of lipid oxidation in food emulsions have been proposed in the literature[11]. In comparison to the diffusional transport of individual hydrophobic lipid oxidation intermediates in the aqueous phase, droplet-droplet contacts could present a more efficient exchange mechanism. An even more efficient way to transfer oxidation intermediates between droplets could be micellar transport, aided by the presence of emulsifiers that are not adsorbed at droplet interfaces. This micelle-assisted transfer has been proposed as the main accelerator of lipid oxidation, as the amount of emulsifiers used for stabilizing food emulsions is sufficient to form micelles[2]. According to this micelle-assisted transfer hypothesis, the rate of lipid oxidation can be modulated by controlling the concentration of emulsifiers.

Besides propagation of lipid oxidation, free lipid radicals can also engage in the oxidation of proteins present at droplet interfaces and in the continuous water phase. There is, however, scarce information on the cause-effect relationships in lipid-protein co-oxidation[12]. Progress has been impeded by a lack of methods that can provide spatial insights into the co-oxidation of lipids and proteins.

Whereas the effects of various ingredients that delay lipid oxidation in food emulsions have been widely studied at the ensemble level[6,8,13], there is scarce or even ambiguous support for current hypotheses on the spatial and temporal heterogeneity of lipid oxidation[12,14]. Variation in oil droplet size has been proposed as a factor in the spatiotemporal heterogeneity of lipid oxidation. Some publications suggested that smaller lipid droplets have a higher rate of oxidation due to their larger surface area to volume ratio[5,15,16] whereas others showed that the droplet size itself

has no significant effect on the rate of lipid oxidation[17–21]. In the water phase, the composition of anti/pro-oxidants, including ascorbic acid, unadsorbed proteins, and metal iron, can inhibit or promote the formation and diffusion of reactive species dependent on their concentration and the pH value of the emulsions[13,22]. These anti/pro-oxidants further influence the characteristics of the interfacial layer and can change the oxidation rate by having the role of metal chelators as well as free radical scavengers at the oil-water interface[2].

The fluorophore BODIPY 665/676 and other dyes of the series have been widely used for studying lipophilic structures as it is sensitive to peroxyl radicals[23–26]. Recently, the role of mass transport in lipid oxidation between droplets in emulsions was studied using flow cytometry[24]. This technique, however, does not allow the individual droplets to be followed in situ over time, nor does it distinguish whether and to which extent oxidation occurs at the interface or the continuous phase.

Here, we present a method that can assess oxidation in a time-dependent manner in three distinct phases: (1) lipid oxidation in the dispersed oil phase, (2) protein oxidation in the continuous water phase, and (3) protein oxidation at the oil-water interface. We assessed lipid oxidation of oil droplets in mayonnaise using BODIPY 665/676, which changes its fluorescence emission from red to green after interaction with radicals, and we evaluated protein oxidation by detecting protein autofluorescence[27–29] in both the aqueous phase and interface.

3.2 Materials and Method

3.2.1 Materials

The lipophilic and oxidation-sensitive dye BODIPY 665/676 was purchased from Thermo Fischer (Waltham, MA, USA). L-ascorbic acid, sodium chloride (>99.5%, EMSURE®), and alumina power (Alumina N—Super I) were obtained from Aldrich-Europe (Darmstadt, Germany), MilliporeSigma (Burlington, MA, USA), and MP EcoChrom™ (Eschwege, Germany), respectively. Spirit white vinegar (4%), soybean oil, and egg yolk containing 8% (w/w) NaCl were purchased from a local store. Demineralized (demi) water was used for all experiments.

3.2.2 Preparation of oil samples

Soybean oil was stripped using alumina powder to remove lipid-soluble antioxidants [22]. The powder was mixed with the oil at a volume ratio of 1:2 in Falcon tubes, and the mixture was shaken in the dark for 24 h. The mixture was then centrifuged at 2000× g for 20 min to separate the stripped soybean oil. The oil was collected, and the same centrifugation procedure was repeated to ensure the complete removal of the alumina powder. BODIPY 665/676 was

dissolved in soybean oil or stripped soybean oil to a final concentration of 1 µM, which is too low to act as an antioxidant[30].

3.2.3   Preparation of Emulsions

Mayonnaise was prepared using a Silverson mixer: 78% (w/w) of soybean oil, 5% (w/w) of egg yolk with 8% (w/w) NaCl, 0.72% (w/w) of sodium chloride, 11.75% (w/w) demi water, and 4.53% (w/w) spirit vinegar. Egg yolk, salt, demi water, and the half volume of vinegar were premixed in a 500-mL jar and mixed at 2000 rpm for 20 s. Oil containing 1 µM BODIPY 665/676 was slowly added and mixed at 8500 rpm for 4 min. Spirit vinegar was added and mixed further for 2 min. For the manipulation of oxidation via a water-soluble agent, we prepared a stock solution of 2.1 g of L-ascorbic acid in 6.5 mL of demi water. To obtain a 10 mM final concentration of L-ascorbic acid, 1.1 mL of stock solution was gently stirred into 180 g of mayonnaise.

Mayonnaises were prepared with either soybean or stripped soybean oil, in which native oil-soluble antioxidants were removed. Additionally, we performed measurements with and without ascorbic acid (**Table 3.1**).

Table 3.1. The four mayonnaises studied were prepared with soybean oil (SO, Sample I), soybean oil with ascorbic acid (SO + aa, Sample II), stripped soybean oil (SSO, Sample III), stripped soybean oil with ascorbic acid (SSO + aa, Sample IV).

	Sample	**Lipid Soluble Antioxidant**
I	Soybean oil (SO)	+
II	Soybean oil + ascorbic acid (SO + aa)	+
III	Stripped soybean oil (SSO)	−
IV	Stripped soybean oil + ascorbic acid (SSO + aa)	−

3.2.4   Accelerated Oxidation of Samples

For imaging measurements, the emulsions (200 µL each) were placed into separate µ-slide wells and stored at 30 °C to accelerate the oxidation (**Figure 3.1a**). For the measurements in the fluorescence spectrophotometer, 15 samples with 1.5 mL of emulsions in 2 mL Eppendorf tubes were stored at 30 °C. Every day, a sample was placed in a −20 °C freezer to stop oxidation. After 15 days, the samples were thawed, resulting in the separation of the oil and water phases. Clean oil phases were obtained by centrifuging the phase-separated emulsion at 2000× g for 5 min and removing the water phase.

3.2.5   Preparation of sample carrier

To monitor lipid droplets at the same location over time, we engraved an "x" into the bottom of a glass sample carrier (µ-slide 8-well glass bottom, ibidi®, Munich, Germany) using a diamond knife (**Figure 3.1a**). The carrier was then plasma cleaned (1 min) to remove organic contaminations from the glass and to prevent the absorption of oil droplets to the surface. After placing the samples in the carrier, a lid was glued on to it using an epoxy resin to prevent evaporation. The carrier was then placed on a confocal laser scanning microscope (CLSM, Leica SP8, Wetzlar, Germany) such that the same position could be revisited on consecutive days.

3.2.6   Confocal Laser Scanning Microscopy (CLSM)

Monitoring of lipid and protein oxidation was carried out on a CLSM (Leica SP8, Wetzlar, Germany) equipped with a 63x NA = 1.2 water immersion objective (HC PLAPO CS2, Leica, Wetzlar, Germany) and a white-light laser with user-selectable excitation wavelengths. The scanning format was 512×512 pixels (123 µm by 123 µm), and the line-scanning speed was set to 100 Hz. The excitation wavelength was set to 561 nm to detect oxidized lipids with BODIPY 665/676 (detection range from 580 to 660 nm, green channel) or 640 nm to measure non-oxidized lipids (detection range from 660 to 750 nm, red channel). To detect protein oxidation, samples were excited at 488 nm and fluorescence emission was detected between 500 and 560 nm (blue channel). Images were tracked 15 days for sample I and II and 10 days for samples III and IV.

3.2.7   Spectrophotometry

The emission spectra of BODIPY 665/676 were measured with a fluorescence spectrophotometer (Fluorlog 322, Horiba, Kyoto, Japan). The laser excitation and the detection range of emission were the same as with the measurements in CLSM (λ_{ex} 561/640 nm, λ_{em} 580-660/660-750 nm). The final concentration of BODIPY in oil was calculated from the absorption coefficients determined with an absorption spectrophotometer (Cary4000, Santa Clara, CA, USA).

3.2.8   Segmentation and Tracking

For segmentation in StarDist[31], we set the percentile low and high values to 1 and 99.8, respectively. The probability/score threshold was set to 0.5, and the overlap threshold was 0.4. For the neural network prediction, we used the versatile (fluorescence nuclei) model. For tracking in Trackmate[32], the calibration settings were 1 pixel for pixel width, height, and voxel depth. The time interval was set to 1 frame, and a LoG detector was used. The estimated blob diameter was set to 14 pixels, and the threshold was set to 0. A median filter and sub-pixel localization option were used in combination with a simple LAP tracker option. Linking max

distance and gap-closing max distance were set to 15.0 pixels, and gap-closing max frame gap was set to 2. The filters were set on tracks above 9.9 (number of spots in track). After tracking, the label image was exported with the option of only spots in the tracks. For segmentation and tracking analyses, sample IV (SSO + aa) was not included as the fast oxidation led to extensive droplet coalescence.

3.2.9   Gompertz Curve Fitting

Local oxidation rates were determined using the Gompertz function,

$$f(t) = a \exp(-b \exp(-ct)) \tag{3.1}$$

where a, b, and c representing the asymptote of the curve, the displacement along the x-axis, and the growth rate. Lipid and protein oxidation data were fitted using least-squares regression with the Excel-solver (Version 2020, Microsoft Corporation, Redmond, Wash., USA). The obtained growth rates were used as indications for the local oxidation rate of lipids in oil droplets and proteins at the interface, respectively.

3.3   Results

3.3.1   Confocal microscopy allows spatiotemporal mapping of lipid and protein oxidation

We compared the oxidation kinetics for four different emulsions (SO, SO + aa, SSO, and SSO + aa, **Table 3.1**) in a modified sample carrier (**Figure 3.1a**). The carrier allowed us to track oil droplets at the same location over many days on a confocal laser scanning microscope (CLSM). As a proxy of lipid oxidation, we used BODIPY 665/676. In total, we monitored three spectral regions (**Materials and Methods**) to obtain spatially and temporarily resolved information on lipid and protein oxidation at the interface, in oil droplets, and in the continuous phase. The three spectral regions were then overlaid to obtain a single pseudo-color coded CLSM image for each condition (**Figure 3.1b**).

We will first qualitatively describe our observations before performing further quantitative analysis. On day one, samples I-III (SO, SO + aa, and SSO) showed similar fluorescence emission characteristics, with most of the fluorescence intensities originating from the red emission channel, indicating a similar non-oxidized state. Sample IV (SSO + aa), however, showed already increased intensities in the green and blue emission channels, indicating that lipids and proteins are already highly oxidized. On the third day, there was a modest increase of green emission in samples I-III and no increase in the blue channel for samples I and III (no aa).
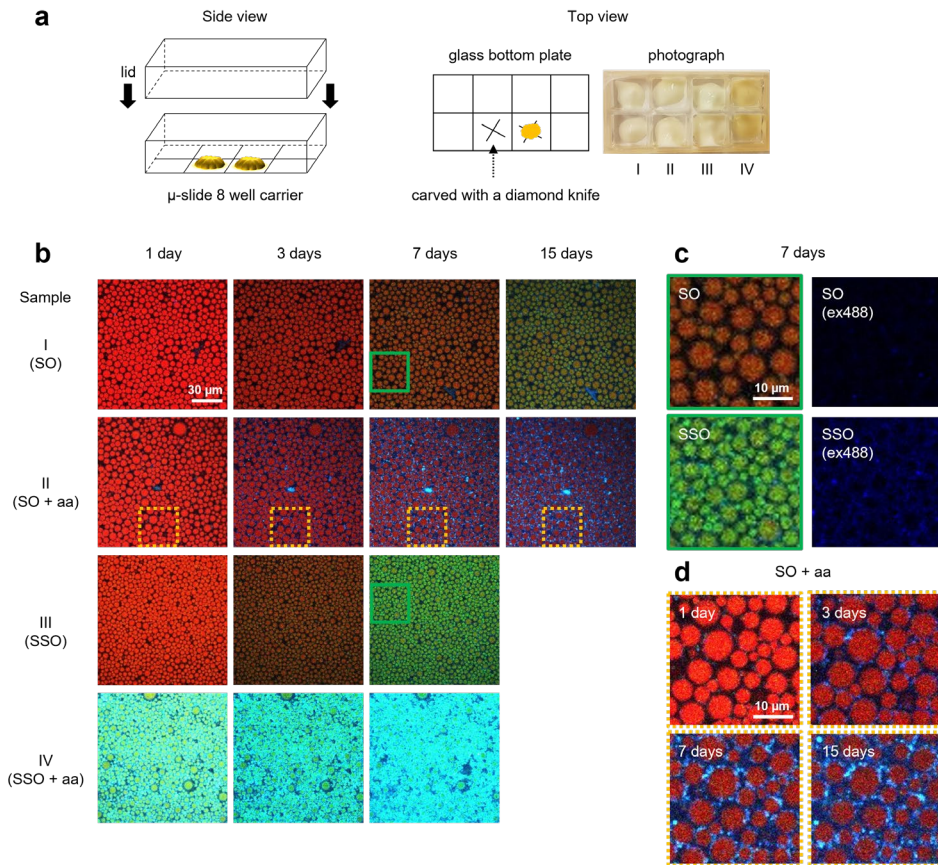
Figure 3.1. Experimental design and imaging oxidation in mayonnaise. (**a**) The side and top view of a modified sample carrier for monitoring the same field of view over time. Marks were engraved on the bottom of the glass slide using a diamond knife. The photograph shows the oxidized samples I-IV after one day at 30 °C. Sample IV shows the yellow color because of the fast oxidation. (**b**) Pseudo-color-coded CLSM images of mayonnaise containing BODIPY 665/676 stored for up to 15 days at 30 °C. Mayonnaise was made either using soybean oil (SO, Sample I), soybean oil with ascorbic acid (SO + aa, Sample II), stripped soybean oil (SSO, Sample III), or stripped soybean oil with ascorbic acid (SSO + aa, Sample IV). Images were combined from three different channels taken with λ_{ex} 640 nm and λ_{em} 660 – 750 nm (red), λ_{ex} 561 nm and λ_{em} 580 – 660 nm (green), and λ_{ex} 488 nm and λ_{em} 500 – 560 nm (blue). (**c**) Zoom-in of sample I (SO) and sample III (SSO) for seven days. The left column shows the combination of three channels and the right column shows only the blue channel (λ_{ex} 488 nm). (**d**) Zoom-in (yellow dashed box) of sample II (SO + aa) for day 1, 3, 7, and 15. Heterogeneous protein oxidation is visible throughout the continuous phase and near the oil-water interface. For details on how this figure was further processed for droplet segmentation, see **Figure S3.3**. The size of the images is 123 × 123 μm in (b) and 31 × 31 μm in (c), (d).

Whereas sample II (SO + aa) showed a modest increase in the blue channel for the aqueous phase, and sample IV (SSO + aa) showed high intensities in both the blue and the green detection channels. On day seven, a small increase of green emission was visible for sample I (SO) and a larger increase for sample III (SSO). Sample II (SO + aa) showed an increase in blue

fluorescence at the interface of oil droplets. After 15 days at 30 °C, the sample I (SO) showed dominant green fluorescence; in contrast, no significant increase in green fluorescence was seen in sample II (SO + aa). For samples III and IV (SSO, SSO + aa), the emulsion broke after 15 days, hence no data are shown. To support the general changes of lipid and protein oxidation, we further recorded data at different positions in the same sample carrier and with an independent repeat in a different carrier as well (**Figure S3.1**).

To comprehend the effect of stripping the soybean oil, close-up images of the areas depicting samples I and III (SO and SSO) in the absence of ascorbic acid are presented in **Figure 3.1c**. Both samples showed similar levels of red emission fluorescence on day one. Interestingly, both green and blue emissions, indicating oxidized lipids and proteins respectively, were higher after seven days in sample III (SSO) than in sample I (SO). To further evaluate the role of ascorbic acid, samples I and II (SO and SO + aa) were compared. Lipids were not fully oxidized even after 15 days and blue spots appeared to increase heterogeneously around the oil droplets, indicating that ascorbic acid acted as a protein pro-oxidant in sample II (SO + aa, **Figure 3.1d**). The finding of ascorbic acid acting here as a lipid antioxidant is further supported by the spectral ensemble measurements (**Figure S3.2**).

3.3.2   Quantitative spatiotemporal analysis of lipid and protein oxidation maps

The analysis of intensity changes in individual droplets as a function of time is not a trivial task. Challenges involve the identification and separation of individual droplets from the water phase in emulsions and the tracking of individual droplets over many days. To solve this, we first segmented the droplets from CLSM data using the deep learning-based software 2D StarDist[31]. To this end, we used the red channel of the CLSM images for segmentation (**Figure 3.2a & b**) and applied the segmentation mask to the original three-color images using MATLAB R2019a. This approach allowed us to obtain three-segmented channels representing (**Figure 3.2c**) (1) non-oxidized lipids in oil droplets (red channel, ex 640 nm), (2) oxidized lipids in oil droplets (green channel, ex 561nm), and (3) oxidized proteins at the interface (blue channel, ex 488 nm). **Figure 3.2c** further shows the image containing the oxidized proteins in the aqueous phase obtained by applying and inverting the segmentation mask. After segmentation, the number of droplets was 600, 601, and 910, respectively, and the average radius size of droplets was 2.2, 2.1, and 1.8 µm for samples I-III (**Table 3.2**).

We then tracked individual droplets using Trackmate[32]. To this end, we first stacked the segmented images representing the same location in the sample monitored over 10 days (**Figure 3.2d**). Only droplets that could be successfully tracked for the entire duration were analyzed further. As Trackmate does not support monitoring different changes in the size of the tracked objects, we assigned a tracking number to each droplet and re-processed the data if necessary

(**Figure S3.4**). The number of droplets and their average radii are given in **Table 3.2**. Using the segmented and tracked images, we then analyzed the local oxidation rate of each droplet.
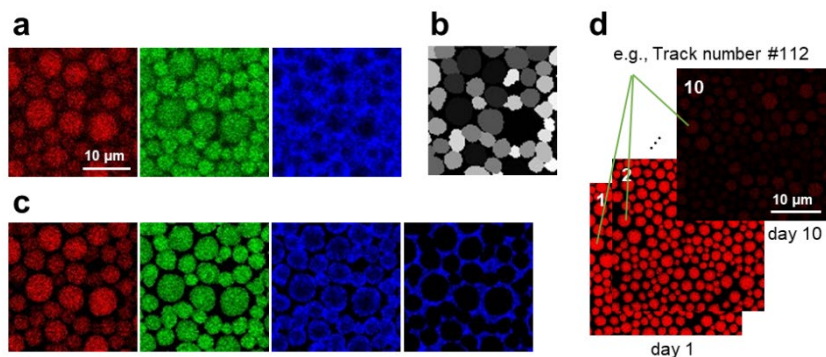

Figure 3.2. Workflow for the segmentation and tracking of individual oil droplets. (**a**) Original images (raw data) were collected in three separate channels (red, green, and blue). (**b**) Droplets were segmented using StarDist. (**c**) Segmented images were reconstructed by applying the segmentation mask to the original images. The blue channel images represent intensity within and outside the mask corresponding to oxidized proteins at the interface and in the continuous phase. (**d**) Segmented images that have clear borders were stacked together for tracking. Each droplet was tracked using Trackmate for up to 10 days. Tracking numbers were allocated to individual droplets. Scale bars represent 10 µm in (a-d).

Table 3.2. The number of droplets and average radius size from analyses for samples I, II, and III (see **Table 3.1**).

Results	Number of Analyzed Droplets			Average Radius Size (µm) [3]		
Sample	I	II	III	I	II	III
StarDist [1]	600	601	910	2.2 ± 0.6	2.1 ± 0.6	1.8 ± 0.4
Re-assigned after Trackmate [2]	484	445	641	2.2 ± 0.5	2.1 ± 0.5	2.0 ± 0.3

[1] Minimum number of droplets per sample from segmented images that were recorded over 10 days. [2] Re-assigned details are explained in **Figure S3.4**. [3] The standard deviation in droplet radius sizes is shown with the average radius size.

For oxidized proteins at the oil-water interface, sample I (SO) showed only small changes in the fluorescence intensities (mean intensity = 2.0 ± 0.7 photons per pixel) for 10 days (**Figure 3.3a**). In sample II (SO + aa), the mean intensities increased from 2.5 to 5.8 photons per pixel, showing a faster increase at the initial stage of oxidation. Sample III (SSO) did not show any changes at the initial stage (1.8 and 1.9 photons per pixel for day one and day four, respectively) but showed an increase in fluorescence after six days, leading to 7.5 photons per pixel on day 10. For oxidized proteins in the aqueous phase, the intensity changes were similar to the protein oxidation at the interface. We did not observe an increase in sample I. Sample II (SO + aa)

showed the increase only in the initial stage of oxidation and at the latest stage of oxidation, sample III (SSO) had a similar oxidation level with sample II (SO + aa).

To compare the degree of lipid oxidation in individual droplets, we divided the average BODIPY 665/667 fluorescence intensity of the green channel by the sum intensities of the green and the red channel (for the intensities in the individual channels, see **Figure S3.5**). The rate of lipid oxidation in sample III (SSO) is faster than the rates in samples I and II (SO, SO + aa, **Figure 3.3b**). The ratio reporting on the degree of oxidation after 10 days is 0.85 for sample III (SSO) and 0.39 and 0.32 for sample I (SO) and sample II (SO + aa), respectively. The average lipid oxidation ratio of sample I (SO) is 18% higher than the ratio of sample II (SO + aa), indicating that ascorbic acid acted as an antioxidant for lipids.

The individual oxidation rates of lipids and proteins were further quantified by fitting the data from **Figure 3.3a** and **Figure S3.5a** with a Gompertz function (**Materials and Methods**). Here, we defined the growth parameter 'c' as the local oxidation rate and calculated the rates c_{lip} and c_{prot} for lipids in oil droplets and proteins at the droplet interface, respectively. These local oxidation rates were plotted against the inverse of the droplet radius (**Figure 3.3c**) because of the expected inverse relation between the surface area of droplets exposed to the continuous phase and the droplet radius[6,33]. For quantitative evaluation, we performed regression analyses on the lipid (c_{lip}) and protein (c_{prot}) oxidation rate with the inverse droplet radius within the groups (**Figure 3.3c**). For the protein oxidation formulations (c_{prot}), they showed a significant dependency of the local protein oxidation rates on the inverse of the droplet radius in all samples ($p < 0.0001$). For the lipid oxidation rates (c_{lip}), only sample II (SO + aa) showed a significant inverse droplet size dependency ($p < 0.0001$). To assess whether the weak effect of the droplet size on the local oxidation rate was due to inter-droplet exchange of dye, we mixed emulsions prepared with and without BODIPY 665/676. Within 10 days, the timeframe of our oxidation experiments, the peak fluorescence intensity in undyed droplets had increased by 45% (**Figure S3.6**). The calculated oxidation rates, however, are determined on a shorter time frame and the exchange of BODIPY 665/676 between droplets may therefore only partially contribute to averaging out the effect of the droplet size on the lipid oxidation rate.
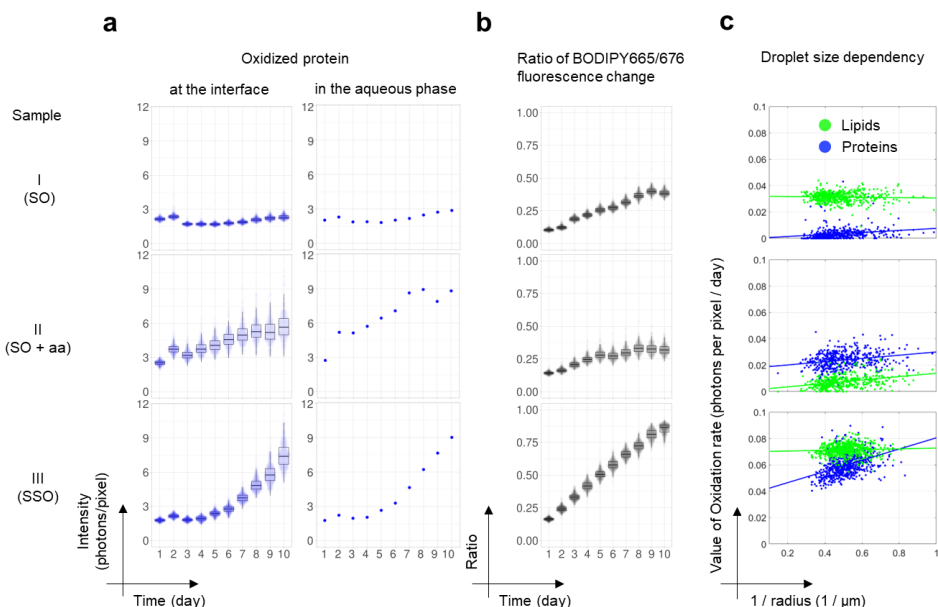
Figure 3.3. Statistical analyses of protein and lipid oxidation. (a + b) The data are visualized using PlotsOfData[34]. Each data point represents the average intensity of individual droplets. Black boxes indicate the 95% confidence interval (95CIs) of the data and the center line indicates the median value. (**a**) Intensity changes of protein oxidation at the interface and the aqueous phase. For the numbers of analyzed droplets (left column), see **Table 3.2**; for the aqueous phase (right column), we obtained a single number from the entire field of view. (**b**) The ratio of BODIPY 665/676 fluorescence intensity changes is presented as a measure of lipid oxidation. The average intensity per droplet from λ_{ex} 561 nm (oxidized lipids) was divided by the sum intensity from λ_{ex} 640nm (non-oxidized lipids) and λ_{ex} 561 nm (oxidized lipids). (**c**) The effect of the inverse droplet size on the oxidation rate of lipids within droplets (green color) and protein at/near interfaces (blue color) based on changes in fluorescence intensity. Dots show the local lipid oxidation rate as obtained from fitting the time dependency of BODIPY 665/676 color shifts and protein fluorescence changes in individual droplets with the Gompertz function. Lines show the regression analysis result of local lipid (green line) and protein (blue line) oxidation rates on the inverse of droplet sizes.

3.4 Discussion

In this study, we show that ascorbic acid takes on different roles on lipids depending on the availability of lipid-soluble antioxidants, such as tocopherol. In the non-stripped sample II (SO + aa), the antioxidant role of ascorbic acid for lipids is dominant over a pro-oxidant effect via redox cycling of transition metals, likely ferric (Fe^{3+}) to ferrous (Fe^{2+}) ions, at the lipid droplet interface (**Figure 3.4a**). We note that all mayonnaises in this study were prepared at low pH, where reduced binding strength to phosvitin allows for effective ferric-ferrous redox cycling[22,35]. In the stripped sample IV (SSO + aa), the ascorbic acid can no longer work in synergy with tocopherol and its pro-oxidant role becomes dominant (**Figure 3.4b**). Hence, for this emulsion (sample IV), we observed rapid lipid oxidation. This observation is in line with the pro-oxidant

effect of ascorbic acid on lipids in mayonnaises prepared with fish oil, which has a low concentration of α-tocopherol[22].

Whereas ascorbic acid had different roles in lipid oxidation, it always acted as a pro-oxidant on proteins in the aqueous phase and at the interface (samples II and IV). As a pro-oxidant (**Figure 3.4b**), ascorbic acid interacts with transition metals that are known to promote lipid oxidation by propagating lipid hydroperoxide (LOOH) formation at the interface of dispersed oil droplets[13,22]. Our results show that ascorbic acid also acts as a pro-oxidant for proteins at the interface and in the water phase. The heterogeneous distribution of protein oxidation at the interface in sample II (SO + aa, **Figure 3.1d**) points towards lipoprotein granules that are typically present in egg yolk of mayonnaises[36–38]. Additionally, here, ascorbic acid can interact with transition metals, such as iron and copper, that are known to catalyze lipid oxidation in lipoprotein particles[29]. It has been shown that lipid oxidation in lipoproteins can induce oxidation of constituent apoproteins, which becomes apparent as increased protein autofluorescence in the visible wavelength region[29].

We attribute the faster lipid oxidation in sample III (SSO, **Figure 3.1b**) to the absence of α-tocopherol. α-Tocopherol is naturally present in vegetable oils (sample I, SO) and is known to act as a chain-breaker in radical reactions by trapping lipid radicals and forming tocopherol radicals[6,9,39,40] (**Figure 3.4a**). Our experimental results show that in the absence of tocopherol, protein oxidation is also enhanced at the interface and in the continuous phase (sample I (SO) vs. III (SSO)), with the heterogeneous distribution of oxidized proteins pointing towards the involvement of lipoprotein granules. We attribute the enhanced protein oxidation upon removal of tocopherol to the transport of lipid radicals from the oil droplets to the interface and continuous phase[12].

Several studies have suggested that the rate of lipid oxidation in emulsions depends on the droplet size, typically when covering a large range of average droplet sizes[15,33]. In our case, only for sample II (SO+aa), a significant but weak, linear dependency of local lipid oxidation rate with the inverse of droplet size could be observed. A partial explanation can be the inter-droplet exchange of BODIPY 665/676, as indicated by the experiment where we mixed emulsions with and without dye. As a more likely explanation, we propose the inter-droplet exchange of lipid oxidation intermediates, such as hydroperoxides. The exchange of such intermediates can be facilitated by their intrinsic amphiphilic character in combination with micellization by non-adsorbed emulsifiers[11]. This precludes lipid droplets to have a size dependency on the lipid oxidation rate. Moreover, we note that in our emulsions, the distribution of droplet sizes was relatively small (radius range 1–4 μm). For a larger difference in droplet radius, the aforementioned transport mechanism may be less effective in averaging out the droplet size effect for lipids. The inter-droplet exchange effect will not be less effective for proteins adsorbed

at the interface, which explains why we could consistently observe significant but small effects of the inverse droplet size on the oxidation rate of proteins at the droplet interface.
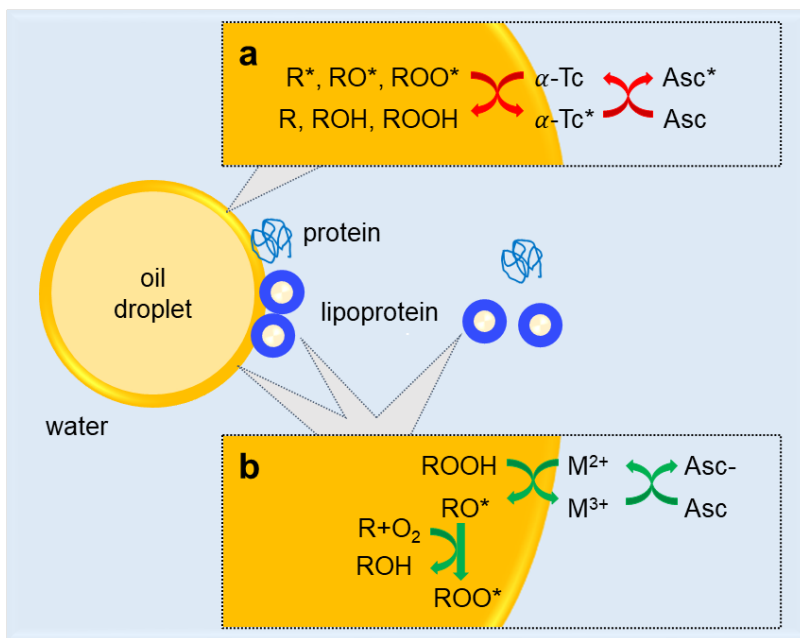

Figure 3.4. Overview of the mechanisms of lipid and protein oxidation present in oil-in-water emulsions. Oil droplets are shown in yellow; lipoprotein particles are presented with a yellow lipid core and a blue protein shell. For simplicity, these particles are not shown in their aggregated form in granules. Anti/pro-oxidant mechanisms are depicted at the interfacial droplet layer and at the lipoprotein surface. Anti- and pro-oxidant mechanisms are respectively indicated in red and green. (**a**) Ascorbic acid acts as an antioxidant for lipids by converting tocopherol radicals to tocopherol. (**b**) Pro-oxidant behavior of ascorbic acid on lipids and proteins, including lipoproteins, at the interface and the water phase. Mechanisms involve metal chelation as well as free radical scavenging. ROOH: lipid hydroperoxide; R: unsaturated lipids; R^*: alkyl radical; RO^*: alkoxyl radical; ROO^*: peroxyl radical; ROH: hydroxy lipids; Asc: ascorbic acid; Asc^-: dehydroascorbic acid; Asc^*: ascorbyl radical; Tc: tocopherol; Tc^*: tocopherol radical. M^{2+}: Transition metal ions (Fe or Cu).

3.5 Conclusions

This study demonstrates a CLSM imaging method that can provide spatiotemporal maps of lipid and protein oxidation in mayonnaise via changes in BODIPY 665/676 fluorescence emission and protein autofluorescence. Local oxidation rates of lipids within dispersed oil droplets and proteins at the interface or in the continuous water phase can be quantitively assessed via segmentation and tracking of individual droplets and fitting with a semi-empirical model. Removal of lipid-soluble antioxidants by oil stripping promotes lipid oxidation within oil droplets as well as protein oxidation at the interface. In the presence of tocopherol, ascorbic acid acts as a lipid antioxidant and as a protein pro-oxidant in the water phase. The heterogeneous distribution of oxidized proteins points towards remnant lipoprotein granules from the egg yolk

used for emulsification. The spatially heterogeneous oxidation of proteins at the interface is in line with the heterogeneous distribution of micron-scale granules consisting of aggregated nanoscale lipoprotein particles. Upon depletion of lipid-soluble antioxidants, ascorbic acid acts as a pro-oxidant for both proteins and lipids. For mayonnaise protected by antioxidants, the impact of droplet size was minor compared with the effects of ascorbic acid addition and lipid-soluble antioxidant depletion. Our method can be deployed for spatially resolved assessment of lipid oxidation in heterogeneous food systems and to unravel the colloidal structure and transport mechanisms at play there.

3

References

1. Ganesan, B., Brothersen, C. & McMahon, D. J. Fortification of Foods with Omega-3 Polyunsaturated Fatty Acids. *Crit Rev Food Sci Nutr* **54**, 98–114 (2014).
2. Berton-Carabin, C. C., Ropers, M. H. & Genot, C. Lipid Oxidation in Oil-in-Water Emulsions: Involvement of the Interfacial Layer. *Compr Rev Food Sci Food Saf* **13**, 945–977 (2014).
3. Berton-Carabin, C. & Schroën, K. Towards new food emulsions: designing the interface and beyond. *Current Opinion in Food Science* vol. 27 74–81 (2019).
4. Serini, S., Fasano, E., Piccioni, E., Cittadini, A. R. M. & Calviello, G. Dietary n-3 polyunsaturated fatty acids and the paradox of their health benefits and potential harmful effects. *Chemical Research in Toxicology* vol. 24 2093–2105 (2011).
5. Mcclements, D. J. & Decker, E. A. *Lipid Oxidation in Oil-in-Water Emulsions: Impact of Molecular Environment on Chemical Reactions in Heterogeneous Food Systems. 1270 JOURNAL OF FOOD SCIENCE* vol. 65 (2000).
6. McClements, D. J. & Decker, E. Interfacial Antioxidants: A Review of Natural and Synthetic Emulsifiers and Coemulsifiers That Can Inhibit Lipid Oxidation. *Journal of Agricultural and Food Chemistry* vol. 66 20–25 (2018).
7. Laguerre, M., Bily, A. & Birtić, S. Lipid oxidation in food. in *Lipids and Edible Oils: Properties, Processing and Applications* 243–287 (2019).
8. Decker, E. A. *et al.* Hurdles in Predicting Antioxidant Efficacy in Oil-in-water emulsions. *Trends in Food Science and Technology* vol. 67 183–194 (2017).
9. Laguerre, M., Lecomte, J. & Villeneuve, P. Evaluation of the ability of antioxidants to counteract lipid oxidation: Existing methods, new trends and challenges. *Progress in Lipid Research* vol. 46 244–282 (2007).
10. Berton, C., Genot, C., Guibert, D. & Ropers, M. H. Effect of lateral heterogeneity in mixed surfactant-stabilized interfaces on the oxidation of unsaturated lipids in oil-in-water emulsions. *J Colloid Interface Sci* **377**, 244–250 (2012).
11. Laguerre, M., Bily, A., Roller, M. & Birtić, S. Mass Transport Phenomena in Lipid Oxidation and Antioxidation. *Annual Review of Food Science and Technology* vol. 8 391–411 (2017).
12. Schaich, K. M. *Co-oxidations of oxidizing lipids: Reactions with proteins. Chapter* vol. 8 (2008).
13. Ghorbani Gorji, S., Smyth, H. E., Sharma, M. & Fitzgerald, M. Lipid oxidation in mayonnaise and the role of natural antioxidants: A review. *Trends in Food Science and Technology* vol. 56 88–102 (2016).
14. Laguerre, M., Tenon, M., Bily, A. & Birtić, S. Toward a Spatiotemporal Model of Oxidation in Lipid Dispersions: A Hypothesis-Driven Review. *European Journal of Lipid Science and Technology* **122**, (2020).
15. Gohtani, S., Sirendi, M., Yamamoto, N., Kajikawa, K. & Yamano, Y. Effect of droplet size on oxidation of docosahexaenoic acid in emulsion system. *J Dispers Sci Technol* **20**, 1319–1325 (1999).
16. Yalçinöz, S. & Erçelebi, E. Effect of surfactant type and droplet size on lipid oxidation in oil-in-water nano-emulsions. *Quality Assurance and Safety of Crops and Foods* **12**, 1–11 (2020).
17. Sun, C. & Gunasekaran, S. Effects of protein concentration and oil-phase volume fraction on the stability and rheology of menhaden oil-in-water emulsions stabilized by whey protein isolate with xanthan gum. *Food Hydrocoll* **23**, 165–174 (2009).
18. Osborn, H. T. & Akoh, C. C. Effect of emulsifier type, droplet size, and oil concentration on lipid oxidation in structured lipid-based oil-in-water emulsions. *Food Chem* **84**, 451–456 (2004).
19. Kiokias, S., Dimakou, C. & Oreopoulou, V. Effect of heat treatment and droplet size on the oxidative stability of whey protein emulsions. *Food Chem* **105**, 94–100 (2007).
20. Roozen, J. P., Frankel, E. N. & Kinseha, J. E. *Enzymic and autoxidation of lipids in low fat foods: model of linoleic acid in emulsified hexadecane. Food Chemistry* vol. 50 (1994).
21. Erdmann, M. E., Lautenschlaeger, R., Zeeb, B., Gibis, M. & Weiss, J. Effect of differently sized O/W emulsions loaded with rosemary extract on lipid oxidation in cooked emulsion-type sausages rich in n-3 fatty acids. *LWT* **79**, 496–502 (2017).
22. Jacobsen, C., Timm, M. & Meyer, A. Oxidation in fish oil enriched mayonnaise: Ascorbic acid and low pH increase oxidative deterioration. *J Agric Food Chem* **49**, 3947–3956 (2001).
23. Raudsepp, P., Brüggemann, D. A. & Andersen, M. L. Detection of radicals in single droplets of oil-in-water emulsions with the lipophilic fluorescent probe BODIPY665/676 and confocal laser scanning microscopy. *Free Radic Biol Med* **70**, 233–240 (2014).
24. Li, P., McClements, D. J. & Decker, E. A. Application of flow cytometry as novel technology in studying lipid oxidation and mass transport phenomena in oil-in-water emulsions. *Food Chem* **315**, (2020).
25. Raudsepp, P., Brüggemann, D. A., Lenferink, A., Otto, C. & Andersen, M. L. Oxidative stabilization of mixed mayonnaises made with linseed oil and saturated medium-chain triglyceride oil. *Food Chem* **152**, 378–385 (2014).

26.   Banerjee, C., Westberg, M., Breitenbach, T., Bregnhøj, M. & Ogilby, P. R. Monitoring Interfacial Lipid Oxidation in Oil-in-Water Emulsions Using Spatially Resolved Optical Techniques. *Anal Chem* **89**, 6239–6247 (2017).

27.   Zamora, R. & Hidalgo, F. J. The Maillard reaction and lipid oxidation. *Lipid Technol* **23**, 59–62 (2011).

28.   Kokawa, M. *et al.* Predicting the Heating Temperature of Soymilk Products Using Fluorescence Fingerprints. *Food Bioproc Tech* **10**, 462–468 (2017).

29.   Aidyraliev, R. K., Azizova, O. A., Vakhrusheva, T. V, Lopukhin, Y. M. & Mirrakhimov, M. M. *Autofluorescence of Low-Density Lipoproteins Modified as a Result of Autooxidation. OctoberBulletin of Experimental Biology and Medicine* vol. 142 (2006).

30.   Berton, C., Genot, C. & Ropers, M. H. Quantification of unadsorbed protein and surfactant emulsifiers in oil-in-water emulsions. *J Colloid Interface Sci* **354**, 739–748 (2011).

31.   Schmidt, U., Weigert, M., Broaddus, C. & Myers, G. Cell detection with star-convex polygons. *Lecture Notes in Computer Science* **11071 LNCS**, 265–273 (2018).

32.   Tinevez, J. Y. *et al.* TrackMate: An open and extensible platform for single-particle tracking. *Methods* **115**, 80–90 (2017).

33.   McClements, D. J. Food emulsions : principles, practices, and techniques. *CRC press* (2015)

34.   Postma, M. & Goedhart, J. Plotsofdata—a web app for visualizing data together with their summaries. *PLoS Biol* **17**, (2019).

35.   Merkx, D. W. H., Delić, F., Wierenga, P. A., Hennebelle, M. & van Duynhoven, J. P. M. 31P NMR assessment of the phosvitin-iron complex in mayonnaise. *Magnetic Resonance in Chemistry* **57**, 540–547 (2019).

36.   Anton, M. Egg yolk: Structures, functionalities and processes. *Journal of the Science of Food and Agriculture* vol. 93 2871–2880 (2013).

37.   Sirvente, H. *et al.* Structuring and functionalization of dispersions containing egg yolk, plasma and granules induced by mechanical treatments. *J Agric Food Chem* **55**, 9537–9544 (2007).

38.   Pinchuk, I. & Lichtenberg, D. The effect of compartmentalization on the kinetics of transition metal ions-induced lipoprotein peroxidation. *Chem Phys Lipids* **195**, 39–46 (2016).

39.   Chaiyasit, W., Mcclements, D. J. & Decker, E. A. The Relationship between the Physicochemical Properties of Antioxidants and Their Ability to Inhibit Lipid Oxidation in Bulk Oil and Oil-in-Water Emulsions. *J Agric Food Chem* **53**, 4982–4988 (2005).

40.   Samdani, G. K., McClements, D. J. & Decker, E. A. Impact of Phospholipids and Tocopherols on the Oxidative Stability of Soybean Oil-in-Water Emulsions. *J Agric Food Chem* **66**, 3939–3948 (2018).
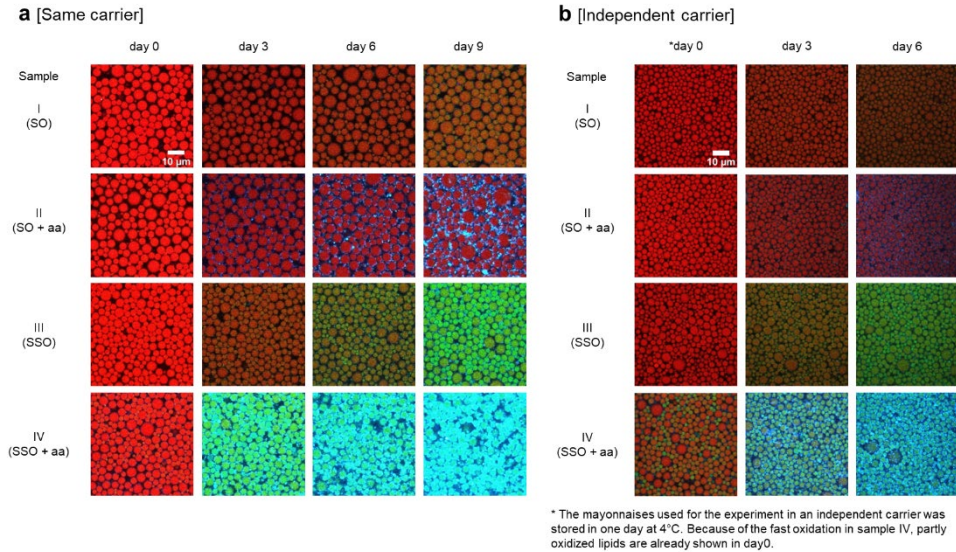
3

3.6   Appendix

Figure S3.1. The independent measurement of CLSM. (**a**) CLSM images of four different mayonnaises (sample I-IV) in different random positions. All samples showed the same tendency as **Figure 3.1b**. (**b**) The same experiment was conducted in an independent carrier. The image acquisition conditions are slightly different compared to the main figure. The scanning format was 1024 x 1024 pixels (62 x 62 μm), and the line-scanning speed was set to 100 Hz. The sample still shows the same tendencies in lipid and protein oxidation. Images were combined from three different channels taken with λ_{ex} 640 nm and λ_{em} 660-750 nm (red); λ_{ex} 561 nm and λ_{em} 580-660 nm (green); λ_{ex} 488 nm and λ_{em} 500-560 nm (blue).
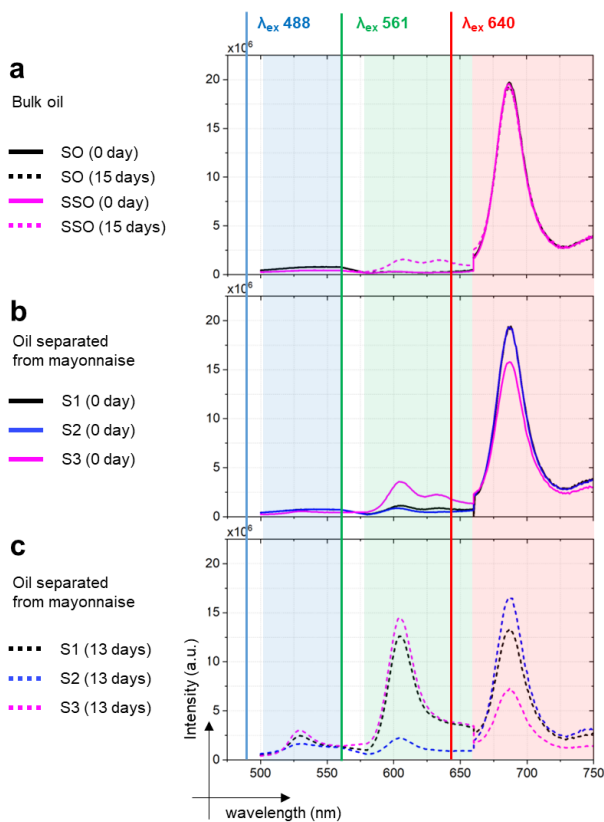
Figure S3.2. The spectral changes of BODIPY 665/676 in native oil and after retrieving the oil from the mayonnaise. Fluorescence emission spectra were measured for excitation at 488 nm, 561 nm, and 640 nm (colored vertical dashed lines). Colored areas show the range of detection. Blue channel: 500 - 560 nm, green channel: 580 - 660 nm, and red channel: 660 - 750 nm. (**a**) Native soybean oil (SO, black line) and native stripped soybean oil (SSO, magenta line) after 0 day (straight line) and 15 days (dashed line). In both native soybean oil (SO) and stripped soybean oil (SSO), the initial fluorescence intensity at day 0 was similar in all channels with a dominant emission peak around 680 nm after excitation at 640 nm. A slightly smaller intensity of SSO than SO in the blue channel reflects the depletion of tocopherol by stripping the oil. After storing the samples at 30 °C for 15 days, only SSO showed a small increase of emission in the green channel, indicating the presence of oxidation. (**b**) Retrieved oil from freeze-thaw emulsions after 0 days (straight line). Soybean oil (SO, black line), soybean oil with added ascorbic acid (SO + aa, blue line), and stripped soybean oil (SSO, magenta line). They showed higher fluorescence intensities in the green channel than the bulk oil samples due to the presence of pro-oxidants in emulsifiers. In the green channel, FL intensity of SSO was higher than SO suggesting that SSO was more prone to oxidation and SO + aa had similar intensities as the SO sample. In the red channel which shows the non-oxidized lipids, SO and SO + aa had a higher intensity than SSO. (**c**) Retrieved oil from freeze-thaw emulsions after 13 days (dashed line). After 13 days, the SSO sample showed a higher degree of oxidation than SO reflected by a higher intensity in the green channel and a larger drop of emission in the red detection channel. We further observed an unexpected peak around 530 nm in the blue channel in all samples, which we attribute to a second state of the oxidized BODIPY fluorophore. SO + aa showed a lower response with the green intensity of SO being 6 times higher than SO + aa thereby indicating that ascorbic acid has a role as an anti-oxidant on lipids. In stripped soybean oil, however, emulsions with ascorbic acid had a higher oxidation rate than without. This is because of the combined effects of tocopherol removal by stripping the oil and the presence of ascorbic acid in the aqueous phase.
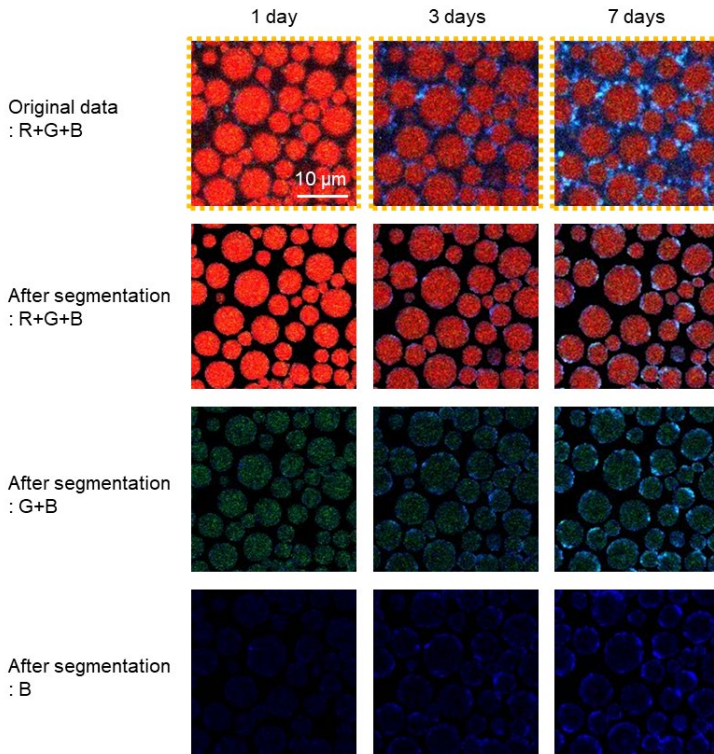
Figure S3.3. Segmentation applied with the channel. Original data and images after segmentation from **Figure 3.1d**. R: red channel, ex 640nm, G: green channel, ex 561nm, B: blue channel, ex 488nm.
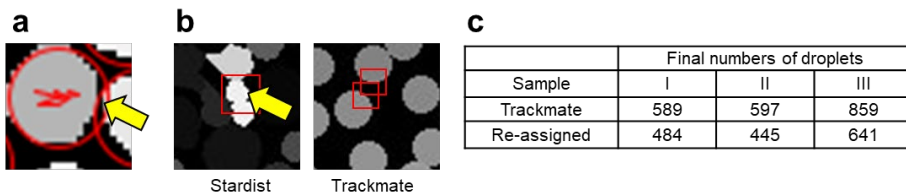

Figure S3.4. Re-assigning process after using Trackmate. As only a single blob diameter can be chosen for tracking analysis in Trackmate, one tracked number can be assigned in several droplets. (**a**) Example of overlapping tracking numbers. In this case, the droplet which has a larger area in the tracking number was chosen. (**b**) Tracked numbers from other droplets (Trackmate) can be assigned in non-tracked droplets (Stardist). One of them is randomly chosen if it is assigned with the same tracking area. Those are removed in the final steps by choosing the only droplets which are fully tracked for 10 days. (**c**) The final number of droplets for sample I-III after Trackmate and re-assigning process.
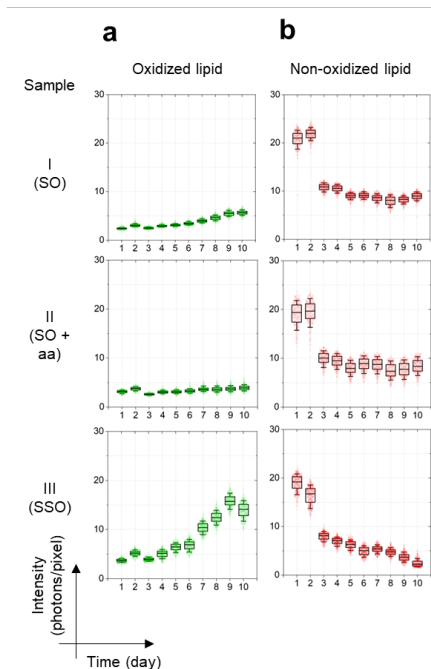
Figure S3.5. Fluorescence changes of oxidized and non-oxidized lipids in oil droplets. (**a**) For oxidized lipids in oil droplets, sample I (SO) showed a slow oxidation rate (2.43 photons per pixel on day 1, 5.68 on day 10) but was oxidized faster than sample II (SO + aa) with 3.15 on day 1 and 3.94 on day 10. Sample III (SSO) had highly increased FL after 6 days (1 day: 3.72, 6 days: 6.82, and 10 days: 13.97) and protein oxidation started to increase as well. On the other hand, sample II (SO + aa) had a high level of protein oxidation but it didn't influence lipid oxidation. (**b**) For non-oxidized lipids in oil droplets, fluorescence intensity of sample I and II (SO and SO + aa) is decreased from 20.86 to 8.97 and from 19.05 to 8.42 during 10 days, respectively, and sample III (SSO) showed a higher decrease rate from 18.98 to 2.43 photons per pixel.

3
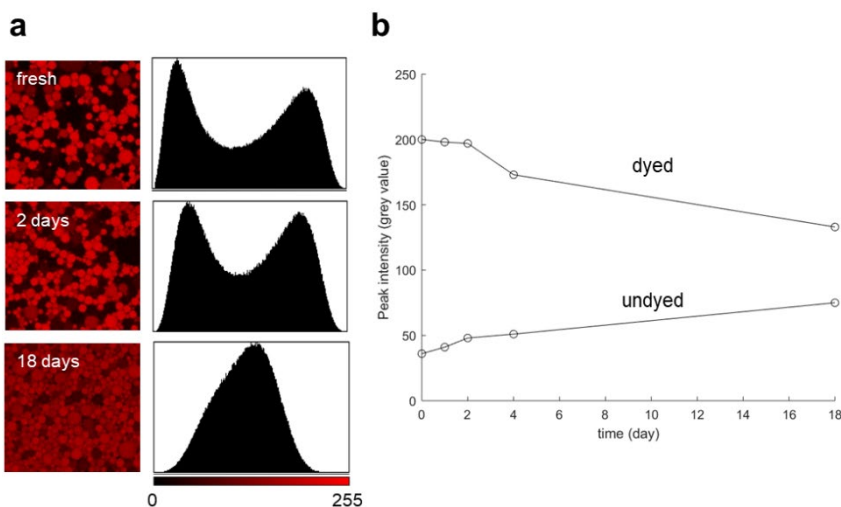
Figure S3.6. Diffusion measurements of BODIPY 665/676. Dye diffusion was tested by mixing dyed and undyed mayonnaise with the ratio 1:1. (**a**) CLSM images and their histograms (red (non-oxidized) channel only) of mixtures of dyed and undyed soybean oil mayonnaise (SO). The image size is 80 x 80 μm. Samples were stored at 22°C. (**b**) Peak positions of image histograms of mixtures of dyed and undyed mayonnaise as a function of time.

4

Unraveling mechanisms of protein and lipid oxidation in mayonnaise at multiple length scales

Abstract

In mayonnaise, lipid and protein oxidation are closely related and the interplay between them is critical for understanding the chemical shelf-life stability of mayonnaise. This is particularly the case for comprehending the role of low-density lipoprotein (LDL) particles acting as a main emulsifier. Here, we monitored oxidation and the concomitant aggregation of LDLs by bright-field light microscopy and cryogenic transmission electron microscopy. We further probed the formation of protein radicals and oxidation by imaging the accumulation of a water-soluble fluorescent spin trap and protein autofluorescence. The effect of the variation of pH and the addition of EDTA on the accumulation of the spin trap validated that protein radicals were induced by lipid radicals. Our data suggest two main pathways of oxidative protein radical formation in LDL particles: (1) at the droplet interface, induced by lipid free radicals formed in oil droplets, and (2) in the continuous phase induced by an independent LDL-specific mechanism.

4.1 Introduction

Mayonnaise derives its structural stability from egg yolk containing protein and lipid emulsifiers that reside at the oil-water droplet interface[1]. The use of egg yolk as an emulsifier, however, also introduces strong pro-oxidants[2]. Preventing oxidation of the oil phase and the proteins in mayonnaise has been a long-standing challenge, as oxidation can lead to reaction products that decrease the physical stability or the nutritional and sensorial value thereby limiting shelf-life. Mayonnaise is formulated with vegetable oil, vinegar and egg yolk. A major part of the proteins is associated with high-density lipoprotein (HDL) and low-density lipoprotein (LDL) particles and the remainder exists in free forms as phosvitins and livetins. LDL particles have a diameter of 40 ± 20 nm[1,3] and feature a core-shell structure where a core of triglycerides cholesteryl esters is surrounded by a monolayer of phospholipids and apolipoproteins. During the emulsification of mayonnaise, LDL particles can release phospholipids and apolipoproteins that together with phosvitin adsorb at the oil-water droplet interface. LDLs can also remain structurally intact and form granules present in the continuous phase or adsorbed at the oil-water interface depending on mechanical treatments and conditions[3,4].

Lipid oxidation in mayonnaise is mediated by free radical chain reactions[5] and catalyzed by the presence of metal ions such as iron introduced via phosvitin[6,7]. Reactions between alkyl radicals (L*) and molecular oxygen generate peroxyl radicals (LOO*), which further accelerate lipid peroxidation by reacting with unsaturated lipids. Whereas at neutral pH, pro-oxidant iron ions are strongly bound to the negatively charged phosvitin, a weaker binding at the acidic pH of mayonnaise makes the iron ions available as catalysts for lipid oxidation[8]. Therefore, ethylenediaminetetraacetic acid (EDTA) is often added to mayonnaise to bind free metal ions via chelation, thus reducing the formation of lipid peroxidation (LPO) products[9,10]. In food emulsions, protein emulsifiers are known to react with free radicals formed via lipid oxidation, thus acting as antioxidants via scavenging free radicals[11–13]. Emulsions stabilized by whey proteins, for example, showed better oxidation stability than emulsions stabilized by the surfactant Tween[14]. It has therefore been argued that due to their proximity to lipid radicals generated at the droplet interface, proteins adsorbed at the oil-water interface can function as effective antioxidants. Even though the importance of proteins present at the interface on lipid oxidation has been highlighted earlier[15], only a few quantitative studies have been reported[16,17] since and, to our knowledge, no studies have yet addressed the challenge of localizing lipid and protein oxidation in a complex food emulsion.

In mayonnaise, proteins that originate from LDL particles are either present at the oil-water droplet interface, as individual particles in the continuous phase, or aggregated in granules[1]. Apoproteins from LDL particles can specifically act as emulsifiers at droplet interfaces within mayonnaise. In both intact LDLs and in the dispersed form at droplet interfaces, apoproteins can

engage in oxidation reactions. The potential role of these particles in protein and lipid oxidation processes occurring in mayonnaise has been largely overlooked. Human plasma model systems have been used to study oxidation and aggregation of LDLs using bright field microscopy and transmission electron microscopy (TEM)[18]. By means of UV/VIS and fluorescence spectroscopy, protein oxidation of LDL was investigated, showing that the fluorescence intensity increased in the 430 nm emission range after auto-oxidation[19,20]. We hypothesize that the proteins from LDL particles can scavenge lipid radicals, not only in intact particles but also in the dispersed form at the droplet interfaces.

Location and time-dependent detection of lipid and protein radicals is required for unraveling possible oxidation pathways in mayonnaise. Conventionally, electron spin resonance (ESR) is used to detect free radicals and radical adducts of either proteins or lipids. ESR can be applied to either the oil or water phase, however, the signals from immobile protein radical adducts are broad and overlap. Furthermore, ESR does not allow for localizing radicals. In food emulsions, lipid radicals are formed at the oil-water droplet interface and can either diffuse quickly into the droplet or be transferred to other oil droplets[21]. In this study, we suggest localizing protein radicals as a proxy for lipid oxidation. In ESR, 5,5-Dimethyl-1-pyrroline N-oxide (DMPO) is frequently used to detect protein free radicals by forming stable spin adducts. Similar to biomedical approaches allowing to localization of free radicals via fluorescent spin trapping adducts[22], we developed a spin trap composed of the fluorophore AFDye 647 and CAMPO, a derivative of water-soluble DMPO.

Here, we study the interplay of protein and lipid oxidation in mayonnaise. We first monitor structural aspects such as the aggregation of LDL particles. We then localize protein free radicals at the oil-water droplet interface and in the continuous phase using a fluorescently labeled free radical spin trap. Cryo-transmission electron microscopy (cryo-TEM) was used to observe LDL particles at the nanometer scale, and we used plunge vitrification of LDLs present in the continuous phase isolated from mayonnaise to study oxidation in a time-resolved manner. Our imaging experiments were performed at time points based on a previous kinetic assessment of primary and secondary lipid oxidation products[23]. We further studied the impact of oxidation using optical bright-field light microscopy, which provides micro-scale information allowing us to identify aggregation of LDLs upon oxidation. Moreover, our newly developed fluorescently labeled spin trap (CAMPO-AFDye 647) was applied to detect protein oxidation at an early stage. We monitored oxidation in dilute (26% (w/w) oil concentration) mayonnaises and demonstrated the co-localization of autofluorescence from oxidized proteins and CAMPO-AFDye 647 fluorescence from protein free radical spin adducts.

4.2 Materials and Method

4.2.1 Materials

2-((1E,3E)-5-((E)-3,3-dimethyl-5-sulfo-1-(3-sulfopropyl) indolin-2- ylidene) penta-1,3-dien-1-yl) - 3-methyl-1-(6-((4-(2-methyl-1-oxido- 3,4-dihydro-2H-pyrrole-2-carboxamido) butyl) amino)-6-oxohexyl) - 3- (4-sulfobutyl)-3H-indol-1-ium-5-sulfonate (CAMPO-AFDye 647) was synthesized by SyMO-Chem B.V. (Eindhoven, the Netherlands). Reference AuNPs were obtained from AURION (Wageningen, the Netherlands). Sodium chloride (>99.5%, EMSURE®) and Rhodamine B were purchased from Sigma–Aldrich. Spirit white vinegar (4%), soybean oil and egg yolk containing 8% NaCl were purchased from a local store. Alumina powder (Alumina N-Super I) was obtained from MP EcoChrom™. EDTA (Ethylenediaminetetraacetic acid disodium salt dihydrate) was purchased from Merck. Demineralized (demi) water was used for all experiments.

4.2.2 Preparation of oil samples

Stripped soybean oil was prepared using alumina powder to remove lipid-soluble antioxidants[15]. The oil was mixed with the powder at a volume ratio of 2:1 in Falcon tubes and shaken for 24 hrs. The suspension was then centrifuged at $2000 \times g$ for 20 min. The oil was collected, and the same centrifugation procedure was repeated to ensure the complete removal of the alumina powder. Stripped soybean oil was used for the co-localization experiments of CAMPO-AFDye 647 and autofluorescence in dilute emulsions. Unless mentioned otherwise, non-stripped soybean oil was used.

Mayonnaise was prepared from 78% (w/w) of soybean oil, 5% (w/w) of egg yolk with 8% NaCl, 0.7% (w/w) of salt, 14.8% (w/w) of demi water, and 1.5% (w/w) of spirit vinegar using a Silverson mixer. Egg yolk, salt and demi water were premixed in a 500 mL jar and mixed at 2000 rpm for 20 s. Oil was slowly added and mixed at 8500 rpm for 4 min. Spirit vinegar was added and mixed further for 2 min. For preparing a dilute mayonnaise, we added demi-water to reach a final 26% (w/w) oil concentration. Under standard conditions, the dilute mayonnaise had pH 4.0. Without the addition of vinegar, the pH was 6.6. For samples formulated with EDTA, this ingredient was added to the water phase before making the emulsions. The continuous phase of the prepared mayonnaise was obtained by centrifuging the fresh mayonnaise at $4000 \times g$ for 1 hr. The continuous phase was collected from the bottom part of the Eppendorf tubes by cutting off the bottom tip. The continuous phase was stored in a fridge at 4 ℃ until further use. To accelerate the oxidation, these separated continuous phases (each 100 μL in 1.5 mL Eppendorf tubes) were stored at 40 ℃ and sampled at 0, 1, 3, and 5 days.

For oxidation experiments including spin traps, CAMPO-AFDye 647 (MW = 1068.30 g/mol) was dissolved with dimethylsulfoxide (DMSO) to prepare 0.01 g/L of CAMPO-AFDye 647 stock solutions. The stock solution was added to the continuous phase samples and mayonnaise to reach a final concentration of 1 µM. The CAMPO-AFDye 647 spin trap was added in two different ways. In the pre-addition method, CAMPO-AFDye 647 was added in the continuous phase/mayonnaise *before* oxidation. In the post-addition method, CAMPO-AFDye 647 was added in the continuous phase/mayonnaise *after* oxidation. For the post-addition method, samples were imaged at room temperature (21 ºC) within one hour after incubation. For the samples used for imaging of protein localization, 1 µL of Rhodamine B stock solution (10 µM) was added to 9 µL of emulsion to stain proteins before measurements.

4.2.3   Light microscopy

All optical imaging was performed on a home-built microscope, the miCube[24], at room temperature (21 ºC). For brightfield imaging, we used a LED lamp in transmission mode. For the measurements of CAMPO-AFDye 647 and autofluorescence from oxidized proteins, we used a rescan confocal microscopy (RCM) module (Confocal.nl, Amsterdam, The Netherlands)[25] connected to the miCube. Four different lasers were available (405 nm, 488 nm, 561 nm, 642 nm, Omicron LightHub). The microscope is further equipped with a 100× oil immersion objective lens (Nikon TIRF 1.49NA HP SR) and an Andor – Zyla 4.2 PLUS sCMOS camera. The frame time was set to 50 ms. We used 2 × 2 pixel binning for a final image size of 1024 by 1024 pixels and an effective field of view of 88 × 88 µm. Images were recorded using MicroManager 2.0[26]. To detect protein autofluorescence, samples were excited at 405 nm (12 mW). For the detection of trapped free radical adducts with CAMPO-AFDye 647, the samples were illuminated at 642 nm (34 mW). Fluorescence from Rhodamine B was measured with excitation at 561 nm (8 mW). For each measurement, 3 µL of the continuous phase sample was added to a well of silicon gasket (CultureWell™, GRACEBIO-LABS) on a cleaned cover glass.

4.2.4   Quantification of fluorescence imaging data

For further quantifying both changes in the intensity levels of the autofluorescence and the accumulation of CAMPO-AFDye 647, we used ImageJ and MATLAB R2021b (**Figure S4.1**). First, we apply a Gaussian Blur filter to the raw data (Gaussian filter, with sigma radius set to 1 pixel). These filtered images were used for obtaining the segmented masks by adjusting the threshold and converting these images to a mask. Background filtered images were obtained by multiplying the segmented mask images consisting of zeros and ones with the raw image data using MATLAB. The intensity histograms of autofluorescence and the histograms of CAMPO-AFDye 647 aggregates' sizes were plotted using MATLAB R2021b.

4.2.5   Sample preparation for cryo-TEM

Samples for cryo-TEM were prepared by applying 3 µL of the continuous phase separated from mayonnaise on a 200 mesh Cu grid with a R2/2 Quantifoil® carbon support film (Quantifoil MicroTools GmbH). An automated vitrification robot (Thermo Fisher Scientific Vitrobot™ Mark IV) was used to first blot and then plunge the samples into liquid ethane. Prior to the application of the sample, the TEM grid was glow-discharged to render the surface of the carbon TEM support film hydrophilic. Cryo-TEM imaging was conducted on the TU/e CryoTitan (Thermo Fisher Scientific), which was operated at 300 kV and is equipped with a Field-Emission Gun, a post-GIF 2k× 2k Gatan CCD camera, and a post column Gatan Energy Filter (GIF). Cryo-TEM images were acquired at an electron dose rate of 3 and 6 e^- $Å^{-2}$ s^{-1} with an exposure time of 1 s at magnifications of 6500× and 24000× , respectively. The nominal defocus was set to - 20 µm for 6500× and - 5 µm for 24000×. For detailed imaging conditions for cryo-electron tomography, see **Figure S4.2**.

4.3   Results

4.3.1   Impact of oxidation on multi-scale structure in the continuous phase

We first characterized the aggregation of LDL particles in the isolated continuous phase of mayonnaise using bright-field light microscopy over a duration of 5 days. In the fresh sample, no LDL superstructures were visible, suggesting little to no aggregation of LDLs. In their non-aggregated form, LDLs are too small to be visible using diffraction limited bright-field imaging (**Figure 4.1a**). After 1 day, micrometer sized LDL superstructures become visible, which then grow to fractals (3 days) and fractal aggregates (5 days). This aggregation behavior upon oxidation is similar to the one observed for LDLs superstructures from human plasma[18].

Using cryo-TEM, we determined the diameter of dispersed LDLs to be 36 ± 6 nm in the fresh sample (**Figure 4.1b,c, d-I**). The number (N) of particles analyzed was $N = 112$ (**Figure S4.3**). In addition, we saw aggregated LDLs (**Figure 4.1d-II**), liposomes characterized by a double phospholipid layer without proteins (**Figure 4.1d-III**), and spherical, low contrast objects of about 200 nm in diameter (**Fig. 4.1d-IV**), which we tentatively assigned to very low-density lipoprotein (VLDL) particles[27].

After one day, we observed aggregates with a broad size distribution composed of mainly LDLs and liposomes. The average diameter of the longest axis was roughly 400 nm with a standard deviation of 200 nm ($N = 69$). The structure of these aggregates can be further resolved in cross sections from the acquired electron tomograms (**Figure S4.2**). After three days, we observed aggregates spanning the entire 2 µm wide hole of the carbon film. Our cryo-TEM and cryo-ET data confirm that the superstructures seen in bright-field light microscopy consist of LDLs.
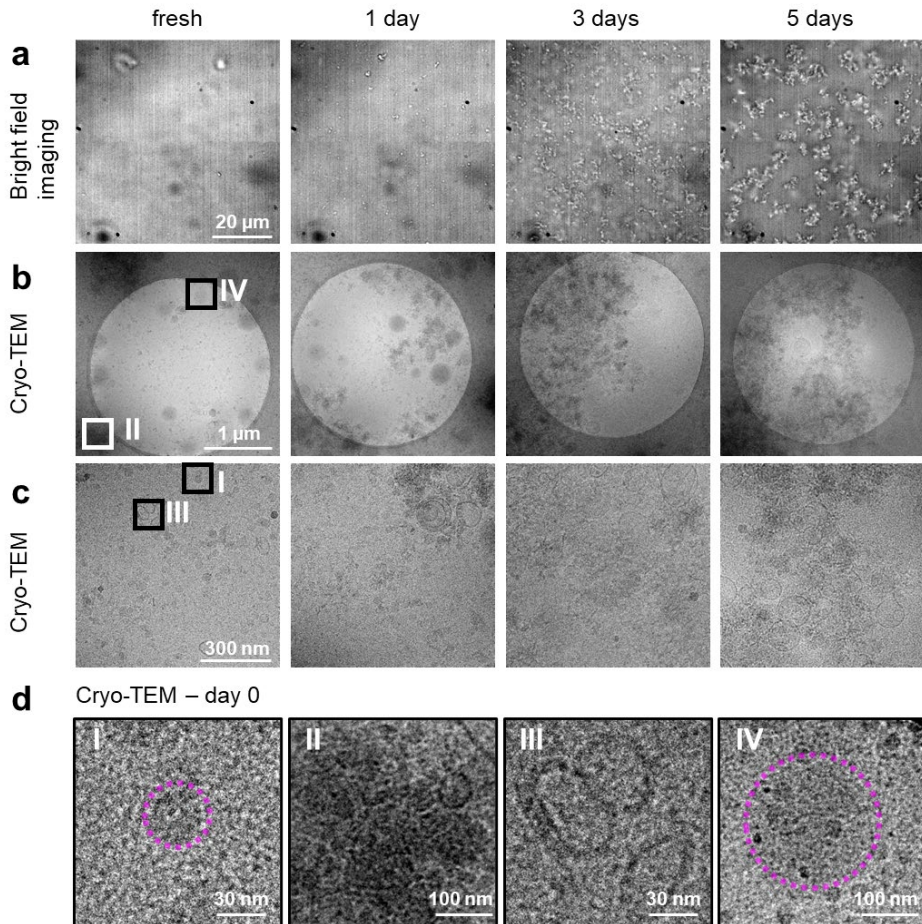
Figure 4.1. Multi-scale imaging of LDL particle aggregation in the continuous phase of mayonnaise. (**a**) Bright-field images after incubation for 0, 1, 3, and 5 days at 40 °C. Black blurry spots located in the same place of different images indicate dust on the camera, not from the sample itself. Cryo-TEM images of the continuous phase at magnifications of 6500× (**b**) and 24000× (**c**) during the same sample incubation period. (**d**) Zoom-in regions from (**b**) and (**c**) for fresh samples showing I: LDL, II: aggregated LDLs, III: liposome vesicles, IV: spherical low-contrast object, VLDLs. A nominal defocus of - 20 μm and - 5 μm was applied for magnifications of 6500× and 24000×, respectively. Contrast and brightness were adjusted for visibility. Some images (d-I and d-IV) contain dashed outlines (magenta) of the underlying structures for visual guidance.

4.3.2   Co-localization of protein oxidation and radical formation in the continuous phase

LDLs show autofluorescence in the ultraviolet (UV) region mainly due to tryptophan (Trp) residues present in apolipoproteins. Upon oxidation of LDLs, fluorescence emission increases in the visible region due to reactions between lipid peroxidation products such as aldehyde with amino groups[20]. In **Chapter 2**, we compared the autofluorescence spectrum after excitation at 300 nm, 360 nm, and 405 nm to confirm the decrease of FL in the UV region and the increase

72

in longer wavelength. The measurement shows an inverse correlation between the decrease of tryptophane autofluorescence (excitation at 300 nm) and the increase of the autofluorescence signal of aldehyde-apolipoprotein adducts (excitation at 405 nm). In **Chapter 3**, we also assessed protein oxidation in mayonnaise via autofluorescence in the longer wavelength, using 488 nm excitation and detection in the 500 – 560 nm range. Here, we excited at 405 nm to maximize the detectable fluorescence emission intensity (**Figure S4.4**). LDL superstructures in the continuous phase showed aggregation over time leading to small fractals upon oxidation with autofluorescence (**Figure S4.5**).

To further localize protein oxidation, we deployed adducts of CAMPO, a derivative of the spin trap DMPO. CAMPO was labeled with AFDye 647 for fluorescence imaging (**Figure 4.2a**). We first monitored the accumulation of CAMPO-AFDye 647 fluorescence in the continuous phase of mayonnaise over time. To show the co-localization between spin trap and oxidized proteins, we combined fluorescence images from CAMPO-AFDye 647 accumulation (red channel) and autofluorescence (blue channel). Two different ways of adding CAMPO-AFDye 647 to the continuous phase were used to see the effect of CAMPO accumulation during incubation: pre-addition and post-addition.

With the fresh and 1 day oxidation sample of the pre-addition series, we did not observe any increase of intensities caused by either protein autofluorescence or CAMPO-AFDye 647 fluorescence (**Figure 4.2b**). The high intensities in the red channel indicate that CAMPO-AFDye 647 is freely diffusing in the continuous phase instead of reacting with protein free radicals. In the pre-addition series (**Figure 4.2c**), we observed that LDL superstructures and aggregates form over time similar to the bright field images seen in **Figure 4.1a**. Further, the autofluorescence (blue) increases and CAMPO-AFDye 647 (red) accumulates in the LDL aggregates. The decrease of the background in the continuous phase is in line with CAMPO-AFDye 647 accumulating at sites with protein radicals. After five days, CAMPO-AFDye 647 accumulation in fractal aggregates of LDL superstructures was observed and found to be mostly co-localized with autofluorescence from oxidized proteins.
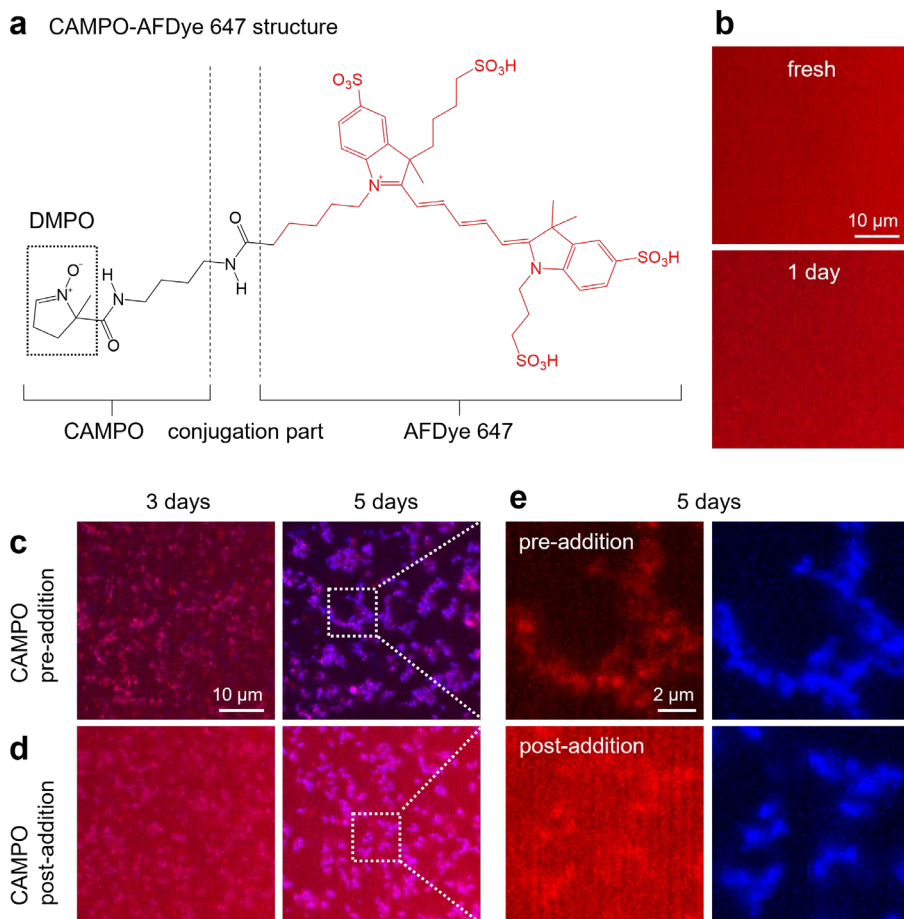
Figure 4.2. Chemical structure of CAMPO-AFDye 647 and fluorescence images of the continuous phases of mayonnaise. (**a**) Chemical structure of CAMPO-AFDye 647. CAMPO is derived from DMPO (left) and conjugated to AFDye 647 (right). (b-d) Fluorescence images showing the red (CAMPO-AFDye 647) and the blue (autofluorescence) channels were recorded after up to 5 days of incubation. (**b**) CAMPO-AFDye 647 was directly added after preparing the emulsions and measured within 1 hr of preparation (fresh). We neither observed localized oxidation after 1 h (fresh) nor after one day. (**c-d**) CAMPO-AFDye 647 was pre-added before oxidation (c) and post-added after continuing oxidation (d). Aggregates of LDLs show the co-localization of CAMPO-AFDye 647 (red) and autofluorescence (blue) after 5 days. (**e**) Spectrally resolved zoom-in (white dashed boxes in c and d) after 5 days of oxidation.

In the post-addition series (**Figure 4.2d**), we could measure increased autofluorescence (blue) but noticed elevated background intensities originating from freely diffusing CAMPO-AFDye 647. Over the five days, aggregates in the continuous phase from both addition methods showed a similar extent of aggregation. **Figure 4.2e** compares spectrally resolved channels for samples oxidized for five days. Fluorescence of accumulated CAMPO-AFDye 647 and protein autofluorescence are clearly co-localized in the pre-addition sample, whereas the signal to noise

ratio of CAMPO-AFDye 647 is compromised in the post-addition sample due to the fluorophore still being present in free solution. We note that autofluorescence signals from two different addition methods (pre- and post-addition) showed a similar distribution of intensity levels, indicating they are not influenced by the addition of CAMPO-AFDye 647 (**Figure S4.6**).

4.3.3 Co-localization of protein oxidation and radical formation in dilute mayonnaise

The dense packing of oil droplets made it difficult to discern LDLs in the continuous phase and at the interfaces of oil droplets. The samples were therefore diluted before observing protein autofluorescence and CAMPO-AFDye 647 accumulation. As a control, dilute (26% (w/w) oil concentration) mayonnaise without CAMPO-AFDye 647 was measured (**Figure 4.3a**). As seen, the level of autofluorescence at the oil-water droplet interface and in the continuous phase increased upon oxidation from day 0 (fresh) to day 5 (**Figure S4.7**). To show the co-localization of accumulated spin trap and oxidized proteins, we combined the images of the red channel (CAMPO-AFDye 647) and the blue channel (autofluorescence). Already in the fresh sample, we observed the accumulation of CAMPO-AFDye 647 fluorescence at the oil-water droplet interface and in the continuous phase between droplets (**Figure 4.3b**). After 5 days, we saw an increase in protein oxidation around and especially between droplets, likely representing LDL aggregates (**Figure 4.3b**). It should be noted that although in most cases, co-localization of CAMPO-AFDye 647 and autofluorescence was observed, few regions showed only CAMPO-AFDye 647 accumulation. In **Figure 4.3c & d**, selected regions of interest and spectrally separated images are shown. In the fresh sample, only CAMPO-AFDye 647 accumulated heterogeneously at the oil-water droplet interface, whereas after 5 days, the autofluorescence signal around the droplets partially co-localize with CAMPO-AFDye 647 (**Figure 4.3c & d**). The accumulation of CAMPO-AFDye 647 at the droplet interface occurs in micron-scale domains as well as a thin homogeneous halo around the droplet interface (**Figure 4.3d**). These findings suggest that the accumulation of CAMPO-AFDye 647 spin trap occurs in both micron-scale LDL granules and protein molecules stabilizing the droplet interfaces as emulsifiers. Both apoproteins originating from LDL particles and phosvitin qualify for such a role.
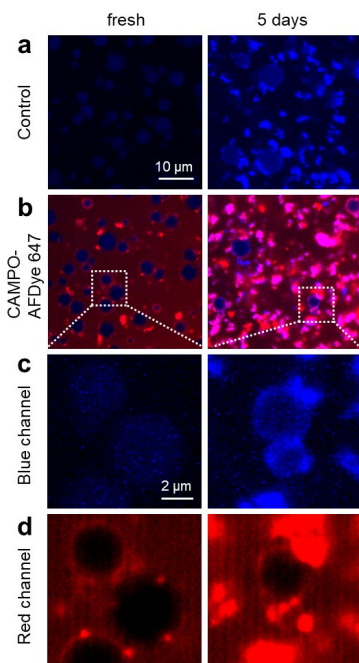
Figure 4.3. Localization of CAMPO-AFDye 647 and autofluorescence in dilute mayonnaise. Images combined from red (CAMPO-AFDye 647) and blue (autofluorescence) emission channels are shown in (a)-(b). (**a**) Dilute emulsions without any fluorescent dyes were measured on day 0 (fresh) and day 5 after incubation. These control samples only showed autofluorescence after incubation. (**b**) Samples with the post-addition of 1 μM CAMPO-AFDye 647. CAMPO-AFDye 647 was added just before each measurement. Co-localization between CAMPO-AFDye 647 and autofluorescence was seen after five days of incubation. (**c**) Zoom-in (white dashed box) blue channel images from (b). Significantly increased autofluorescence was observed only in the sample after 5 days of oxidation. (**d**) Zoom-in (white dashed box) red channel images from (b). Accumulation of CAMPO-AFDye 647 at the interface was seen after five days of oxidation, whereas small granules of CAMPO-AFDye 647 were already observed in the fresh sample. Scales of fluorescence intensities are adjusted in the same range for each channel to see the increased CAMPO-AFDye 647 accumulation and autofluorescence.

To validate that the accumulation of CAMPO-AFDye 647 at droplet interfaces is due to protein free radical formation induced by nearby lipid radicals, the pH of the mayonnaise was varied. Under the usual acidic environment of mayonnaise, phosvitin has a weak affinity for ferric ions, which allows them to act as catalysts for lipid oxidation at oil-water droplet interfaces[8]. At neutral pH, phosvitin has a stronger binding affinity for ferric ions thus preventing ferric ions from being released at the interface[28]. Indeed, whereas accumulation of CAMPO-AFDye 647 at droplet interfaces at pH 4.0 was seen (**Figure 4.4a**), we did not observe this at pH 6.6 (**Figure 4.4b**).
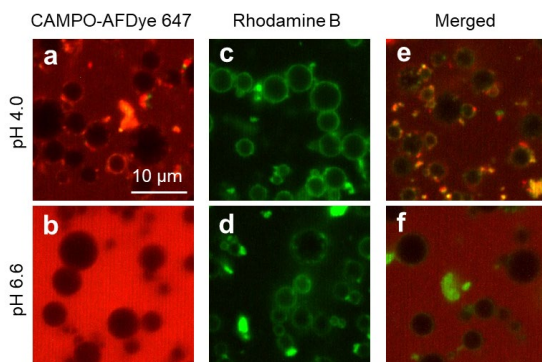
Figure 4.4. pH dependency of CAMPO-AFDye 647 accumulation with stained proteins in dilute mayonnaise. 1 μM of CAMPO-AFDye 647 and Rhodamine B was added before measurements in samples stored at 4 °C. (**a**, **b**) Accumulation of CAMPO-AFDye 647 with excitation at 640 nm. (**c**, **d**) Protein staining with Rhodamine B at the oil-water droplet interface and in the continuous phase. Samples were illuminated at 561 nm. (**e**, **f**) Overlay images of CAMPO-AFDye 647 and Rhodamine B. Co-localizations are observed in dilute mayonnaise only at pH 4.0.

Furthermore, Rhodamine B staining confirmed that proteins are present at the droplet interfaces both at pH 4.0 and 6.6 (**Figure 4.4c & d**). This observation ruled out potential effects due to pH induced release of proteins from the droplet interface. Co-localization of Rhodamine B and CAMPO-AFDye 647 could only be observed in acidic mayonnaise (**Figure 4.4e & f**).

The accumulation of CAMPO-AFDye 647 in the fresh sample (**Figure 4.3b**) indicated that protein radicals were already formed soon (1 hr) after preparing the dilute mayonnaise. In order to exclude that this effect is induced by a specific binding of CAMPO-AFDye 647, we prepared dilute mayonnaise with and without EDTA, which acts as a strong antioxidant by chelating metal ions from phosvitin at the droplet interface[2,8]. Upon the addition of EDTA, less CAMPO-AFDye 647 accumulated at the droplet interfaces over time compared to conditions in the absence of EDTA (**Figure 4.5a & b**). To compare the changes, we analyzed the sizes of the aggregates (**Figure S4.8**). The dilute mayonnaise without EDTA (**Figure 4.5a**) showed an increase in the size of LDL aggregates over time, while the emulsion containing EDTA (**Figure 4.5b**) showed hardly any changes. A zoom into the images after ten days of oxidation showed that in the absence of EDTA most droplet interfaces feature trapped CAMPO-AFDye 647 as they show halos at the interface (**Figure 4.5c**). In the presence of EDTA, accumulation at interfaces is virtually absent. Accumulation in aggregates is still visible in LDL aggregates but less pronounced than in the absence of EDTA. This observation confirmed that the addition of EDTA significantly delayed lipid radical formation and subsequent protein oxidation at the interface but was less effective in inhibiting the oxidation of LDLs in the continuous phase.
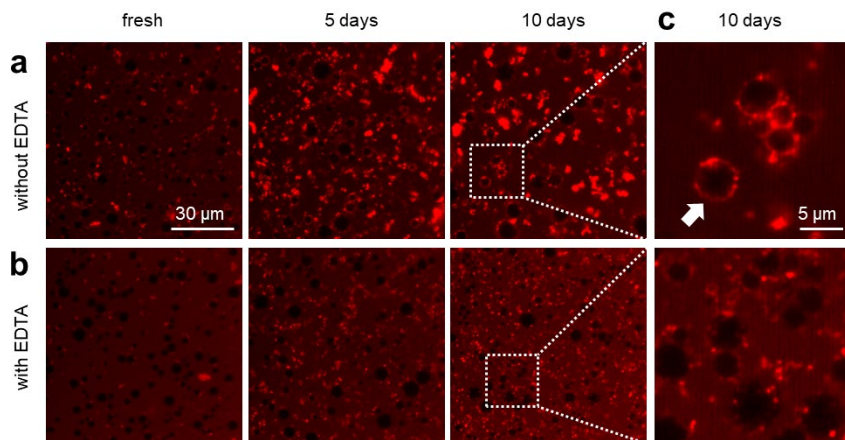
Figure 4.5. EDTA dependency of CAMPO-AFDye 647 accumulation in dilute mayonnaise at pH 4.0. The CAMPO-AFDye 647 spin trap was added at the indicated time points (post-addition). Images were measured using RCM. (**a**, **b**) Dilute mayonnaise without (a) and with 100 mM EDTA (b) measured after 0 (fresh), 5 and 10 days of incubation. (**c**) Zoom-in (white dashed box) images from (a, b) after 10 days of oxidation. The arrow points the halos at the oil-water droplet interface from CAMPO-AFDye 647 accumulation.

4.4 Discussion

Our multi-scale microscopy measurements suggest a pathway for protein oxidation, including LDLs in the continuous phase of mayonnaise which is independent from lipid oxidation in oil droplets. The protein oxidation and aggregation of LDLs is likely triggered by free radical-mediated oxidation of unsaturated fatty acids[19,29,30], which then can trigger radical chain reactions. Increased autofluorescence intensity supports this finding (**Figure S4.5**), as it was previously shown that increased autofluorescence from oxidized LDL is due to the reaction between lipid peroxidation products such as aldehyde with amino groups[20]. An increase in autofluorescence alone is, however, not a suitable marker for the early stage of oxidation, as aldehydes are secondary breakdown products of unsaturated lipids. Therefore, we here decided to use a water-soluble fluorescent spin trap (CAMPO-AFDye 647) that targets protein radicals. We assume that due to the immobility of proteins at the oil-water droplet interfaces or in LDL particles, the trapped radicals accumulate locally. This mechanism is unlikely to work for spin trapped lipid radicals which are smaller and more likely to diffuse throughout oil droplets. We are aware that CAMPO may lead to false-positive signals originating from the reaction with substrates other than our targeted protein free radicals[31]. Our results confirm, however, that spin trapping of protein radicals using CAMPO can be used as a proxy for local and early free radical formation at oil-water droplet interfaces since CAMPO predominantly co-localized with the autofluorescence originating from protein oxidation (**Figure 4.3**).

The data did not show accumulation of CAMPO-AFDye 647 in the fresh continuous phase (**Figure 4.2b**), whereas the fresh emulsions did show (**Figure 4.3b**). This finding implies that protein oxidation at the oil-water droplet interfaces is faster than in the continuous phase. This effect is due to the generation of lipid radicals at the droplet interfaces induced by reactions between iron and lipid hydroperoxide, which are already initially present in the oil phase. Lipid hydroperoxides are more polar and surface active than unsaturated fatty acids, therefore, they can concentrate at the droplet interfaces[32]. This corroborates what was reported recently on protein-lipid co-oxidation in whey protein isolate-stabilized emulsions[33]. The authors found that the proteins adsorbed at the oil-water interface showed higher levels of oxidation than non-adsorbed proteins possibly due to their free radical scavenging activity at the interface.

Figure 4.6 summarizes our findings in a schematic manner. We discern two spatially separate mechanisms by which protein radicals can be formed by lipid radicals. At the oil-water droplet interfaces, lipid oxidation is catalyzed by iron ions associated with surface bound phosvitin[34,35]. The catalytic activity of iron close to the interface is increased at low pH of mayonnaise, as the binding strength of iron ions to phosvitin is decreased[6,36,37] (**Figure 4.6a**). Iron ions can also be outcompeted from phosvitin by chelation with EDTA[36]. In a spatially separate mechanism, lipid

oxidation in LDL particles produces lipid radicals that induce protein free radical formation and protein oxidation (**Figure 4.6b**). This mechanism is still active in the presence of EDTA, suggesting that chelated iron can still act as a catalyst, albeit less strongly than in its free form. Upon oxidation, LDL particles are prone to aggregation[18,29] (**Figure 4.6c**), which can play a role in the physical instability of mayonnaise in prolonged stages of oxidation. To this end, it remains unclear why most but not all areas show co-localization of CAMPO accumulation with autofluorescence. One explanation is the trapping of CAMPO-AFDye 647 by phosvitin, which contains fewer tryptophan residues than apoproteins[38,39]. To explore this further, we suggest employing a higher resolution imaging method[40] in combination with the localization of phosvitin using a phosvitin-antibody conjugated with fluorophores[41].
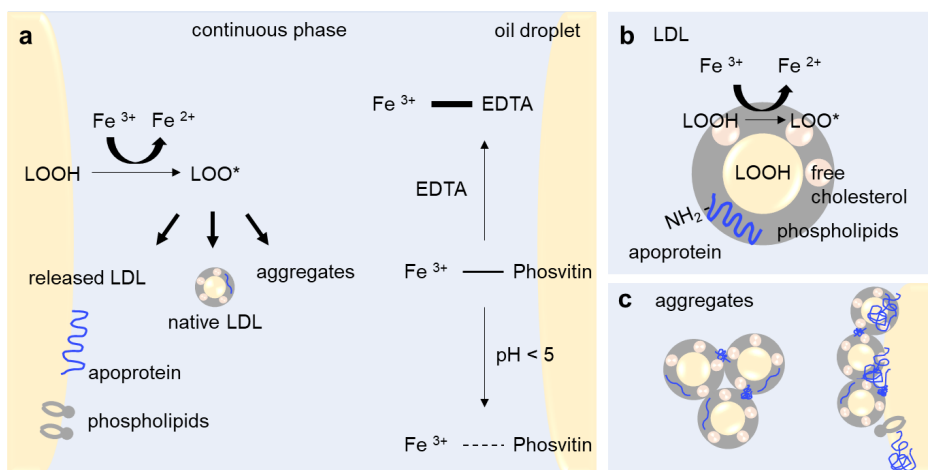

Figure 4.6. Schematic of lipid and protein oxidation with the formation of free radicals at the oil-water droplet interface and in the continuous phase. Apoproteins and phospholipids released from LDLs are adsorbed at the interface. Native and oxidized LDLs are present in the continuous phase. (**a**) Depiction of underlying lipid oxidation mechanisms, including oxidation of proteins dispersed at oil-water interface or present in LDLs in different conditions (acidic/neutral condition and presence of EDTA). Addition of EDTA delays lipid oxidation because of stronger binding with Fe^{3+} than phosvitin. In acidic conditions, Fe^{3+} promotes lipid oxidation due to weak binding between Fe^{3+} and phosvitin. Thick and dashed lines, respectively, indicate strong and weaker binding of iron with EDTA and phosvitin. (**b**) Apoproteins in LDL can be oxidized from lipid free radicals generated within the particles and from oil droplets at the interface. (**c**) Oxidized LDL can cause protein changes such as misfolding and/or cross-linking and aggregation of LDLs at the interface and in the continuous phase.

4.5   Conclusions

We demonstrated that the accumulation of a fluorescently labeled spin trap (CAMPO-AFDye 647) can be used to localize protein radical formation at droplet interfaces and in the continuous phase of mayonnaise. The local formation of protein radicals can be detected ahead of an increase in autofluorescence thereby providing a proxy for the local formation of lipid radicals. In mayonnaise, protein free radicals can be generated via two routes. At the droplet interface, oxidation of proteins including LDLs, apoproteins, and phosvitin is induced by lipid radicals formed close to the droplet interfaces. This route is not effective in a high pH environment, at which iron is strongly bound to phosvitin. The second route is active in the continuous phase, where lipids in LDL particles are also prone to generate radicals, inducing protein oxidation and LDL aggregation. Upon addition of EDTA, protein radical formation is more effectively inhibited at the droplet interface than in the continuous phase. We believe that the fluorescently labeled spin trap (CAMPO-AFDye 647) presents a powerful tool for studying the early onset of lipid-protein co-oxidation at oil-water droplet interfaces and in lipoprotein particles.

References

1. Anton, M. Egg yolk: structures, functionalities and processes. *J Sci Food Agric* **93**, 2871–2880 (2013).
2. Jacobsen, C., Timm, M. & Meyer, A. Oxidation in fish oil enriched mayonnaise: Ascorbic acid and low pH increase oxidative deterioration. *J Agric Food Chem* **49**, 3947–3956 (2001).
3. Anton, M. *et al.* Chemical and structural characterisation of low-density lipoproteins purified from hen egg yolk. *Food Chem* **83**, 175–183 (2003).
4. Sirvente, H. *et al.* Structuring and functionalization of dispersions containing egg yolk, plasma and granules induced by mechanical treatments. *J Agric Food Chem* **55**, 9537–9544 (2007).
5. Schaich, K. M. Thinking outside the classical chain reaction box of lipid oxidation. *Lipid Technol* **24**, 55–58 (2012).
6. Jacobsen, C., Adler-Nissen, J. & Meyer, A. S. Effect of ascorbic acid on iron release from the emulsifier interface and on the oxidative flavor deterioration in fish oil enriched mayonnaise. *J Agric Food Chem* **47**, 4917–4926 (1999).
7. Thomson, M. K., Jacobsen, C. & Skibsted, L. H. Mechanism of initiation of oxidation in mayonnaise enriched with fish oil as studied by electron spin resonance spectroscopy. *European Food Research and Technology* **211**, 381–386 (2000).
8. Merkx, D. W. H., Delić, F., Wierenga, P. A., Hennebelle, M. & van Duynhoven, J. P. M. 31P NMR assessment of the phosvitin-iron complex in mayonnaise. *Magnetic Resonance in Chemistry* **57**, 540–547 (2019).
9. Lee, J. & Decker, E. A. Effects of metal chelator, sodium azide, and superoxide dismutase on the oxidative stability in riboflavin-photosensitized oil-in-water emulsion systems. *J Agric Food Chem* **59**, 6271–6276 (2011).
10. Nielsen, N. S., Petersen, A., Meyer, A. S., Timm-Heinrich, M. & Jacobsen, C. Effects of lactoferrin, phytic acid, and EDTA on oxidation in two food emulsions enriched with long-chain polyunsaturated fatty acids. *J Agric Food Chem* **52**, 7690–7699 (2004).
11. Schaich, K. M. Co-oxidation of proteins by oxidizing lipids. *Lipid Oxidation Pathways* **2**, 181–272 (2008).
12. Berton, C., Ropers, M. H., Guibert, D., Solé, V. & Genot, C. Modifications of interfacial proteins in oil-in-water emulsions prior to and during lipid oxidation. *J Agric Food Chem* **60**, 8659–8671 (2012).
13. Hematyar, N., Rustad, T., Sampels, S. & Kastrup Dalsgaard, T. Relationship between lipid and protein oxidation in fish. *Aquac Res* **50**, 1393–1403 (2019).
14. Zhu, Z. *et al.* Impact of Interfacial Composition on Lipid and Protein Co-Oxidation in Oil-in-Water Emulsions Containing Mixed Emulsifers. *J Agric Food Chem* **66**, 4458–4468 (2018).
15. Berton, C., Genot, C. & Ropers, M. H. Quantification of unadsorbed protein and surfactant emulsifiers in oil-in-water emulsions. *J Colloid Interface Sci* **354**, 739–748 (2011).
16. Berton, C., Genot, C., Guibert, D. & Ropers, M. H. Effect of lateral heterogeneity in mixed surfactant-stabilized interfaces on the oxidation of unsaturated lipids in oil-in-water emulsions. *J Colloid Interface Sci* **377**, 244–250 (2012).
17. Berton-Carabin, C. C., Schröder, A., Rovalino-Cordova, A., Schroën, K. & Sagis, L. Protein and lipid oxidation affect the viscoelasticity of whey protein layers at the oil–water interface. *European Journal of Lipid Science and Technology* **118**, 1630–1643 (2016).
18. Xu, S. & Lin, B. The mechanism of oxidation-induced low-density lipoprotein aggregation: An analogy to colloidal aggregation and beyond? *Biophys J* **81**, 2403–2413 (2001).
19. Pinchuk, I. & Lichtenberg, D. Analysis of the kinetics of lipid peroxidation in terms of characteristic time-points. *Chem Phys Lipids* **178**, 63–76 (2014).
20. Koller, E., Quehenberger, O., Jürgens, G., Wolfbeis, O. S. & Esterbauer, H. Investigation of human plasma low density lipoprotein by three-dimensional flourescence spectroscopy. *FEBS Lett* **198**, 229–234 (1986).
21. Laguerre, M., Bily, A., Roller, M. & Birtić, S. Mass Transport Phenomena in Lipid Oxidation and Antioxidation. *Annual Review of Food Science and Technology* vol. 8 391–411 (2017).
22. Mason, R. P. & Ganini, D. Immuno-spin trapping of macromolecules free radicals in vitro and in vivo – One stop shopping for free radical detection. *Free Radic Biol Med* **131**, 318–331 (2019).
23. Boerkamp, V. J. P. *et al.* Quantitative assessment of epoxide formation in oil and mayonnaise by 1H-13C HSQC NMR spectroscopy. *Food Chem* **390**, 133145 (2022).
24. Martens, K. J. A. *et al.* Visualisation of dCas9 target search in vivo using an open-microscopy framework. *Nat Commun* **10**, 1–11 (2019).
25. De Luca, G. M. *et al.* Re-scan confocal microscopy: scanning twice for better resolution. *Biomedical Optics Express, Vol. 4, Issue 11, pp. 2644-2656* **4**, 2644–2656 (2013).
26. Edelstein, A. D. *et al.* Advanced methods of microscope control using μManager software. *J Biol Methods* **1**, e10 (2014).
27. Huopalahti, R. *et al.* Bioactive egg compounds. *Bioactive Egg Compounds* 1–298 (2007)

28.   Castellani, O., Guérin-Dubiard, C., David-Briand, E. & Anton, M. Influence of physicochemical conditions and technological treatments on the iron binding capacity of egg yolk phosvitin. *Food Chem* **85**, 569–577 (2004).

29.   Witztum, J. L. & Steinberg, D. Role of oxidized low density lipoprotein in atherogenesis. *Journal of Clinical Investigation* **88**, 1785–1792 (1991).

30.   Stocker, R. & Keaney, J. F. Role of oxidative modifications in atherosclerosis. *Physiol Rev* **84**, 1381–1478 (2004).

31.   Leinisch, F., Jiang, J., Derose, E. F., Khramtsov, V. V. & Mason, R. P. Investigation of spin-trapping artifacts formed by the Forrester-Hepburn mechanism. *Free Radic Biol Med* **65**, 1497–1505 (2013).

32.   Nuchi, C. D., Hernandez, P., McClements, J. J. & Decker, E. A. Ability of lipid hydroperoxides to partition into surfactant micelles and alter lipid oxidation rates in emulsions. *J Agric Food Chem* **50**, 5445–5449 (2002).

33.   Chen, J., Li, X., Kong, B., Chen, Q. & Liu, Q. Comparative study of protein-lipid co-oxidation in whey protein isolate-stabilised oil-in-water emulsions prepared by different homogenisation methods. *Colloids Surf A Physicochem Eng Asp* **633**, (2022).

34.   Ghorbani Gorji, S., Smyth, H. E., Sharma, M. & Fitzgerald, M. Lipid oxidation in mayonnaise and the role of natural antioxidants: A review. *Trends Food Sci Technol* **56**, 88–102 (2016).

35.   Mirzanajafi-Zanjani, M., Yousefi, M. & Ehsani, A. Challenges and approaches for production of a healthy and functional mayonnaise sauce. *Food Sci Nutr* **7**, 2471–2484 (2019).

36.   Thomsen, M. K. *et al.* Mechanism of initiation of oxidation in mayonnaise enriched with fish oil as studied by electron spin resonance spectroscopy. *Eur Food Res Technol* **211**, 381–386 (2000).

37.   Takeuchi, M. *et al.* Characterization of hen phosvitin in aqueous salt solutions: Size, structure, and aggregation. *Food Hydrocoll* **129**, 107545 (2022).

38.   Byrne, B. M. *et al.* Amino Acid Sequence of Phosvitin Derived from the Nucleotide Sequence of Part of the Chicken Vitellogenin Gene. *Biochemistry* **23**, 4275–4279 (1984).

39.   Olofsson, S. O. *et al.* Apolipoprotein B: structure, biosynthesis and role in the lipoprotein assembly process. *Atherosclerosis* **68**, 1–17 (1987).

40.   Hohlbein, J. Single-molecule localization microscopy as an emerging tool to probe multiscale food structures. *Food Structure* **30**, 100236 (2021).

41.   Jabermoradi, A., Yang, S., Gobes, M. I., Van Duynhoven, J. P. M. & Hohlbein, J. Enabling single-molecule localization microscopy in turbid food emulsions. *Philosophical Transactions of the Royal Society A* **380**, (2022).

42.   Kremer, J. R., Mastronarde, D. N. & McIntosh, J. R. Computer Visualization of Three-Dimensional Image Data Using IMOD. *J Struct Biol* **116**, 71–76 (1996).
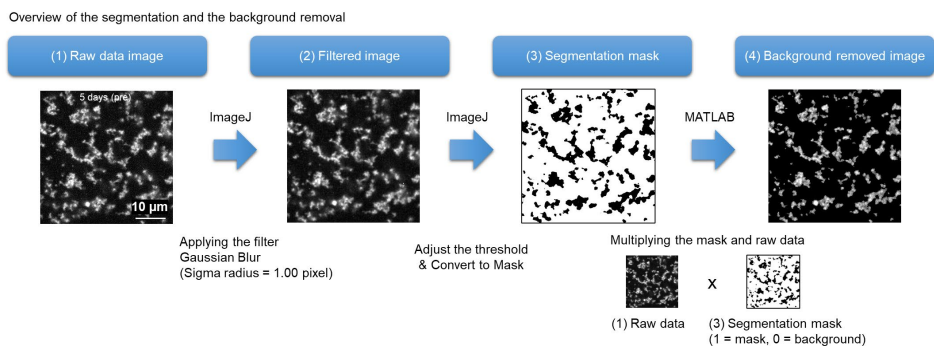
4.6   Appendix

Figure S4.1. Overview of the individual steps. To the raw data in (1), we applied the Gaussian blur filter to obtain a filtered image (2) that was then used for obtaining the segmentation mask (3). This process can be done by adjusting the threshold and then converting the image to a mask in ImageJ. After multiplying the raw data (1) with the segmentation mask (3) in MATLAB, we obtained the background removed image (4).
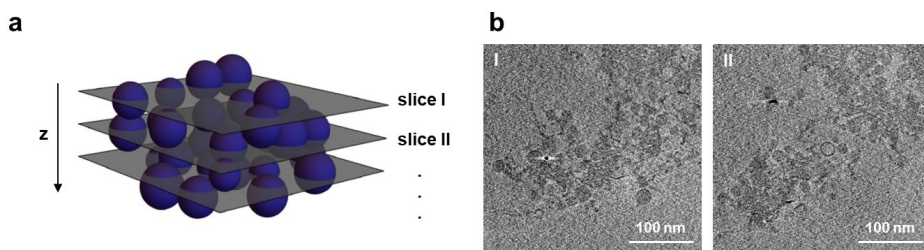

Figure S4.2. Cryo-Electron Tomography (Cryo-ET). (**a**) Schematic drawing of cross sections through reconstructed 3D intensity map commonly referred to as electron tomogram. (**b**) Two representative cross-sections of the reconstructed tomogram at different heights along the z-axis. A 9 pixel (3×3) median filter was applied to reduce noise. Contrast and brightness were adjusted for better visibility. The continuous phase of mayonnaise was incubated for 3 days at 40 °C and mixed with a solution of 10 nm gold nanoparticles for alignment of the tilt series prior to reconstruction of a tomogram. Vitrification of the samples was performed as indicated in the main text. Tilt series were acquired at an electron dose rate of 1.6 e^- $Å^{-2}$ s^{-1} with an exposure time of 1 s at a magnification of 24000× and -5 μm defocus. A total electron dose during tilt series imaging was estimated to be 72 e^- $Å^{-2}$. The sample stage was tilted from -66 ° to +66 ° with 3 ° tilt increments. Alignment and 3D reconstruction of the acquired data sets were done by IMOD[42].
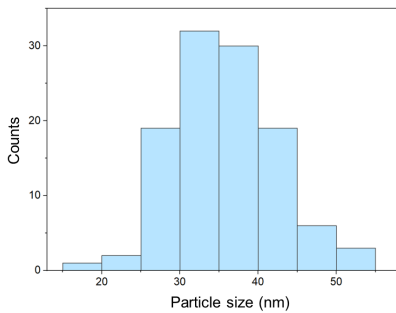
Figure S4.3. Histogram of LDL particles obtained by measuring the LDL diameter in cryo-TEM images. The diameter of dispersed LDLs was 36 ± 6 nm in the fresh sample, with the number (N) of particles analyzed 112.
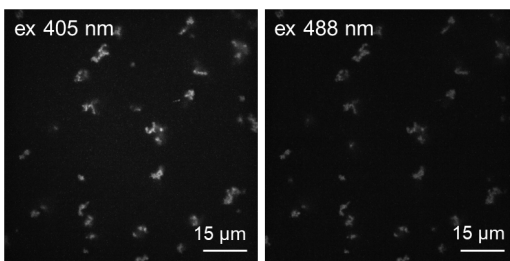
Figure S4.4. Images were measured using Rescan Confocal Microscopy (RCM). The image of excitation at 405 nm was measured after the measurement of excitation at 488 nm. The laser power of 405 and 488 nm was 2.8 mW and 9.1 mW, respectively. The image size is 88 μm x 88 μm.
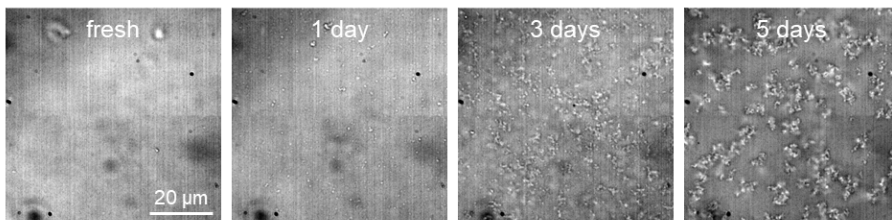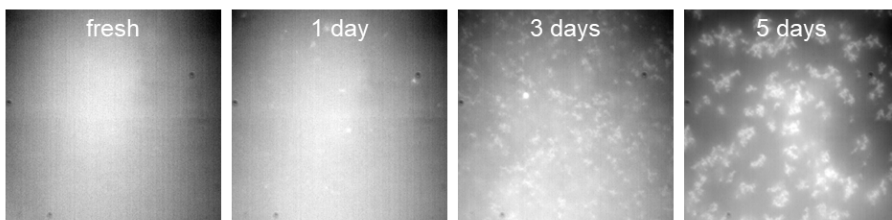
Figure S4.5. Comparing bright field microscopy in transmission and autofluorescence imaging of oxidized LDLs. (**a**) Reproduction of **Figure 4.1a** showing bright field images of the continuous phase after incubation for 0, 1, 3, and 5 days at 40 °C. The images are in line with earlier reports showing that LDL particles aggregate upon oxidation in the human plasma system. (**b**) The oxidized proteins in the continuous phase show an increased level of autofluorescence upon oxidation.
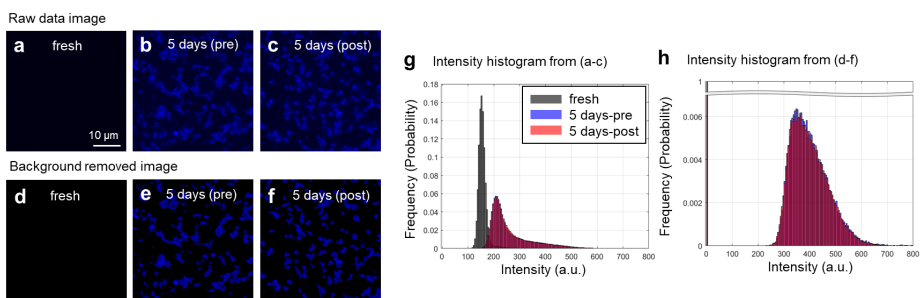
Figure S4.6. Analyzing the intensity levels of autofluorescence in the continuous phase as a function of time. (**a-c**) Raw data showing the autofluorescence at day 0 (a) and after five days for either pre- or post-addition of CAMPO AFDye 647 (b and c, respectively). (**d-f**) Same images as in a-c after (1) applying Gaussian filtering, (2) applying an intensity threshold of 313 counts per pixel and setting all lower intensities to 0, and (3) multiplying the segmentation mask with the raw data. (For further information on the steps, see **Figure S4.1**). (**g**) Intensity histograms of images in a-c, showing a mean intensity of around 156 counts per pixel at day 0 (fresh) and a broad distribution between 150-600 counts per pixel for 5 days. (**h**) Intensity histograms of the background removed images in d-f. After background removal and segmentation, the intensity histogram shows 250-600 counts per pixel. As both distributions (pre- and post-addition) are similar, we conclude that adding CAMPO-AFDye 647 either before or after oxidation does not alter the intensity levels of the autofluorescence.
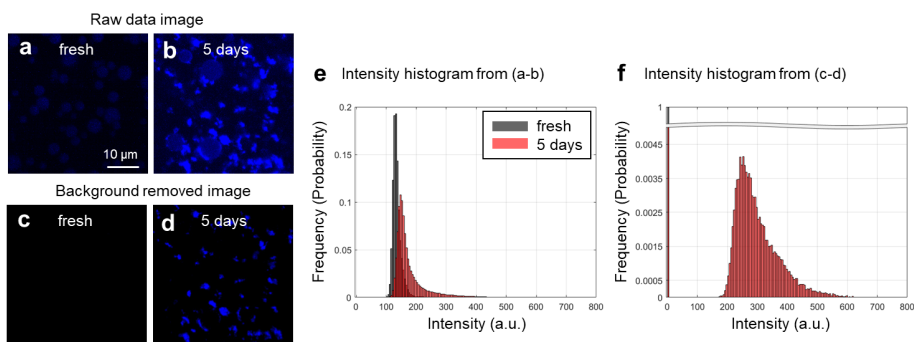
Figure S4.7. Analyzing the intensity levels of autofluorescence in oil-water emulsions. (**a-b**) Raw data showing the autofluorescence at day 0 (a) and after five days of oxidation (b). (**c-d**) Same images as in a-b after (1) applying Gaussian filtering, (2) applying an intensity threshold of 229 counts per pixel and setting all lower intensities to 0, and (3) multiplying the segmentation mask with the raw data. (For further information on the steps, see **Figure S4.1**). The droplets were detected as background and removed to analyze only proteins at the interface and in the continuous phase. (**e**) Intensity histograms of images in a-b, showing a mean intensity of around 136 counts per pixel at day 0 (fresh) and a broad distribution between 100-500 counts per pixel for 5 days. (**f**) Intensity histograms of the background removed images in c-d. After background removal and segmentation, the intensity histogram shows 200-500 counts per pixel. As the histogram shows the increase in autofluorescence intensities from day 0 (fresh) to 5 days, we conclude that not only proteins in the continuous phase show an increase in autofluorescence intensities upon oxidation but also proteins at the interface and in the continuous phase in emulsions.
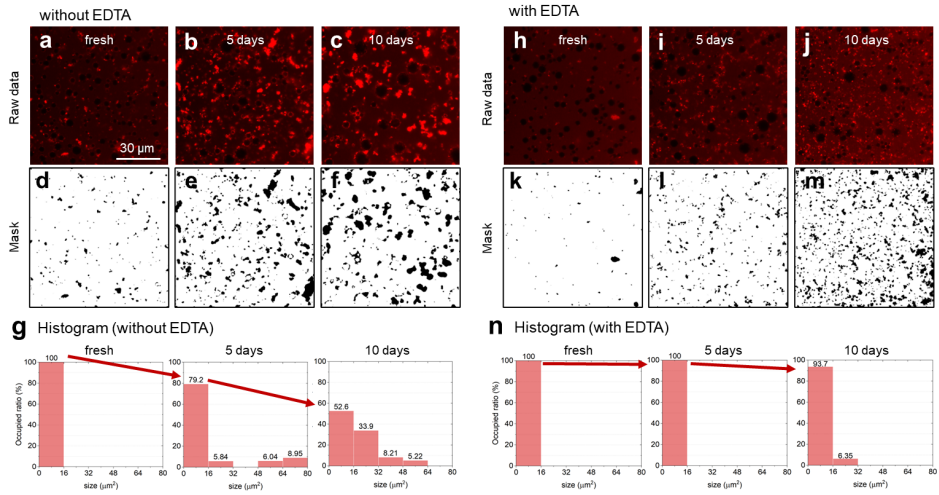
Figure S4.8. Quantifying the size of aggregates over time in the presence and absence of EDTA. (**a-c**) Raw data showing CAMPO-AFDye 647 accumulation without the addition of EDTA at day 0 (a), at day 5 and 10 of oxidation (b and c, respectively). (**d-f**) Segmentation mask in a-c at day 0 (d), at day 5 and 10 of oxidation (e and f, respectively). (**g**) Histograms showing the percentage of the total area covered by the aggregates in an entire field of view as a function of the size per aggregate. Whereas after day 0 (fresh), the entire area covered with aggregates is formed by aggregates with a size smaller than 16 μm^2, the histograms after day 5 and day 10 indicate that an increasing part of the total area is formed by aggregates with a size larger than 16 μm^2. Red arrows are added for visual guidance. (**h-j**) Raw data showing CAMPO-AFDye 647 accumulation with the addition of EDTA at day 0 (h), at day 5 and 10 of oxidation (i and j, respectively). (**k-m**) Segmentation mask in h-j at day 0 (k), at day 5 and 10 of oxidation (l and m, respectively). For obtaining the segmentation mask, an intensity threshold was set to 982 counts per pixel and all lower intensities were set to 0 (For further information about methods, see **Figure S4.1**). (**n**) Histograms showing the percentage of the total area covered by the aggregates as a function of the size per aggregate in the presence of EDTA. Here, in contrast (g), even after 10 days, the total area spanned by the aggregates is formed by >90% of aggregates with a size smaller than 16 μm^2.

4

5

Droplet size dependency and spatial heterogeneity of lipid oxidation in WPI-stabilized emulsions

Suyeon Yang*, Sten ten Klooster*, Khoa A. Nguyen, Marie Hennebelle, Claire Berton-Carabin, Karin Schroën, John P.M. van Duynhoven, Johannes Hohlbein

* These authors contributed equally

Abstract

Lipid oxidation is one of the main causes of product deterioration in emulsified food products containing polyunsaturated fatty acids. In this work, we validated the use of the lipid oxidation-sensitive fluorophore BODIPY 665/676 as a semi-quantitative marker for peroxyl radical formation by mechanistic modeling of lipid oxidation kinetics in whey protein isolate (WPI)-stabilized emulsions. We compared the decrease in long wavelength emission of BODIPY 665/676 and bulk lipid oxidation products in mono- and poly-disperse WPI-stabilized emulsions, respectively, prepared by microfluidic and colloid mill emulsification. Local observation of changes in BODIPY 665/676 fluorescence by CLSM showed an inverse relation between droplet size and lipid oxidation rate for polydisperse emulsions. To co-localize lipid and protein oxidation, we used another lipid oxidation-sensitive dye (BODIPY 581/591 C11) and a fluorescently labeled spin trap (CAMPO-AFDye 647). We observed less protein and lipid oxidation in mono- compared to poly-disperse emulsions. We attribute this finding to a more heterogeneous packing of proteins at the droplet interfaces upon high-shear colloid mill emulsification. Colloid mill emulsification also resulted in higher inter-droplet heterogeneity of protein coverage, which was also reflected in higher inter-droplet heterogeneity in lipid oxidation. We expect these insights to improve our understanding of local oxidation events and establish links between lipid and protein co-oxidation at oil-water interfaces.

5.1 Introduction

Lipid oxidation is a major factor contributing to the deterioration of the sensorial quality of oil-containing food products, especially when the oil is rich in unsaturated fatty acids[1]. In many of these products, oil is dispersed as droplets in a continuous aqueous phase[2], such as sauces, dressings, and infant milk. In these oil-in-water (O/W) emulsions, lipid oxidation is enhanced by the large interfacial area at which pro-oxidants present in the continuous phase are close to the lipids[1,3]. Lipid oxidation can be mitigated by utilizing synthetic antioxidants, packaging the products in inert atmospheres, and storing products at low temperatures[3]. Although these measures can be very effective, the food industry faces pressure to develop alternative solutions. The main drivers are the need for a more sustainable supply chain and the clean labeling trend urging manufacturers to refrain from using synthetic antioxidants[3].

Furthermore, benefits associated with cardiovascular health-promoting products with high levels of polyunsaturated fatty acids (PUFAs) such as omega-3 fatty acids[4,5] are of increasing commercial interest. However, PUFAs are particularly susceptible to lipid oxidation[6,7]. All these aspects have rekindled the research interest in lipid oxidation and its prevention in O/W emulsions. Most of our current knowledge has been obtained using one-dimensional methods[8] that measure markers of lipid oxidation in an extracted oil phase[9,10]. However, these approaches do not capture the complexity of lipid oxidation kinetics occurring at or in colloidal interfaces[11]. The complexity of lipid oxidation in O/W emulsions from the perspective of location and time has urged the field to shift from one-dimensional to spatiotemporally resolved research approaches[12].

To resolve the spatiotemporal aspects of lipid oxidation in food emulsions, confocal laser scanning microscopy (CLSM) is increasingly being deployed[13–16]. Using CLSM and fluorescent BODIPY dyes[17] enables the monitoring and localization of lipid oxidation as these BODIPY dyes undergo changes in absorption and emission spectra upon oxidation. For example, a recent publication using BODIPY 665/676 showed that oxidation in medium chain triglyceride (saturated fatty acids) emulsion droplets occurred faster when co-oxidizing unsaturated oil droplets were present[14]. This may indicate that lipid oxidation can spread from oxidizing droplets to non-oxidized ones or that oxidizing droplets influence each other. A different study using the same fluorophore showed, however, that when lipid oxidation is selectively initiated in a single droplet, the oxidation does not spread rapidly to neighboring droplets[18]. Recently our group also used BODIPY 665/676 to show that the formulation of the emulsions determined the effect of droplet size on lipid oxidation in an O/W emulsion with a high oil concentration, such as mayonnaise[16] (**Chapter 3**). In that study, we combined information from monitoring local changes in BODIPY 665/676 fluorescence with local protein autofluorescence at the single-droplet level. Despite much ambiguity in the literature on the role of droplet size dispersion and

heterogeneity of lipid oxidation, no systematic spatiotemporal investigations have been performed[15,19–21].

In the present study, we first mechanistically validate the use of BODIPY 665/676 as a monitor for local lipid oxidation in protein-stabilized emulsions. Then, using quantitative kinetic reaction modeling, we assess the scope of using BODIPY 665/676 as a peroxyl radical monitor without perturbing primary and secondary lipid oxidation products. Next, local changes in the native fluorescence of BODIPY 665/676 are compared with the formation of primary and secondary lipid oxidation products in whey protein isolate (WPI)-stabilized emulsions. Finally, we focus on the spatiotemporal heterogeneity of lipid- and protein oxidation in mono- and polydisperse WPI-stabilized emulsions, respectively, prepared by microfluidic emulsification and a colloid mill.

5.2   Materials and methods

5.2.1   Materials

Soybean oil was kindly supplied by Unilever (Wageningen, the Netherlands). Sodium phosphate dibasic heptahydrate (MW: 268.07 g/mol), sodium phosphate monobasic monohydrate (MW: 137.99 g/mol), and phosphoric acid (85.0-88.0%) were purchased from Sigma-Aldrich (Zwijndrecht, the Netherlands) to prepare a 10 mM phosphate buffer (pH 3.0). n-Hexane and 2-propanol were obtained from Actu-All Chemicals (Oss, the Netherlands). Deuterated chloroform and dimethylsulfoxide (CDCl$_3$ and DMSO-d6) were purchased from Euriso-top (Saint-Aubin, France). Tween 20 was purchased from Sigma Aldrich (Zwijndrecht, the Netherlands). WPI, purity 97.0–98.4% (BiPro®, Davisco, Switzerland) was used as received. For cleaning the microfluidic chips, we used ethanol, purity of 96% v/v (VWR International B.V., Amsterdam, the Netherlands) and piranha solution, which represents a 3:1 v/v ratio of sulphuric acid, a purity of 96% (Sigma-Aldrich, Zwijndrecht, the Netherlands) and 35 wt.% hydrogen peroxide (Sigma-Aldrich, Zwijndrecht, the Netherlands). The assay reagent for measuring the triacylglycerol (TAG) content and a standard containing TAGs (Triglycerides liquicolor mono kit) were purchased from HUMAN (HUMAN Gesellschaft für Biochemica und Diagnostica mbH, Wiesbaden, Germany). The assay reagent comprised 50 mmol/L PIPES buffer (pH 7.5), 5 mmol/L 4-chlorophenol, 0.25 mmol/L 4-aminoantipyrine, 4.5 mmol/L magnesium ions, 2 mmol/L ATP, 1.3 U/mL lipases, 0.5 U/mL peroxidase, 0.4 U/mL glycerol kinase and 1.5 U/mL glycerol-3-phosphate oxidase. The lipophilic and oxidation-sensitive dyes BODIPY 665/676 and BODIPY 581/591 C11 were purchased from Thermo Fischer (Waltham, MA, USA). CAMPO-AFDye 647 was synthesized by SyMO-Chem B.V. (Eindhoven, the Netherlands). 2,2'-Azobis (2-amidinopropane) dihydrochloride (AAPH) and sodium azide were purchased from Sigma Aldrich (Zwijndrecht, the Netherlands). Ultrapure water (18.2 MΩ) was

used for all experiments and prepared using a Milli-Q system (Millipore Corporation, Billerica, MA, USA).

5.2.2   Emulsion preparation

5.2.2.1   Preparation of oil and continuous phase

Soybean oil was stripped with alumina powder (MP112 EcoChromet ALUMINA N, Activity: Super I, Biomedicals) to remove impurities and endogenous antioxidants (in particular tocopherols)[22]. For both emulsification methods (colloid mill and microfluidics, see below), the oil was filtered using a 0.22-µm filter (Minisart High-Flow, Sartorius Stedim Biotech GmbH, Goettingen, Germany) to remove any small particles that can cause clogging of the microfluidic channels. To prepare the continuous phase, either Tween 20 or WPI was dissolved in a buffer with a concentration of 2.35 wt.%. Next, the mixture was stirred for 2 h (WPI) or 30 min (Tween 20). Sodium azide (0.05 wt. %) was added to the emulsions to prevent bacteria growth. For lipid oxidation experiments, BODIPY 665/676 was added to the stripped soybean oil (final concentration of 1 or 50 µM in the emulsion). For lipid-protein co-oxidation measurements, BODIPY 581/591 C11 was added to the emulsions prior to incubation, and CAMPO-AFDye 647 was added after incubation, before the measurements (for details regarding the structure of CAMPO-AFDye 647, see **Chapter 4**). The concentration of BODIPY 581/591 C11 and AFDye 647 in the emulsions was 1 µM.

5.2.2.2   Colloid mill emulsification

A coarse emulsion was made by adding 15 wt.% of the stripped soybean oil (with or without BODIPY 665/676) to the continuous phase, and high-speed stirring was applied at 11,000 rpm for 1 min with a rotor-stator homogenizer (Ultra-turrax IKA T18 basic, Germany). A fine emulsion was prepared by passing the coarse emulsion through a lab-scale colloid mill with a gap width of 0.32 mm (IKA Magic Lab, Staufen, Germany), operating for 1 min at 26,000 rpm. During operation, the colloid mill was cooled with water at 4 °C.

5.2.2.3   Microfluidic emulsification

To produce monodisperse emulsions, the microfluidic emulsification chip called UPE$_{10x1}$ (Upscaled Partitioned EDGE [Edge-based droplet generation]) was used (**Figure S5.1**)[23]. These chips were designed in our lab and produced in glass by deep reactive ion etching (Micronit Microfluidics, Enschede, The Netherlands). A chip with 8,064 droplet formation units (DFUs) of 10 x 1 µm (width x height) each was used. More details about the fabrication, operation, and droplet formation can be found in the literature[23].

5.2.3   Lipid and protein oxidation measurements

5.2.3.1   Initial oxygen concentration

The initial amount of oxygen was calculated (mmol/kg oil) using a headspace volume of 1.55 mL headspace with 20.9 % O_2; 46.8 mg/kg oxygen concentration in the oil[24]; and 8.1 mg/kg oxygen concentration in the continuous phase[25]. The amount of oxygen initially present was ~ 450 mmol/kg oil.

5.2.3.2   Incubation conditions

To initiate lipid oxidation, 5 mM of 2,2'-azobis (2-amidinopropane) dihydrochloride (AAPH) was added to the emulsion. A volume of 0.2 mL of the emulsion was added to 1.5 mL microcentrifuge tubes. The tubes were rotated horizontally at 2 rpm in a dark oven at 25 °C for up to 10 days. At selected time points, two tubes per independently prepared emulsion were taken and either used directly for further measurements (imaging with CLSM) or stored under inert gas at -80 °C for at least 48 hrs for lipid extraction and, subsequently, quantification of lipid oxidation products.

5.2.3.3   Oil extraction

The extraction of oxidation products was performed by adding 1 mL hexane-isopropanol (3:2 v/v) to ~ 1.5 mL emulsion and vortexing thoroughly, as described previously[26,27]. The mixture was centrifuged at 4,000xg for 20 min, and the upper layer, containing the hexane and fat, was carefully separated from the bottom layer. The hexane was evaporated under a stream of nitrogen at 25 °C until constant weight, and the remaining oil was treated with a nitrogen blanket and frozen at -80 °C for at least 48 hrs until further measurements were performed[28].

5.2.3.4   Lipid oxidation measurements by quantitative ^{1}H NMR

Hydroperoxides (primary oxidation products), aldehydes (secondary oxidation products) and triacylglycerols (as a reference for the total amount of oil) were simultaneously quantified using ^{1}H NMR, with an Advance III 600 MHz spectrometer, equipped with a 5-mm cryo-probe at 295 K, following the method described earlier[29]. In brief, 580 µL of a mixture of CDCl$_3$/DMSO-d6 (5:1 v/v) were added to ~ 20 µL extracted oil (as described in **section 5.2.3.3**) and transferred to 5-mm NMR tubes (Bruker, Billerica, Massachusetts, USA). From the recorded single pulse experiment, the glycerol backbone peaks at δ 4.4 pm were used to quantify the amount of triacylglycerols. With a band selective pulse, the region between δ 13.0 and 8.0 ppm was selectively excited for the quantification of hydroperoxides and aldehydes, following Merkx et al.[29]. The hydroperoxide signals resonate between δ 11.3 and 10.6 ppm, and the aldehydes resonate between δ 9.8 and 9.4 ppm. The calculations, including a factor that accounts for intensity loss during the selective pulse, are described elsewhere[29]. The data were processed with the Bruker TopSpin 4.0.6 software.

5.2.4 Confocal laser scanning microscopy (CLSM)

The emulsion samples were centrifuged for 5 min at 2000 rpm, and the cream layer was taken. This procedure was used to prevent the droplets from moving during the CLSM measurement. A silicon gasket was fixed on the cleaned glass, and 2 μL of the cream phase was dripped into a well of a silicon gasket (CultureWell™, GRACEBIO-LABS). The well was then sealed with a glass plate to prevent the evaporation of water from the samples. Fluorescence images were monitored on a confocal laser scanning microscope (CLSM, Leica SP8) equipped with a 63 x NA = 1.2 water immersion objective (HC PLAPO CS2, Leica) and a white-light laser with user-selectable excitation wavelengths. The scanning format was 512 x 512 pixels (62 μm by 62 μm), and the line-scanning speed was set to 100 Hz. For lipid oxidation measurements with BODIPY 665/676, the excitation wavelengths were set to 561 and 640 nm to detect oxidized and non-oxidized lipids, respectively. Detection ranges were set from 580 to 660 nm and 660 to 750 nm, respectively. For protein oxidation measurements with CAMPO-AFDye 647, the samples were excited at 640 nm with a detection range between 660 and 750 nm. BODIPY 581/591 C11 was excited at 561 and 488 nm to detect non-oxidized and oxidized BODIPY, respectively. The emission ranges were set from 580 to 660 nm and 500 to 560 nm, respectively.

5.2.5 Determination of local lipid and protein oxidation from CLSM

5.2.5.1 Local lipid oxidation

CLSM imaging data were analyzed using StarDist[30] and MATLAB. First, the raw image data from non-oxidized (ex 640 nm for BODIPY 665/676 and ex 561 nm for BODIPY 581/591 C11) and oxidized (ex 561 nm for BODIPY 665/676 and ex 488 nm for BODIPY 581/591 C11) channels were summed and used for the segmentation of oil droplets in 2D StarDist. In the segmentation steps, the versatile (fluorescence nuclei) model was used for the neural network prediction. We set the percentile low and high values to 1 and 99.8, respectively. The probability/score threshold was set to 0.5, and the overlap threshold was 0.4. After the segmentation steps, the masks were applied to the raw image data for the analysis of the fluorescence intensity changes using MATLAB. The average intensity and radii were determined for each droplet by summing up the total number of pixels for each segmented region and assuming a circle for each region. Then the radius is given by the square root of the area divided by π with 1 pixel corresponding to an area of 0.12 by 0.12 μm. For the normalized data set, the averaged intensities of red fluorescence in each droplet were divided by the total average red fluorescence intensity in the fresh sample (**Figure S5.2**).

5.2.5.2 Local protein oxidation

The mask from oil droplet segmentation was applied to the raw protein oxidation maps measured via accumulation of the spin trap CAMPO-AFDye 647 (ex 640 nm). Next, the applied images

were filtered to visualize only the accumulation of the CAMPO-AFDye 647 at the droplet interface. Filtered images were obtained by applying the segmentation mask from the oil droplets on the raw data. Then, to remove the background intensity from within the oil droplets, only the pixels with intensity counts exceeding 30% of the maximum fluorescence intensity from all segmented droplets were considered for further calculation. With these segmented images, the level of protein oxidation per droplet was determined by first summing up all the intensities per droplet and dividing it by the circumference of the droplet using the radius which we obtained from the area in pixels after segmentation.

5.2.6   Droplet size measurements

5.2.6.1   Static light scattering (SLS)

The oil droplet size of the whole emulsions was measured by static light scattering (SLS) (Malvern Mastersizer 3000, Malvern Instruments Ltd., Malvern, Worcestershire, UK), using a refractive index of 1.465 for the dispersed phase and 1.33 for the dispersant (water); and an absorption index of 0.01.

5.2.6.2   Dynamic light scattering (DLS)

The continuous phase and the smallest oil droplets were separated from the larger oil droplets by centrifuging 2 mL of emulsion at 20,000xg for 42 min in a 2-mL microcentrifuge tube and collecting ~ 0.3 mL of the subnatant from the bottom of the tube. The size of the colloidal structures present in this subnatant was measured by dynamic light scattering (DLS) (Zetasizer Nano ZS, Malvern Instruments Ltd., Malvern, Worcestershire, UK). The refractive index was 1.47 for the dispersed phase, and the absorbance was 0.01.

5.2.6.3   Oil content

The amount of lipids corresponding to very small droplets was quantified using a colorimetric method for measuring the triacylglycerol content (Triglycerides Liquicolor Mono kit, HUMAN)[31,32]. In brief, the subnatant samples, obtained as described in the section above, were diluted to a range of 0.4-4 g/L, and about 20 µL of the sample was weighed into a 2-mL microcentrifuge tube. Next, 1 mL of assay reagent was added, and the samples were subsequently incubated in a heating block at 800 rpm for 20 minutes at 20 °C. The absorbance was measured at a wavelength of 500 nm, and the concentration was calculated using a calibration curve (0.4-4 g triglycerides/L).

5.2.6.4   Combined droplet size distribution

For visualization purposes, the distributions obtained by DLS and SLS were superimposed on the same graph. For this, the relative intensities from the DLS measurements were adjusted based on the actual oil contents in the subnatant (see below). The relative intensities from the SLS

measurements were adjusted based on the assumption that its oil content was one minus the oil content in the subnatant.

5.2.6.5   Confocal laser scanning microscopy (CLSM)

The droplet sizes of monodisperse emulsions were measured by CLSM. The same segmentation steps (**section 5.2.5**) were applied to the raw images. The number of pixels was counted per droplet, and the radius was calculated based on the sum of pixels (**Figure S5.2**).

5.2.7   Experimental design

For each measurement, at least two emulsions were independently prepared, except for the measurements with emulsions containing 50 µM of BODIPY 665/676, for which only one emulsion was prepared. Additionally, droplet size and lipid oxidation measurements were performed on two independently incubated samples from the same emulsion for each time point.

5.2.8   Quantitative kinetic model

5.2.8.1   Lipid oxidation reactions in the kinetic model

A kinetic model was employed to describe lipid oxidation reactions (R.1 -R.7, **Table 5.1**) with a set of kinetic equations using a mixture of first and second order reactions (**Table S5.1**). As AAPH and BODIPY are present in the system, reactions 8 and 9 (**Table 5.1**) were incorporated into the kinetic model[33].

Table 5.1. The summary of lipid oxidation reactions that can occur at the water-oil interface in O/W food emulsions.

Lipid oxidation reactions	
$LH \xrightarrow{k_1} L^* + H^*$	R.1
$L^* + O_2 \xrightarrow{k_2} LOO^*$	R.2
$LOO^* + LH \xrightarrow{k_3} LOOH + L^*$	R.3
$LOOH \xrightarrow{k4} LO^* + OH^*$	R.4
$OH^* + LH \xrightarrow{k_5} L^* + H_2O$	R.5
$LO^* + LH \xrightarrow{k_6} AD + L^*$	R.6*
$LO^* + LH \xrightarrow{k_7} EP + L^*$	R.7*
Reactions in the presence of AAPH and BODIPY	
$AAPH \xrightarrow{k_{AAPH}} 2L^* + N_2$	R.8
$LOO^* + BODIPY \xrightarrow{k_{BODIPY}} non\text{-}radical\ products$	R.9

*R.6-R.7 results from the combination of multi-chain reactions to form aldehydes, epoxides, and EPOOHs[34].

The surface-volume mean diameter (D_{32}) corresponds to:

$$D_{32} = \frac{\sum_i n_i d_i^3}{\sum_i n_i d_i^2},$$

(5.1)

where n_i is the number of droplets of a diameter d_i.

To estimate the impact of changes in D_{32} on the formation of lipid oxidation products, we varied D_{32} with deviations of σ. The model related the concentrations of O_2, AAPH, and BODIPY 665/676 at the oil-water interface to droplet sizes using their partition coefficients and D_{32}. The concentration over time of the compounds with D_{32} is denoted as $[C]$. Then, with $D_{32} \pm \sigma$, the varied concentration denoted as $[\tilde{C}]$ can be calculated as (**Appendix 5.5.1**)

$$[\tilde{C}] = \frac{D_{3,2}}{D_{3,2} \pm \sigma} \times [C].$$ (5.2)

5.2.8.2 Estimation of kinetic constants and initial radical concentrations

The model required estimating 13 parameters: k_1 to k_7 (R.1 – R.7, **Table 5.1**), k_{AAPH} and k_{BODIPY} (R.8 and R.9, **Table 5.1**), and initial concentration of L*, LOO*, LO*, and OH*. These parameters were calculated by a multi-response optimization method, for instance, by fitting hydroperoxide and aldehyde profiles simultaneously, using MATLAB 2021b software (Mathworks, Natick, MA, USA)[35].

The optimization procedure was applied to fit experimental datasets with 1 µM BODIPY 665/676. Based on the literature, k_3 (R.3 in **Table 5.1**) was found to be approximately two times lower than k_{BODIPY} (R.9 in **Table 5.1**)[36], thus, we fixed k_3 as $0.5 \times k_{\text{BODIPY}}$.

Typically, the optimization requires starting values of all parameters which we obtained from the literatures[33,37] (**Table S5.2**). Then, for every set of initial starting values, the *'lsqnonlin'* algorithm simultaneously determined their estimated values by minimizing the sum of the squared errors between the experimental (X_{exp}) and numerical (X_{num}) datasets (**Equation 5.3**). Since each set of starting values returned different estimated values, the optimal estimated values were selected based on the least squared error (**Equation 5.3**).

$$\left\| X_{\text{exp}} - X_{\text{num}} \right\|_2^2 = \sum_{i=1}^{n_t} \left(X(t_i)_{\text{exp}} - X(t_i)_{\text{num}} \right)^2,$$ (5.3)

where t, i, and n_t indicate storage time, index of time points, and the total number of time points, respectively. After fitting the numerical and experimental datasets, the precision of the estimated values was evaluated using Monte Carlo simulations with 200 iterations to calculate the standard deviations[38]

$$X_{\text{noise,exp}} = X_{\text{exp}} + \sigma r_1 r_2,$$ (5.4)

where X_{noise}, and X_{exp} are the noised and original experimental data, respectively. σ is the experimental standard deviation estimated for each experimental data, and r_1 and r_2 are random values varying from 0 to 1.

5.2.8.3 Simulation of the impact of BODIPY 665/676 and droplet size on lipid oxidation

Using the estimated values of 13 parameters (**Table S5.1**), the formation of lipid oxidation products was simulated over time with BODIPY 665/676 concentrations of 0, 1 and 50 µM and

with a fixed D_{32} value. Then the simulated data were compared with the experimental datasets measured by NMR. To illustrate the impact of droplet sizes on lipid oxidation products, model simulations were conducted using D_{32} + 0.2 and D_{32} - 0.2 μm, while keeping the initial concentration (1 μM) of BODIPY fixed. Furthermore, we simulated the concentration of native BODIPY 665/676 over time and compared it with the decrease in the experimentally obtained and normalized red fluorescence intensities. The integral of peroxyl radicals (LOO*) over time was also calculated based on the reaction mechanisms.

5.3   Results and discussion

5.3.1   Microstructural characterization of Tween 20- and WPI-stabilized emulsions

Poly- and monodisperse emulsions were prepared with a lab-scale colloid mill or by microfluidic emulsification, respectively. The droplet size distribution of colloid mill-made emulsions was obtained using DLS and SLS, and the droplet size distribution of microfluidic-made emulsions was obtained using CLSM (**section 5.2.6**). The surface volume mean diameter (Sauter mean diameter, $D_{3,2}$) of the colloid mill-made emulsion, stabilized by Tween 20, obtained from SLS and DLS was 0.5 μm (**Figure 5.1**). By centrifugation of the colloid mill emulsions, a subnatant was obtained, which contained small droplets (< 200 nm diameter). The size distribution of these small droplets, as determined by DLS, and their volume fraction is shown in **Figure 5.1**. As covered by DLS and SLS, the size distributions spanned two to three orders of magnitude. The Tween 20-based emulsion made with microfluidics showed a $D_{3,2}$ of 4.5 μm (obtained from CLSM), which is larger than for the colloid-mill made emulsions, although their size distributions partially overlap. Similarly, the WPI-stabilized emulsion prepared with the colloid mill had a smaller average droplet size ($D_{3,2}$ = 1.4 μm, from SLS and DLS) than the WPI-stabilized emulsion prepared with microfluidics ($D_{3,2}$ = 4.5 μm, from CLSM).
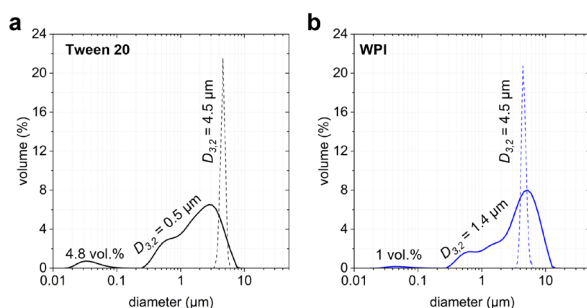
Figure 5.1. Volume fraction per diameter distributions of emulsions stabilized with Tween 20 (**a**, black) and WPI (**b**, blue). Solid lines represent emulsions prepared with the colloid mill, and dashed lines with microfluidics. The droplet size distributions for the colloid mill-made emulsion were obtained by combining the SLS results on the whole emulsion sample with the DLS results on the subnatant sample obtained after centrifugation (**section 5.2.6**). The $D_{3,2}$ values were obtained from the CLSM results for the microfluidic-made emulsions and from SLS and DLS for the colloid mill-made emulsions. The volume fraction of small droplets ($D_{3,2}$ < 200 nm) in Tween 20 and WPI emulsions is 4.8 and 1 %, respectively.

5.3.2 Mechanistic validation of BODIPY 665/676 as a quantitative marker for local lipid oxidation

BODIPY 665/676 has been previously used as a marker to localize lipid oxidation in food emulsions[13–16]. Oxidation of BODIPY 665/676 can be detected by a shift of fluorescence emission from the red to the green spectral region upon reaction with peroxyl radicals[39,40]. This reaction causes the cleavage of the phenylbutadiene moiety and the formation of an acid group, which can occur at several positions (**Figure S5.3**)[36,41]. It has been reported that peroxyl radicals react more rapidly with BODIPY 665/676 (R.9, **Table 5.1**) than with unsaturated fatty acids (R.3, **Table 5.1**)[36]. However, whether these reactions interact or compete with lipid oxidation is unclear. BODIPY 665/676 may, for example, partially inhibit the formation of hydroperoxides and aldehydes following reactions 3 and 4 (**Table 5.1**). We, therefore, carried out a mechanistic validation of using the fluorescence change of BODIPY 665/676 as a quantitative marker for lipid oxidation.

First, we measured the primary and secondary oxidation products in 2 wt.% WPI-stabilized polydisperse emulsions with 0, 1 or 50 µM BODIPY 665/676 in the oil phase. These polydisperse emulsions were prepared with separate colloid mill preparations as the different BODIPY 665/676 levels needed to be added in the oil phase before emulsification. In the first instance, the experimental data suggest that the emulsion prepared with BODIPY 665/676 oxidized less rapidly than those that did not contain BODIPY 665/676, except for after six days, when the values were closer to each other again (**Figures 5.2a & b**).

To assess the influence of adding BODIPY 665/676 on lipid oxidation in a systematic manner, our kinetic model was used to simulate the formation of lipid oxidation products in the presence of BODIPY 665/676. In this model, the kinetic constants and initial radical concentrations were estimated by fitting the numerical kinetic profiles[33] of hydroperoxides and aldehydes to the experimental datasets with 1 µM BODIPY 665/676. With the estimates (**Table S5.2**), the concentrations of oxidation products and all other parameters were simulated as used in the experiments.

It was reported earlier that the reaction of BODIPY 665/676 with peroxyl radicals (k_{BODIPY} in R.9, **Table 5.1**) has a higher kinetic constant than the formation of lipid hydroperoxides (k_3 in R.3, **Table 5.1**)[36]. Our results show, however, that the kinetic rate (not the kinetic constant) of the reaction between BODIPY 665/676 and peroxyl radicals is 4.5×10^7 times lower than the hydroperoxide formation, which is due to the high initial concentration of lipid substrates (**Appendix 5.5.2**). This finding explains why our simulation shows that at the low concentration working range (< 50 µM), BODIPY 665/676 does not influence the formation of lipid oxidation products. Using a 10^4 higher concentration of BODIPY 665/676 (500 mM) our simulations

showed a higher reaction rate than hydroperoxide formation, resulting in a slower lipid oxidation rate (**Figure S5.4**).

The simulations showed that the differences in the experimentally obtained kinetic curves between emulsions including 0, 1, or 50 µM of BODIPY 665/676 (**Figures 5.2a & b**) could not be attributed to the different concentrations of BODIPY 665/676. These emulsions, however, were also prepared by different emulsification procedures. These procedures can give rise to small variations in droplet size distributions, hence we simulated hydroperoxide and aldehyde kinetic curves for emulsion with surface-volume mean diameter ($D_{3,2}$) of 1.2, 1.4, and 1.6 µm (**Figure S5.5**). The simulations show a clear difference in kinetic curves for these minor variations in $D_{3,2}$, which indicates that the variation in kinetic curves in **Figure 5.2** can be attributed to minor variations in the distribution of droplet sizes.

Next, to establish a quantitative interpretation of a change in BODIPY 665/676 fluorescence, we used mechanistic simulations and compared the experimental fluorescence data with 1 µM of BODIPY 665/676. BODIPY 665/676 is known to react with LOO*, which makes BODIPY 665/676 an effective lipid oxidation marker. The correlation between BODIPY 665/676 and the concentration of LOO* is, however, still unclear. Direct measurements of LOO* in emulsions are experimentally difficult due to the short lifetime of this radical; therefore, the LOO* concentration was simulated using the kinetic model. The concentration of native BODIPY 665/676 over time was calculated as follows:

$$[\text{BODIPY}(t)] = [\text{BODIPY}(0)] - \int_0^t k_{\text{BODIPY}} \times [\text{LOO}^*(t')] \times [\text{BODIPY}(t')] dt', \tag{5.5}$$

where BODIPY 665/676 is used in a working range of 1 - 50 µM. The integral term in **Equation 5.5** indicates BODIPY 665/676 consumption over time. As a simplified expression, **Equation 5.5** can be written as:

$$[\text{BODIPY}(t)] \approx [\text{BODIPY}(0)] - \int_0^t k'_{\text{BODIPY}} \times [\text{LOO}^*(t')] \, dt', \tag{5.6}$$

where [BODIPY(t)] and [LOO*(t)] indicate concentrations of BODIPY 665/676 and peroxyl radicals (LOO*) at time t, respectively (in mmol/kg oil), and $k'_{\text{BODIPY}} = k_{\text{BODIPY}} \times [\text{BODIPY}(0)]$.

In **Figure 5.2c**, the decrease in experimental red fluorescence intensity of BODIPY 665/676 upon oxidation was compared with the simulated concentration of the native state of BODIPY 665/676 using the kinetic model. The agreement between experimental and simulation data (from **Equation. 5.5** and **5.6**) indicates that the kinetic model can adequately describe the concentration of native BODIPY 665/676. Furthermore, the approximate concentration of LOO* (from **Equation. 5.6**) from the kinetic model shows that a decrease in BODIPY 665/676 fluorescence can simply be interpreted as the integral of [LOO*] over time (**Figure 5.2d**).
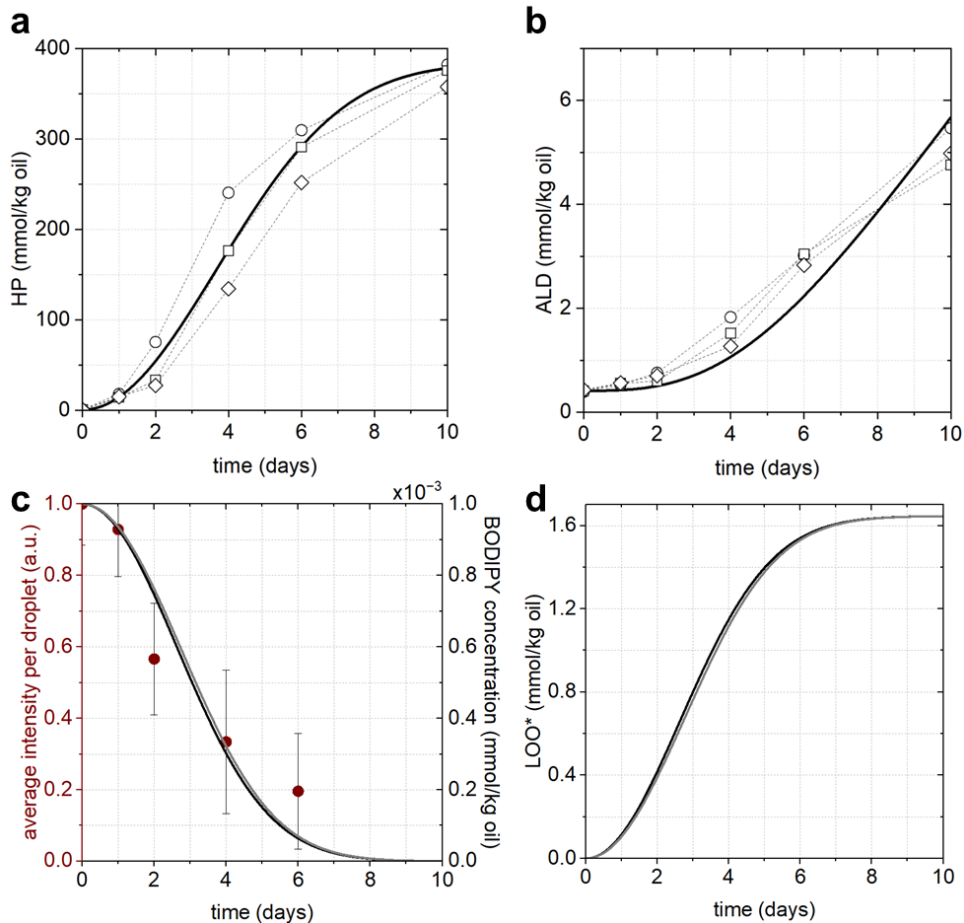
Figure 5.2. Validation of using BODIPY 665/676 to probe oxidation by experimental and simulated data. (**a-b**) The formation of hydroperoxides (HP) (a) and aldehydes (ALD) (b) in the absence and presence of BODIPY 665/676 as measured by NMR. The samples were prepared with a colloid mill (polydisperse emulsions) and stabilized by 2 wt% WPI. Markers corresponding to samples containing 0 (circle), 1 (square), and 50 µM (diamond) BODIPY 665/676. The black line indicates the numerical datasets (simulation) of total HP and ALD. Note that the simulation results from 0, 1, and 50 µM showed no differences, whereas the experimental results showed differences, which we attribute to the differences in droplet size distribution between the sample production (**Figure S5.5**). (**c**) Correlation between experimental (fluorescence intensity) and simulation data (BODIPY 665/676 concentration) with 1 µM BODIPY 665/676. (Left y-axis) Red circles indicate the intensity decrease of red fluorescence. Error bars denote the standard deviations of many droplets from two independently incubated samples. We note that the large standard deviation originates from many droplets in the range of 1 - 6 µm diameter. More than 2000 oil droplets were used for the analyses at each time point. (Right y-axis) Solid lines indicate the concentration of native BODIPY 665/676 calculated from **Equation. 5.5** (black) and **6** (gray). (**d**) Simulated results of LOO* concentration, which reacts with BODIPY 665/676. Lines show the integration term divided by the constant (k_{BODIPY}) in **Equation. 5.5** (black) and the approximated concentration of LOO* in **Equation. 5.6** (gray).

5.3.3   Lipid oxidation in Tween 20- and WPI-stabilized monodisperse emulsions

Emulsion samples containing 2 wt.% of Tween 20 or 2 wt.% of WPI and prepared with microfluidic emulsification[23] were incubated with 5 mM AAPH at 25 °C in the dark. Hydroperoxides (HP) and aldehydes (ALD) were quantified over incubation (**Figures 5.3a & b**), and the decrease in red fluorescence emission of BODIPY 665/676 was measured with CLSM (**Figure 5.3c**). In the monodisperse emulsion stabilized by WPI, the concentration of lipid hydroperoxides and aldehydes increased slightly over the first four days and more rapidly between four and six days of incubation (**Figures 5.3a &b**). Similar effects were seen in the fluorescence intensity, which showed a minor red fluorescence decrease in the first two days, followed by a more rapid decrease between four and six days (**Figure 5.3c**). The decrease in red fluorescence was accompanied by the appearance of green fluorescence (excitation at 561 nm), confirming that the BODIPY 665/676 dye was getting oxidized (**Figure S5.6**). The simultaneous decrease in native (red) fluorescence and increase in hydroperoxides is in line with the formation of lipid peroxyl radicals in the droplets, leading to an increase in both lipid and BODIPY 665/676 oxidation[39,40] as we described in **Figure 5.2** with a kinetic model relating peroxyl radical formation to BODIPY 665/676 oxidation.

For the monodisperse emulsions prepared with Tween 20, the formation of hydroperoxides increased more slowly over the six days of incubation compared to the WPI-stabilized emulsions (**Figures 5.3a & b**), whereas a rapid decrease in red fluorescence was already observed in the first two days (**Figure 5.3c**). This decrease was, however, not accompanied by an increase in green fluorescence, indicating that the BODIPY 665/676 dye was not oxidized (**Figure S5.6**). The loss in red fluorescence is likely caused by the enhanced solubilization of BODIPY into the continuous phase when Tween 20 is present[42]. This finding indicates that when BODIPY 665/676 is used to study lipid oxidation, both the red and green fluorescence of respectively the native and oxidized states need to be assessed in order to confirm that the fluorophore is acting as an oxidation monitor.
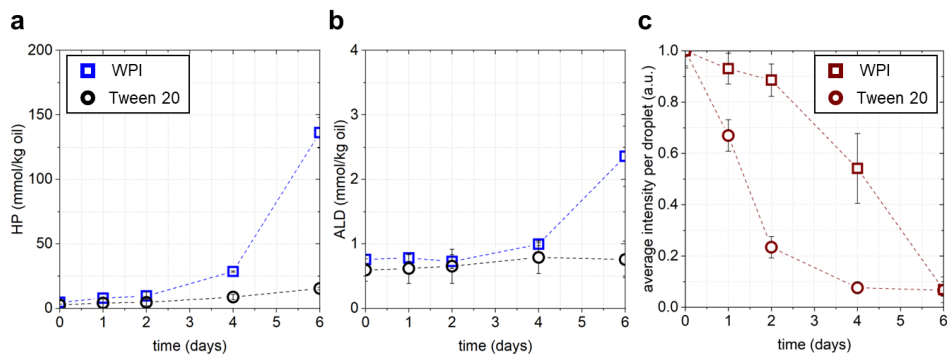
Figure 5.3. Lipid oxidation in microfluidic-made mono-disperse emulsions stabilized by 2 wt.% WPI (square) or 2 wt.% Tween 20 (circle). (**a-b**) Formation of hydroperoxides (HP) (a) and aldehydes (ALD) (b) as a function of time measured by NMR. Error bars (sometimes hidden by the symbol) denote standard deviations of four measurements including two independent sample preparations. The result indicates that WPI-stabilized emulsions get oxidized faster than Tween 20 emulsions in a mono-disperse system. (**c**) Decrease of red fluorescence by BODIPY 665/676 in mono-disperse emulsions. Symbols in c correspond to droplet sizes of 4-5 µm from WPI- (square) and Tween 20 (circles) stabilized emulsions. Error bars denote the standard deviations of many droplets from two independently incubated samples. The dashed lines connecting the average values are for visual guidance.

The formation of hydroperoxides and aldehydes in the monodisperse WPI-stabilized emulsions was faster than in the monodisperse Tween 20-stabilized emulsions (**Figure 5.3a & b**). We initially expected WPI-stabilized emulsions to oxidize slower than the Tween 20-stabilized emulsions due to the antioxidant role of proteins in the continuous phase[43]. Here, we attribute the faster oxidation of the WPI-stabilized monodisperse emulsion to multiple factors, such as the potential presence of transition metals at the interface originally present in WPI and/or a more heterogenous interfacial structure induced by the various proteins present in WPI. Since we cannot access local oxidation kinetics by using BODIPY 665/676 for Tween 20-stabilized emulsions, we will refrain from a further interpretation of their bulk kinetic data (**Figure S5.7**).

5.3.4   Lipid oxidation in WPI-stabilized polydisperse emulsions

The formation of hydroperoxides and aldehydes in the colloid mill-made polydisperse emulsions stabilized by WPI proceeded faster than in monodisperse emulsions made with microfluidic devices (**Figure 5.4a & b**). Furthermore, we saw a clear difference between the decrease in red fluorescence emission for small (1-2 µm) and large droplets (4-5 µm) (**Figure 5.4c**). The faster lipid oxidation in small droplets compared to large ones is in line with our recent study, where we found that more lipid oxidation products are present in the smallest droplets present in the emulsions[44]. In **Figure 5.4c**, we also indicated the decrease of the red fluorescence for 4-5 µm sized droplets in monodisperse emulsions. The monodisperse droplets further showed a slower decrease over time than their similar-sized counterparts in the polydisperse emulsion. We note

that the mono- and polydisperse emulsion were manufactured with microfluidic and high-shear colloid mill emulsification, respectively. We explain the difference in oxidation kinetics between similar (4-5 µm) sized droplets by different packing of the WPI proteins at the interface. Microfluidic emulsification is more likely to lead to homogeneous coverage of proteins at the interface than the use of a colloid mill.

Overall, our results show that lipid oxidation in WPI-stabilized emulsions is determined by both droplet size as well as the emulsification method used. We attribute the latter to the difference in the packing of WPI-proteins at the droplet interface caused by mild and high shear emulsification. For droplets prepared with the same emulsification procedure, size is the most dominant factor in lipid oxidation.
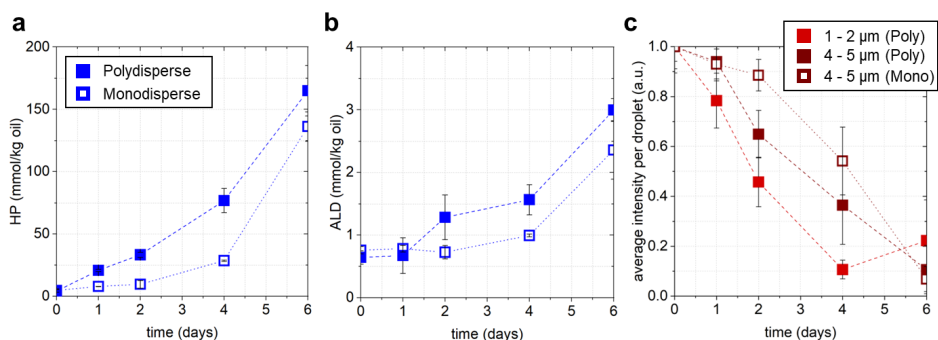

Figure 5.4. Lipid oxidation in colloid mill-made poly-disperse (filled-square) or in microfluidic-made mono-disperse (empty square) emulsions stabilized by 2 wt.% WPI. (**a-b**) Formation of hydroperoxides (HP) (a) and aldehydes (ALD) (b) as a function of time measured by NMR. Error bars (sometimes within the symbol) denote standard deviations of four measurements including two independent sample preparations. The result indicates that poly-disperse emulsions showed faster oxidation than mono-disperse emulsions. (**c**) Decrease of red fluorescence by BODIPY 665/676 in poly- and mono-disperse emulsions. Symbols in c correspond to droplet sizes of 1-2 µm (filled-square, red) and 4-5 µm (filled-square, dark red) from the poly-disperse emulsions and 4-5 µm (empty square, dark red) sized-droplets in the monodisperse system. Error bars denote the standard deviations of many droplets from two independently incubated samples. The dashed lines connecting the average values are for visual guidance.

We note that when comparing local (microscopy) and bulk (NMR) assessments of lipid oxidation, one should consider the spatial resolution limit of the imaging technique used. In our CLSM experiments, the smallest droplets in which BODIPY 665/676 fluorescence could be quantified were ~ 1 µm in diameter. In our polydisperse WPI-stabilized emulsion, ~ 14 vol.% of the oil was present in droplets smaller than 1 µm and ~ 1 vol.% in droplets smaller than 0.2 µm, which represents the conventional resolution limit of CLSM. It was shown that more lipid oxidation products were present in the smallest droplets, which implies that lipid oxidation is underestimated if only droplets larger than 1 µm are analyzed by CLSM[44]. The oxidation in

small droplets could be further studied with super-resolution techniques which allow resolving features smaller than 200 nm[45]. This will be further discussed in **Chapter 7**.

5.3.5   Spatial heterogeneity of lipid and protein oxidation in WPI-stabilized emulsions

Our comparison of local lipid oxidation in mono- and polydisperse emulsions indicated that in the latter, proteins are more heterogeneously packed at the droplet interfaces[46]. We pursued this by further investigating spatial inter- and intra-droplet heterogeneity of lipid and protein oxidation. Red fluorescence of BODIPY 665/676 in WPI-stabilized polydisperse emulsions showed clear inter-droplet heterogeneity in the oxidation of similar-sized droplets as quantified by the violin plots for droplets with 3-5 µm diameter (**Figure 5.5a**). This heterogeneity in fluorescence intensity levels confirms that for similar-sized WPI-stabilized droplets in a monodisperse emulsion, oxidation levels can differ greatly[47]. We attribute this to the aforementioned heterogeneous coverage of droplet interfaces, which prompted us to further investigate the interplay of lipid and protein oxidation at droplet interfaces of WPI-stabilized emulsions with CLSM. Here, we used CAMPO-AFDye 647[48] to localize protein radical formation and BODIPY 581/591 C11 for mapping lipid oxidation. This blue-shifted alternative BODIPY dye does not overlap with the emission of CAMPO-AFDye 647, which enabled us to co-localize protein and lipid oxidation. BODIPY 581/591 C11 has the same core structure as BODIPY 665/676 but contains only one phenylbutadiene moiety, which makes it less sensitive to lipid oxidation[39,40].

Co-localization of lipid and protein oxidation in polydisperse emulsions is shown in **Figure 5.5b** as overlayed raw image data. The raw image data was then segmented and filtered for further analysis. The images of the colloid-mill made emulsion show spots of CAMPO-AFDye 647 accumulation at the interface (**Figure 5.5c**), suggesting that proteins at the interface oxidize heterogeneously at both the inter- and intra-droplet level. For the monodisperse WPI-stabilized emulsions, only a minor accumulation of CAMPO-AFDye 647 took place compared to the polydisperse emulsions (**Figure 5.5d**). This finding indicates that little protein oxidation occurred at the interface, which we attribute to the thinner and more homogeneous coverage of the droplet interfaces due to the mildness of the microfluidic emulsification. This result aligns with the slower lipid oxidation for monodisperse emulsions observed previously (**Figure 5.4**).

To quantify the interplay between protein- and lipid oxidation at the intra-droplet level, we first determined the average fluorescence intensity from BODIPY 581/591 C11. Next, we integrated the fluorescence by CAMPO-AFDye 647 and divided the value by the circumference ($2\pi r$) with the calculated r from the segmentation to obtain a measure for protein oxidation at the interface (**Figures 5.5e & f**). This quantification revealed heterogeneity of lipid oxidation, as discussed

previously (**Figure 5.5a**), and also for protein oxidation (**Figure 5.5g**). In polydisperse emulsions, both lipid and protein showed more oxidation for smaller droplets.

To sum up, in WPI-stabilized emulsions, both lipid and protein oxidation at the interface occurred faster in the polydisperse emulsion than in the monodisperse one (**Figures 5.4a & b and 5.5c & d**). This finding can be explained by both the differences in the emulsification process and the presence of smaller droplets, as we described in the previous section. Thus, our results can help to explain ambiguous outcomes of previous studies on the droplet size dependency of lipid oxidation, as different emulsification methods can lead to different droplet surface coverage and/or droplet size distributions[49,50]. Unfortunately, our current data do not provide clear evidence of protein oxidation induced by lipid oxidation. Both oxidation mechanisms may occur independently, or the oxidation initiator (AAPH) does not only promote lipid oxidation but also protein oxidation at the interface.
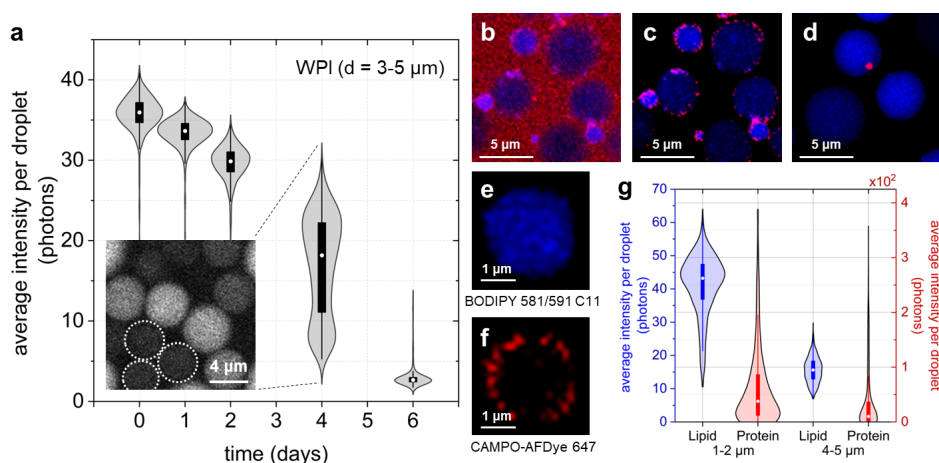

Figure 5.5. Imaging the heterogeneity of lipid and protein oxidation in mono- and polydisperse emulsions stabilized by WPI. (**a**) Heterogeneous lipid oxidation in monodisperse emulsions, including BODIPY 665/676, is indicated by a broad distribution of fluorescence intensity per droplet excited at 640 nm. The average number of droplets used for analysis is ~1000 for each day. The box plot shows the data in the 25 to 75 % range, and the white circle in the box plot shows the median value. (**b-g**) Co-localization of lipid and protein oxidation was assessed using BODIPY 581/591 C11 (excitation at 488 nm for the oxidized droplets) and CAMPO-AFDye 647 (excitation at 640 nm). (**b**) Raw image data of colloid mill-made emulsions with combined excitation channels at 488- and 640 nm. The red color shows the accumulation of CAMPO-AFDye 647, and the blue indicates lipid oxidation. (**c-d**) Segmented droplet images of a colloid mill- (c) and microfluidic-made emulsions (d). (**e-f**) Segmented images of oil droplets with BODIPY 581/591 C11 (e) and interface with CAMPO-AFDye 647 (f). Quantification steps were performed as described in **section 5.2.5**. Lipid oxidation was analyzed with the average intensity at an excitation of 488 nm. To assess protein oxidation, CAMPO was excited at 640 nm. (**g**) Droplet size dependency of lipid- and protein oxidation in polydisperse emulsions. Lipid and protein oxidation in two different size ranges of droplets (1-2 µm and 4-5 µm) are compared. The numbers of analyzed droplets for 1-2 and 4-5 µm diameter are 764 and 305, respectively. As we took the data from a single measurement, we did not perform a normalization step (**Figure S5.2**).

5.4   Conclusions

In this study, the intensity decrease in red fluorescence emission of BODIPY 665/676 was used to unravel droplet size-dependent spatial heterogeneity of lipid oxidation in WPI-stabilized emulsions. Care should be exerted that fluorescence of both non-oxidized and oxidized states are monitored since a decrease in native fluorescence can also be caused by the further dissolution of the dye. Such an effect can occur when an emulsifier is present in a concentration high enough to dissolve the dye in the continuous phase. Through kinetic modeling, we showed that no perturbation of lipid oxidation occurs with the chosen low concentration of BODIPY 665/676. From the model, it can be inferred that the decrease in red fluorescence of BODIPY 665/676 correlates with the integral of peroxyl radical concentration over time. Microfluidic and colloid mill emulsification result in mono- and polydisperse WPI emulsions (**Figure 5.6**). Lipid oxidation kinetics of these emulsions, as observed locally by BODIPY 665/676 and in bulk by NMR, can be explained by differences in droplet size distribution and heterogeneous packing of proteins at the droplet interfaces (**Figure 5.6**). The different packing of proteins at the droplet interfaces of mono- and polydisperse WPI emulsions could be visualized by the accumulation of the CAMPO-AFDye 647 spin trap at droplet interfaces. Our results show that both lipid and protein oxidation proceeds in highly heterogeneous fashions in WPI-stabilized emulsions, which cannot be shown by bulk measurements of lipid oxidation products. We expect that these insights contribute to improving our understanding of local co-oxidation of lipids and proteins at droplet interfaces.

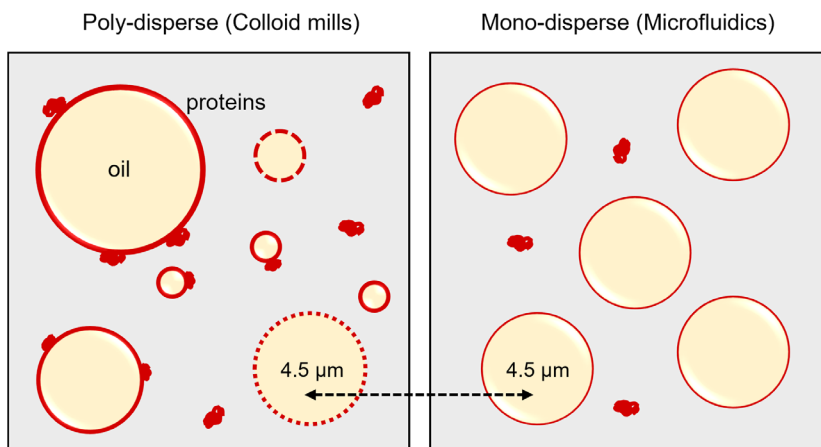**Figure 5.6**. Schematic overview of the findings in Chapter 5. Colloid mills and microfluidic emulsification result in poly- and mono-disperse emulsions. In polydisperse emulsions, droplets are heterogeneously covered with proteins. In monodisperse emulsions, the coverage is homogeneous. The black dashed line connects similar (4-5 μm) sized droplets that differ in surface coverage and protein and lipid oxidation behavior.

References

1. McClements, D. J. & Decker, E. A. Lipid oxidation in oil-in-water emulsions: Impact of molecular environment on chemical reactions in heterogeneous food systems. *J Food Sci* **65**, 1270–1282 (2000).
2. McClements, D. J. *Food emulsions: principles, practices, and techniques. CRC press* (2015).
3. Berton-Carabin, C. C., Ropers, M. H. & Genot, C. Lipid Oxidation in Oil-in-Water Emulsions: Involvement of the Interfacial Layer. *Compr Rev Food Sci Food Saf* **13**, 945–977 (2014).
4. Joint, F. A. O. Fats and fatty acids in human nutrition. Report of an expert consultation, 10-14 November 2008, Geneva. (2010).
5. Vannice, G. & Rasmussen, H. Position of the academy of nutrition and dietetics: dietary fatty acids for healthy adults. *J Acad Nutr Diet* **114**, 136–153 (2014).
6. Schaich, K. M. Challenges in elucidating lipid oxidation mechanisms: When, where, and how do products arise? in *Lipid oxidation* 1–52 (Elsevier, 2013).
7. Kerr, J. A. Bond dissociation energies by kinetic methods. *Chem Rev* **66**, 465–500 (1966).
8. Frankel, E. N. & Meyer, A. S. The problems of using one-dimensional methods to evaluate multifunctional food and biological antioxidants. *J Sci Food Agric* **80**, 1925–1941 (2000).
9. Abeyrathne, E. D. N. S., Nam, K. & Ahn, D. U. Analytical Methods for Lipid Oxidation and Antioxidant Capacity in Food Systems. *Antioxidants 2021, Vol. 10, Page 1587* **10**, 1587 (2021).
10. Zhang, Y. *et al.* Mechanism, indexes, methods, challenges, and perspectives of edible oil oxidation analysis. *https://doi.org/10.1080/10408398.2021.2009437* (2021).
11. Villeneuve, P. *et al.* Lipid oxidation in emulsions and bulk oils: a review of the importance of micelles. *Critical Reviews in Food Science and Nutrition* (2021).
12. Laguerre, M., Tenon, M., Bily, A. & Birtić, S. Toward a Spatiotemporal Model of Oxidation in Lipid Dispersions: a Hypothesis-Driven Review. *European Journal of Lipid Science and Technology* **122**, 1900209 (2020).
13. Li, P., McClements, D. J. & Decker, E. A. Application of flow cytometry as novel technology in studying the effect of droplet size on lipid oxidation in oil-in-water emulsions. *J Agric Food Chem* **68**, 567–573 (2019).
14. Li, P., McClements, D. J. & Decker, E. A. Application of flow cytometry as novel technology in studying lipid oxidation and mass transport phenomena in oil-in-water emulsions. *Food Chem* **315**, 126225 (2020).
15. Banerjee, C., Breitenbach, T. & Ogilby, P. R. Spatially resolved experiments to monitor the singlet oxygen initiated oxidation of lipid droplets in emulsions. *ChemPhotoChem* **2**, 586–595 (2018).
16. Yang, S., Verhoeff, A. A., Merkx, D. W. H., van Duynhoven, J. P. M. & Hohlbein, J. Quantitative spatiotemporal mapping of lipid and protein oxidation in mayonnaise. *Antioxidants* **9**, 1–13 (2020).
17. Boens, N., Leen, V. & Dehaen, W. Fluorescent indicators based on BODIPY. *This journal is Cite this: Chem. Soc. Rev* **41**, 1130–1172 (2012).
18. Banerjee, C., Breitenbach, T. & Ogilby, P. R. Spatially Resolved Experiments to Monitor the Singlet Oxygen Initiated Oxidation of Lipid Droplets in Emulsions. *ChemPhotoChem* **2**, 586–595 (2018).
19. Raudsepp, P., Brüggemann, D. A. & Andersen, M. L. Evidence for transfer of radicals between oil-in-water emulsion droplets as detected by the probe (E, E)-3, 5-bis (4-phenyl-1, 3-butadienyl)-4, 4-difluoro-4-bora-3a, 4a-diaza-s-indacene, BODIPY665/676. *J Agric Food Chem* **62**, 12428–12435 (2014).
20. Raudsepp, P., Brüggemann, D. A., Knudsen, J. C. & Andersen, M. L. Localized lipid autoxidation initiated by two-photon irradiation within single oil droplets in oil-in-water emulsions. *Food Chem* **199**, 760–767 (2016).
21. ten Klooster, S., Schroën, K. & Berton-Carabin, C. Lipid oxidation products in model food emulsions: do they stay in or leave droplets, that's the question. *Food Chem* 134992 (2022).
22. Berton, C., Genot, C. & Ropers, M. Journal of Colloid and Interface Science Quantification of unadsorbed protein and surfactant emulsifiers in oil-in-water emulsions. *J Colloid Interface Sci* **354**, 739–748 (2011).
23. ten Klooster, S., Berton-Carabin, C. & Schroën, K. Design insights for upscaling spontaneous microfluidic emulsification devices based on behavior of the Upscaled Partitioned EDGE device. *Food Research International* 112365 (2022).
24. Cuvelier, M.-E., Soto, P., Courtois, F., Broyart, B. & Bonazzi, C. Oxygen solubility measured in aqueous or oily media by a method using a non-invasive sensor. *Food Control* **73**, 1466–1473 (2017).
25. Truesdale, G. A., Downing, A. L. & Lowden, G. F. The solubility of oxygen in pure water and sea-water. *Journal of Applied Chemistry* **5**, 53–62 (1955).
26. Srinivasan, S., Xiong, Y. L. & Decker, E. A. Inhibition of protein and lipid oxidation in beef heart surimi-like material by antioxidants and combinations of pH, NaCl, and buffer type in the washing media. *J Agric Food Chem* **44**, 119–125 (1996).
27. Shantha, N. C. & Decker, E. A. Rapid, sensitive, iron-based spectrophotometric methods for determination of peroxide values of food lipids. *J AOAC Int* **77**, 421–424 (1994).

28. Ten Klooster, S. *et al.* Alkyl chain length modulates antioxidant activity of gallic acid esters in spray-dried emulsions. *Food Chem* **387**, 132880 (2022).

29. Merkx, D. W. H., Hong, G. T. S., Ermacora, A. & Van Duynhoven, J. P. M. Rapid Quantitative Profiling of Lipid Oxidation Products in a Food Emulsion by 1H NMR. *Anal Chem* **90**, 4863–4870 (2018).

30. Schmidt, U., Weigert, M., Broaddus, C. & Myers, G. *Cell detection with star-convex polygons. Lecture Notes in Computer Science* vol. 11071 LNCS (2018).

31. Jacobs, N. J. & Vandenmark, P. J. Colorimetric method for determination of triglycsrides. *Arch Biochem. Biophys* **88**, 250–255 (1960).

32. Trinder, P. Quantitative determination of triglyceride using GPO-PAP method. *Ann Biochem* **6**, 24–27 (1969).

33. Schroën, K. & Berton-Carabin, C. C. A unifying approach to lipid oxidation in emulsions: Modelling and experimental validation. *Food Research International* **160**, (2022).

34. Schaich, K. M. Lipid Oxidation: New Perspectives on an Old Reaction. *Bailey's Industrial Oil and Fat Products* 1–72 (2020).

35. Muñoz-Tamayo, R. *et al.* Hydrolysis of β-casein by the cell-envelope-located PI-type protease of Lactococcus lactis: A modelling approach. *Int Dairy J* **21**, 755–762 (2011).

36. Yoshida, Y., Shimakawa, S., Itoh, N. & Niki, E. Action of DCFH and BODIPY as a probe for radical oxidation in hydrophilic and lipophilic domain. *Free Radic Res* **37**, 861–872 (2003).

37. Takahashi, A. *et al.* Kinetic Analysis of Co-oxidation of Biomembrane Lipids Induced by Water-Soluble Radicals. *JAOCS, Journal of the American Oil Chemists' Society* **93**, 803–811 (2016).

38. van Boekel, M. A. J. S. Kinetic Modeling of Reactions In Foods. *Kinetic Modeling of Reactions In Foods* (2008).

39. Naguib, Y. M. A. Antioxidant activities of astaxanthin and related carotenoids. *J Agric Food Chem* **48**, 1150–1154 (2000).

40. Raudsepp, P., Brüggemann, D. A. & Andersen, M. L. Detection of radicals in single droplets of oil-in-water emulsions with the lipophilic fluorescent probe BODIPY665/676 and confocal laser scanning microscopy. *Free Radic Biol Med* **70**, 233–240 (2014).

41. Drummen, G. P. C., Gadella, B. M., Post, J. A. & Brouwers, J. F. Mass spectrometric characterization of the oxidation of the fluorescent lipid peroxidation reporter molecule C11-BODIPY581/591. *Free Radic Biol Med* **36**, 1635–1644 (2004).

42. Shao, X. *et al.* Highly selective and sensitive 1-amino BODIPY-based red fluorescent probe for thiophenols with high off-to-on contrast ratio. *Anal Chem* **87**, 399–405 (2015).

43. Berton, C., Ropers, M.-H., Viau, M. & Genot, C. Contribution of the interfacial layer to the protection of emulsified lipids against oxidation. *J Agric Food Chem* **59**, 5052–5061 (2011).

44. Klooster, S. ten, Schroën, K. & Berton-Carabin, C. Lipid oxidation products in model food emulsions: do they stay in or leave droplets, that's the question. *Food Chem* **405**, (2023).

45. Hohlbein, J. Single-molecule localization microscopy as an emerging tool to probe multiscale food structures. *Food Structure* **30**, 100236 (2021).

46. Hebishy, E., Buffa, M., Guamis, B., Blasco-Moreno, A. & Trujillo, A. J. Physical and oxidative stability of whey protein oil-in-water emulsions produced by conventional and ultra high-pressure homogenization: Effects of pressure and protein concentration on emulsion characteristics. *Innovative Food Science and Emerging Technologies* **32**, 79–90 (2015).

47. Berton, C., Ropers, M. H., Guibert, D., Solé, V. & Genot, C. Modifications of interfacial proteins in oil-in-water emulsions prior to and during lipid oxidation. *J Agric Food Chem* **60**, 8659–8671 (2012).

48. Yang, S., Takeuchi, M., Friedrich, H., van Duynhoven, J. P. M. & Hohlbein, J. Unravelling mechanisms of protein and lipid oxidation in mayonnaise at multiple length scales. *Food Chem* **402**, 134417 (2023).

49. Neves, M. A., Wang, Z., Kobayashi, I. & Nakajima, M. Assessment of Oxidative Stability in Fish Oil-in-Water Emulsions: Effect of Emulsification Process, Droplet Size and Storage Temperature. *J Food Process Eng* **40**, e12316 (2017).

50. Atarés, L., Marshall, L. J., Akhtar, M. & Murray, B. S. Structure and oxidative stability of oil in water emulsions as affected by rutin and homogenization procedure. *Food Chem* **134**, 1418–1424 (2012).

51. Takahashi, A., Takahashi, R., Hiromori, K. & Shibasaki-Kitakawa, N. Quantitative Evaluation of Oxidative Stability of Biomembrane Lipids in the Presence of Vitamin E. *J Am Oil Chem Soc* **98**, 567–579 (2021).

52. Rojas Wahl, R. U., Zeng, L., Madison, S. A., DePinto, R. L. & Shay, B. J. Mechanistic studies on the decomposition of water soluble azo-radical-initiators. *Journal of the Chemical Society, Perkin Transactions 2* 2009–2018 (1998).

53. Niki, E. Role of vitamin e as a lipid-soluble peroxyl radical scavenger: In vitro and in vivo evidence. *Free Radic Biol Med* **66**, 3–12 (2014).

54. Napolitano, G., Fasciolo, G., Meo, S. Di & Venditti, P. Vitamin E Supplementation and Mitochondria in Experimental and Functional Hyperthyroidism: A Mini-Review. (2019).

55. Decker, E. A. & Hultin, H. O. Lipid Oxidation in Muscle Foods via Redox Iron. 33–54 (1992).

56.   Babbs, C. F. & Steiner, M. G. Simulation of free radical reactions in biology and medicine: A new two-compartment kinetic model of intracellular lipid peroxidation. *Free Radic Biol Med* **8**, 471–485 (1990).
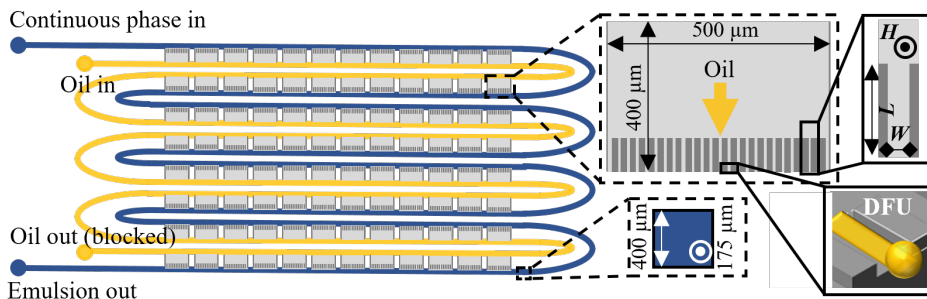
5

5.5   Appendix

Figure S5.1. Top-view design of the Upscaled Partitioned EDGE chips used in this research to generate monodisperse droplet emulsions. The blue 'twisted road' channel represents the continuous aqueous-phase channel. The yellow 'twisted road' channel represents the to-be-dispersed oil-phase channel. The gray rectangular areas between these channels are the main plateaus containing 24 micro-plateaus of 50 x 10 x 1 μm (L x W x H) with the droplet formation units (DFU). A 3D representation of a DFU is shown in the right lower corner, showing oil – in yellow – being pushed out of the DFU and forming a droplet ready to detach. This illustration is not to scale; only 12 out of the 42 main plateaus are shown per row.
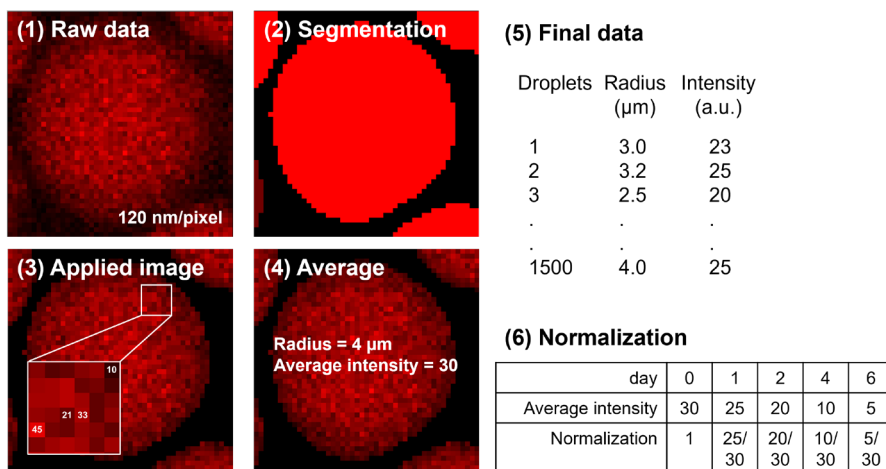

Figure S5.2. Data analysis pathway of microscopy images. (**1**) Raw image data (excited at 640 nm) were acquired using CLSM as described in the main text (**section 5.2.4**). The pixel size was 120 nm (512 x 512 pixels providing a 61.4 x 61.4 μm wide field of view). (**2**) The segmentation masks of oil droplets were acquired by applying 2D StarDist to the sum of the green and red detection channels (ex 561 + ex 640 nm). (**3**) Then, masks and raw data were multiplied using MATLAB. (**4**) The average intensity of each droplet was used for further analyses, and the radius of the droplet was calculated from the number of pixels with the assumption of circle shape; r (radius, μm) = $0.12 \cdot \sqrt{(\text{Sum of pixel numbers} / \pi)}$, 1 pixel = 0.12 μm. (**5**) Finally, we obtained a list of droplet numbers and radii with the average intensity per droplet. (**6**) To compare data obtained under different conditions over different days, the initial intensity was set to 1, and all other data points were divided by the average intensity of all droplets at day 0.

Table S5.1: Kinetic rates of lipid oxidation reactions in the O/W emulsions with the presence of AAPH and BODIPY

$\dfrac{d[L*]}{dt} = k_1[LH] - k_2[L^\cdot][O2] + k_3[LOO^\cdot][LH] + k_5[OH^\cdot][LH] + k_6[LO^\cdot][LH] + k_7[LO^\cdot][LH]$ $+ k_{AAPH}[AAPH]$	eq.S1
$\dfrac{d[LH]}{dt} = -k_1[LH] - k_3[LOO^\cdot][LH] - k_5[OH^\cdot][LH] - k_6[LO^\cdot][LH] - k_7[LO^\cdot][LH]$	eq.S2
$\dfrac{d[LOO^\cdot]}{dt} = k_2[L^\cdot][O2] - k_3[LOO^\cdot][LH] - k_{BODIPY}[LOO^\cdot][BODIPY]$	eq.S3
$\dfrac{d[O2]}{dt} = -k_2[L^\cdot][O2]$	eq.S4
$\dfrac{d[LO^\cdot]}{dt} = k_4[LOOH] - k_6[LO^\cdot][LH] - k_7[LO^\cdot][LH]$	eq.S5
$\dfrac{d[LOOH]}{dt} = k_3[LOO^\cdot][LH] - k_4[LOOH]$	eq.S6
$\dfrac{d[AD]}{dt} = k_6[LO^\cdot][LH]$	eq.S7
$\dfrac{d[EP]}{dt} = k_7[LO^\cdot][LH]$	eq.S8
$\dfrac{d[AAPH]}{dt} = -k_{AAPH}[AAPH]$	eq.S9
$\dfrac{d[BODIPY]}{dt} = -k_{BODIPY}[LOO^\cdot][BODIPY]$	eq.S10
$\dfrac{d[OH^\cdot]}{dt} = k_4[LOOH] - k_5[OH^\cdot][LH]$	eq.S11

Table S5.2: Estimated values and literature values of model kinetic constants at 25 °C

Parameters	Estimated values[1]	Lower and upper bounds of starting values[2]	Literature values
k_1 (s^{-1})	2.09×10^{-8}	$[10^{-15}, 10^{-5}]$	~10^{-15} [51,52]
k_2 (mol^{-1}.m^3.s^{-1})	1.026×10^{-7}	$[10^{-15}, 100]$	100 at 37°C [53]
k_3 (mol^{-1}.m^3.s^{-1})	3.04×10^{-7}	$[10^{-15}, 10^{-3}]$	10^{-4} to 10^{-3} at 40°C [52,54]
k_4 (s^{-1})	2.7×10^{-6}	$[10^{-15}, 10^{-2}]$	10^{-3}
k_5 (mol^{-1}.m^3.s^{-1})	5×10^{-6}	$[10^{-15}, 10^3]$	--
k_6 (mol^{-1}.m^3.s^{-1})	10^2	$[10^{-5}, 10^3]$	10^{-5} to 10^{-2} at 20°C [55]
k_7 (mol^{-1}.m^3.s^{-1})	0.3	$[10^{-5}, 10]$	0.032 to 3.3 [55]
k_{AAPH} (s^{-1})	7.5×10^{-10}	$[7.5 \times 10^{-10}]$	10^{-6} to 10^{-7} [52]
k_{BODIPY} (mol^{-1}.m^3.s^{-1})	6.08×10^{-7}	$[2 \times 10^{-15}, 2 \times 10^{-3}]$	$2 \times k_3$ [36] or 6×10^{-3} M^{-1}s^{-1} at 37 °C [3]
Initial concentration of lipid radicals (mol/m^3 oil)	10^{-11}	$[10^{-15}, 10^{-9}]$	2×10^{-9} (L*), 10^{-10} (LOO*), 7×10^{-15} (OH*) [56]

[1]The deviations of the estimated values < 1% from 200 iteration Monte Carlo simulations, indicating that the optimization is robust enough for the estimation of the kinetic constants and initial radical concentrations; [2]We cut off the upper bound of starting values if their excess values return significantly higher residuals than the previous fitting tests. [3]As far as we know, there is only one report about the kinetic constant of another BODIPY type (BODIPY 581/591 C11), but not BODIPY 665/676.

5.5.1   Partition coefficients of O_2/AAPH/BODIPY between the aqueous and oil phases.

The changes in O_2, AAPH, and BODIPY from different droplet sizes are quantitatively considered in K as a partition coefficient that depends on droplet sizes. For instance, the concentration of O_2 at the oil/water interface in accordance with changes in droplet sizes was calculated (eq.S12).

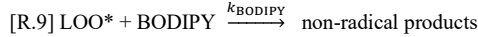$$[O_2]_O = K\frac{V_W}{V_O}[O_2]_W = K\frac{V_W}{V_O(D_{3,2})}[O_2]_W \qquad\qquad \text{eq.S12}$$

$$[\widetilde{O}_2]_O = K\frac{V_W}{V_O(\widetilde{D}_{3,2})}[O_2]_W \text{ where } \widetilde{D}_{3,2} = D_{3,2} \pm \sigma \qquad\qquad \text{eq.S13}$$

$$\frac{[\widetilde{O}_2]_O}{[O_2]_O} = \frac{V_O(D_{3,2})}{V_O(\widetilde{D}_{3,2})} = \frac{D_{3,2}}{\widetilde{D}_{3,2}} = K_{3,2} \qquad\qquad \text{eq.S14}$$

where $[O_2]_W$ and $[O_2]_O$ indicate the concentrations of O_2 in the water and oil phases, respectively; V_W and V_O are the volume of water and oil phases.

5.5.2   Kinetic rate and kinetic constants

From **Table 5.1**, the reactions for LOO* with LH or BODIPY 665/676 over time can be described as,

$$[\text{R.3}] \text{ LOO* + LH } \xrightarrow{k_3} \text{ LOOH + L*}$$

$$[\text{R.9}] \text{ LOO* + BODIPY } \xrightarrow{k_{\text{BODIPY}}} \text{ non-radical products}$$

where k_{BODIPY} and k_3 are kinetic constants. The kinetic rates for LOO* to react with LH or BODIPY 665/676 over time corresponding to R.3 and R.9 can be expressed as r_{LOO*}^{R3} and r_{LOO*}^{R9}, respectively,

$$r_{LOO*}^{R3} = k_3 \times [\text{LOO*}][\text{LH}]$$

$$r_{LOO*}^{R9} = k_{BODIPY} \times [\text{LOO*}][\text{BODIPY}]$$

Although k_{BODIPY} is two times higher than k_3 (**Table S5.2**), the kinetic model showed that the kinetic rate r_{LOO*}^{R9} is 4.5×10^7 times lower than r_{LOO*}^{R3} due to the high initial concentration of LH.

BODIPY 665/676

Reaction with LOO *

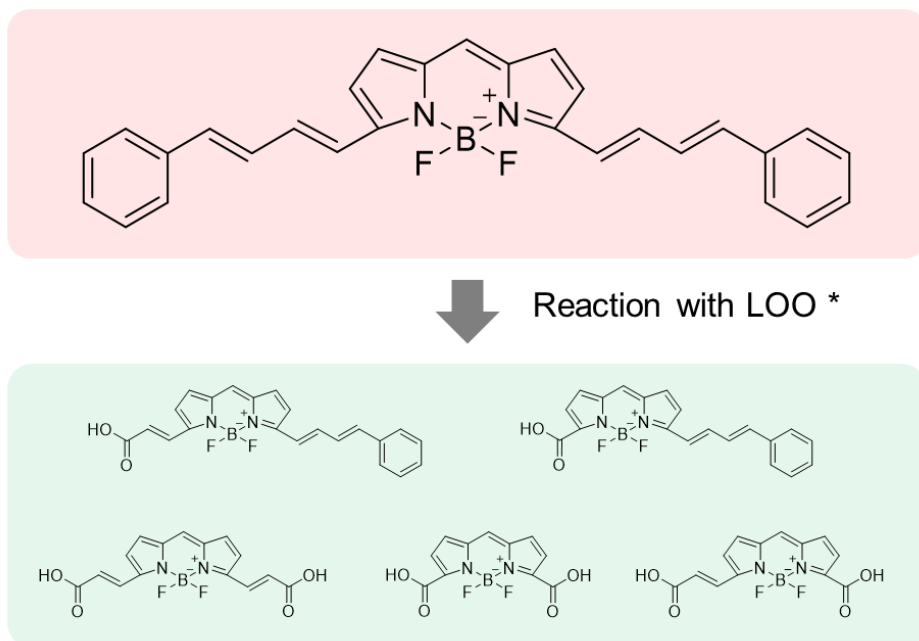**Figure S5.3**. The non-oxidized structure and possible modified structures of BODIPY 665/676.
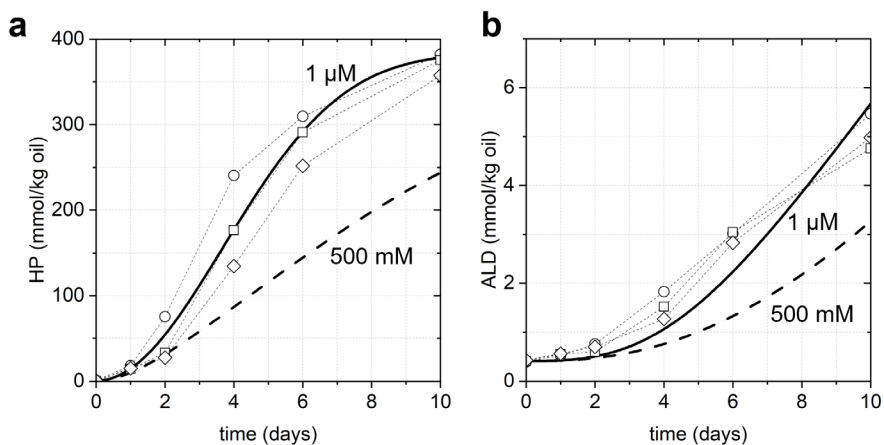
5

Figure S5.4. The formation of lipid oxidation products at various concentrations of BODIPY 665/676. Comparison between the simulations of hydroperoxides (**a**) and aldehydes (**b**) concentrations over time with 0, 1, and 50 µM (all three in overlapping solid black lines) and with 500 mM (dashed lines) of BODIPY 665/676.
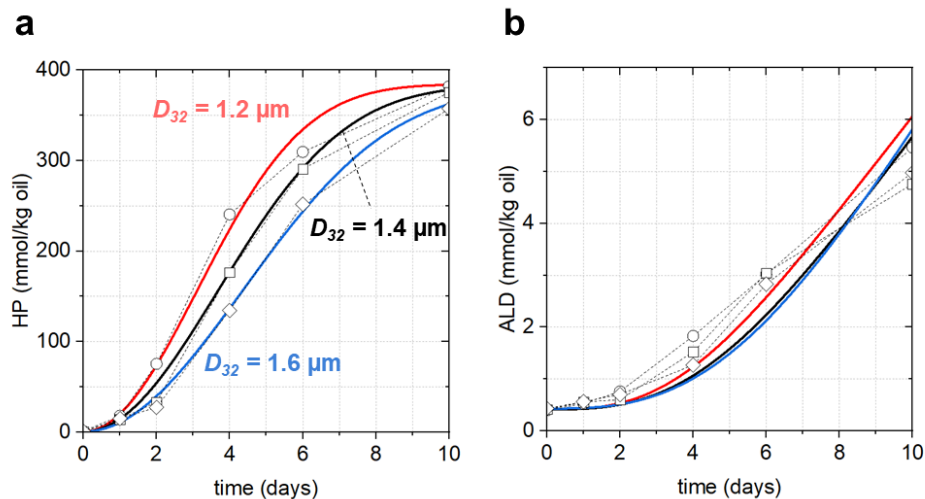
Figure S5.5. Effect of the droplet sizes (D_{32}) with the deviations ($\pm$ 0.2 μm) on the formation of hydroperoxides (**a**) and aldehydes (**b**) over incubation in colloid mill-made emulsions stabilized by 2 wt% WPI. The concentration of BODIPY 665/676 was fixed at 1 μM, and only droplet sizes (D_{32}) were varied. Red, black, and blue solid lines show the simulation results from different droplet sizes, respectively, for 1.2, 1.4, and 1.6 μm. The experimental data set (from **Figure 5.2**) is included for the comparison. We attribute the difference in the formation of lipid oxidation products between 0, 1, and 50 μM BODIPY 665/676 emulsions to the small droplet size difference from the separate emulsification steps.
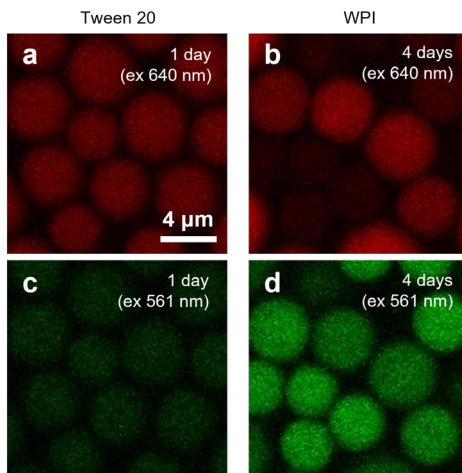
Figure S5.6. Combined channel images of non-oxidized (ex 640 nm) and oxidized (ex 561 nm) BODIPY 665/676 in Tween 20- and WPI-stabilized emulsions. Tween 20-stabilized emulsions showed the decrease of BODIPY 665/676 excited at 640 nm, whereas they did not show an increase in channel representing oxidized BODIPY excited at 561 nm. In contrast, both the decrease in native fluorescence and the increase in oxidized BODIPY 665/676 were observed in WPI-stabilized emulsions.

a

b
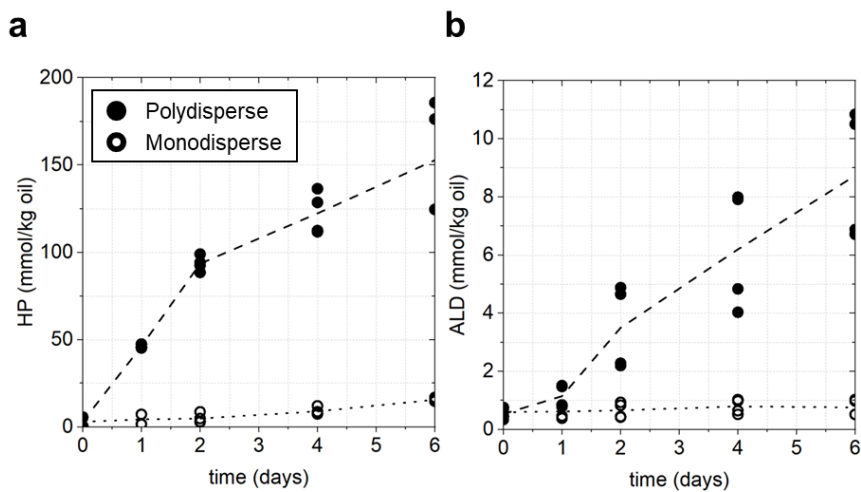
Figure S5.7. Lipid oxidation in Tween 20-stabilized emulsions. The formation of hydroperoxides (**a**) and aldehydes (**b**) in the colloid mill-made polydisperse emulsions stabilized by Tween 20 proceeded faster than in monodisperse emulsions made with microfluidic devices. The difference in droplet sizes caused this faster oxidation in polydisperse emulsions, as we described in **Figure 5.1**.

6

Adapting cryogenic correlative light and electron microscopy (cryo-CLEM) for food oxidation studies

Suyeon Yang*, Machi Takeuchi*, Rick Joosten, Heiner Friedrich, John P.M. van Duynhoven, Johannes Hohlbein

* These authors contributed equally

Abstract

Lipid oxidation is a major cause of product deterioration in oil-in-water food emulsions. Protein emulsifiers that are used to stabilize oil-in-water emulsions are known to delay or promote lipid oxidation. However, the impact of these protein emulsifiers at the interface on lipid oxidation is currently unknown, and the mechanism of lipid-protein co-oxidation is unclear. In this study, we developed a cryo-correlative light and electron microscopy (cryo-CLEM) platform for co-localizing the oxidation of lipids and proteins at the interface in food emulsions. We showed that lipid oxidation in food emulsions could be observed at cryogenic temperature using fluorescence imaging of the fluorophore BODIPY 665/676 that we employed earlier as a lipid oxidation sensor at room temperature. Using cryo-transmission electron microscopy (cryo-TEM), we observed that more protein aggregates are found at the droplet interfaces in oxidized emulsions compared to fresh ones. Our cryo-CLEM platform paves the way for future cryo-correlative oxidation studies to localize protein and lipid oxidation events using fluorescence microscopy and correlate these with the high-resolution interfacial structure provided by electron microscopy.

6.1   Introduction

Many food products such as mayonnaise, salad dressings, and yogurt are oil-in-water (O/W) emulsions, which are commonly stabilized with emulsifiers consisting of proteins and amphiphilic lipid surfactants[1]. In O/W food emulsions, lipid oxidation is widely considered a key factor for food deterioration[2], but the role of the emulsifiers at the interface is poorly understood, even though lipid oxidation is initiated there[3]. Specifically, it is currently unclear what the exact role of proteins at the interface on lipid oxidation is[3–5]. Whereas some earlier work showed that protein-stabilized interfaces are less efficient at protecting emulsified lipids against oxidation than those stabilized with low-molecular weight surfactants[5], other studies indicated that proteins at the interface play the role of antioxidants[6,7]. Therefore, understanding lipid-protein co-oxidation at the interface is essential for addressing food deterioration. However, not many studies have addressed this so far due to a lack of methods that can co-localize lipid oxidation and proteins at the interface.

To address this methodology gap, we adapted a cryogenic correlative light and electron microscopy (cryo-CLEM) platform for studying oxidation in food emulsions. CLEM is an emerging technique that combines information from fluorescence and electron microscopy of the same regions within a sample[8–12]. This technique has been developed and applied mainly in life science over the past decade[13,14]. In the biomedical field, the correlative combination of light and electron microscopy has been used to correlate nanoscale structural information with the localization of fluorophore-labeled biomolecules. For performing electron microscopy at ambient conditions, CLEM typically requires laborious chemical samples preparation steps such as fixation, staining, resin embedding, and cutting, which can lead to artifacts[15–17]. This can be circumvented by performing cryo-electron microscopy[18,19] as cryogenic sample preparation, such as plunge vitrification[18] or high-pressure freezing[19], does not require any addition of chemicals for fixation. Moreover, it has been reported that cryo-fixated samples better preserve structure compared to chemical-fixated samples[16,19,20].

Cryogenic conditions are specifically helpful for application to food emulsions as they prevent the diffusion of components and further oxidation during measurements. However, cryo-CLEM has not yet been explored in food systems. The length scales covered by CLEM have the potential to provide insights into the relationship between the (co-) oxidation of lipids and proteins at droplet interfaces and the local nanoscale arrangement of proteins. In **Chapter 4**, we showed aggregation of proteins in the continuous phase separated from mayonnaise using localization of fluorescently labeled spin-trap and autofluorescence by confocal microscopy and cryo-transmission electron microscopy (cryo-TEM)[21]. We could observe aggregation of proteins in the aqueous phase upon oxidation, but confocal microscopy and cryo-TEM were not deployed in correlative mode. For instance, the same samples were taken for both confocal microscopy

and cryo-TEM measurements, but imaging was not performed at the same position in the sample. Following our previous work, we aim to image proteins and their aggregates at the oil droplet interface in cryo-TEM and the lipid oxidation of the same oil droplets in cryo-fluorescence microscopy.

Here, we first introduce a home-built cryo-upright fluorescence microscope (cryo-FM) for correlative imaging and test the setup with fluorescent silica beads. Then we demonstrate the fluorescence detection of an oxidation-sensitive dye, BODIPY 665/676, in egg yolk stabilized model emulsions at cryogenic temperature (77 K). Additionally, protein granules at the oil droplet interfaces of fresh and oxidized emulsions were observed using cryo-TEM. Finally, our work demonstrates the feasibility of using cryo-CLEM to unravel the role of colloidal interfacial structure in mediating lipid oxidation of food emulsions by correlating images from cryo-FM and cryo-TEM.

6.2   Materials and methods

6.2.1   Materials

Soybean oil and egg yolk containing 8% (w/w) NaCl were purchased from a local store. The lipophilic oxidation-sensitive dye BODIPY 665/676 and Cy3 dye were purchased from Thermo Fischer (Waltham, MA, USA). Alumina power (Alumina N—Super I) was obtained from MP EcoChrom (Eschwege, Germany). Fluorescent silica beads with a diameter of 200 and 780 nm were purchased from ThermoFisher Scientific (Eugene, Oregon, USA) and Bangs Laboratories, Inc (Indiana, USA), respectively. Sodium acetate (MW: 82.03 g/mol), Acetic Acid (MW: 60.05 g/mol), and 2,2'-Azobis (2-amidinopropane) dihydrochloride (AAPH) were purchased from Sigma-Aldrich (Zwijndrecht, the Netherlands). Ultrapure water (18.2 MΩ) was used and prepared using a Milli-Q system (Millipore Corporation, Billerica, MA, USA). Dimethyl sulfoxide (DMSO) was purchased from Thermo Fischer (Waltham, MA, USA).

6.2.2   Preparation of emulsions

0.05 M of acetate buffer (pH 3.8) was prepared with sodium acetate (0.6 g) and acetic acid (2.6 g) in 1 L of ultrapure water. For the preparation of the continuous phase, egg yolk was mixed in the buffer with a concentration of 1 wt.%. Stripped soybean oil was prepared using alumina powder to remove impurities and lipid-soluble antioxidants[22]. Briefly, the oil was mixed with the powder at a volume ratio of 2:1 in Falcon tubes and shaken for 24 hrs. The suspension was then centrifuged at 2000×g for 20 min. The oil was collected, and the same centrifugation procedure was repeated to ensure the complete removal of the alumina powder. For fluorescence labeling of lipid droplets as a marker for cryo-fluorescence microscopy, 50 µM of BODIPY 665/676 was pre-mixed in the stripped soybean oil before making emulsions. A coarse emulsion

was first prepared by adding 10 wt.% of stripped soybean oil to the continuous phase, and high-speed stirring was applied at 11,000 rpm for 1 min with a rotor-stator homogenizer (Ultra-turrax IKA T18 basic, Germany). Next, a fine emulsion was prepared by passing the coarse emulsion through either (1) a lab-scale colloid mill with a gap width of 0.32 mm (IKA Magic Lab, Staufen, Germany), operating for 1 min at 26,000 rpm or (2) a microfluidizer (Microfluidics, Massachusetts, USA), equipped with a Y-shaped interaction chamber (F12Y; minimum internal dimension: 75 μm), operating at 600 bars during three passes. During the operation, the colloid mill was cooled with water at 4 °C, and for the microfluidizer, the sample chamber was placed in an ice bath.

6.2.3   Cryo sample preparation

Cryo-samples were prepared as follows: (i) Prior to the application of the sample, TEM grids were first glow-discharged to make the surface of the carbon TEM support film hydrophilic using plasma treatment. Two different TEM grids were used in the experiments; either a 200 mesh Cu TEM grid with a R2/2 Quantifoil® carbon support film (Quantifoil MicroTools GmbH) or a 200 mesh Au TEM finder grid with a R2/2 Quantifoil® carbon support film (LFH2100AR2, AURION). (ii) Samples of either the fluorescent beads or emulsions were first diluted with the buffer for clearer transparency and sectioning for cryo-TEM imaging, and 3 μL of the diluted samples were applied on TEM grids in an automated vitrification robot (Thermo Fisher Scientific Vitrobot™ Mark IV). Then, the samples were blotted with the condition of blotting time (3 s) and blot force (-4) and plunged into liquid ethane.

6.2.4   Optical setup of cryo-FM and cryo-TEM

For cryo-FM measurements, a cryo-stage was purchased from LINKAM (CMS196M, UK), and a laser was obtained from Integrated Optics (MatchBox, 405, 520, and 638 nm, Lithuania). A square-core multimode fiber (0.39 NA, 150 x 150 μm square core), an iris (SM1D12D), a lens for the collimation (f = 50 mm, AC254-050-A), mirrors (BBE1-E02), a second lens (f = 250 mm, AC254-250-A), a dichroic mirror holder (DMF1/M), motorized Translation Stage for z-focusing (KMTS25E/M), and a tube lens (f = 200 mm, ITL 200) were all purchased from Thorlabs (Germany). A dichroic mirror (ZT532/640rpc-UF2) and a bandpass filter (ZET532/640m-TRF) were obtained from Chroma (USA). The objective lens (100 X, NA 0.90, WD 2.0 mm, MUC11900) was purchased from Nikon (Japan), and the camera (UI-3060CP-M-GL R2) from IDS (Germany).

Cryo-TEM imaging was conducted on a CryoTitan (Thermo Fisher Scientific), which was operated at 300 kV and is equipped with a Field-Emission Gun, a post-GIF 2k × 2k Gatan CCD camera (model 794), and a post-column Gatan Energy Filter (GIF, model 2002).
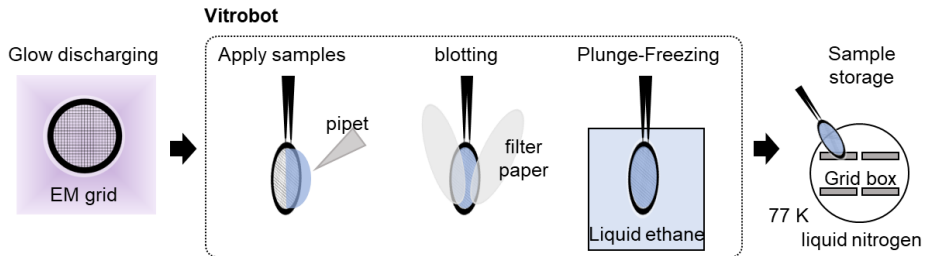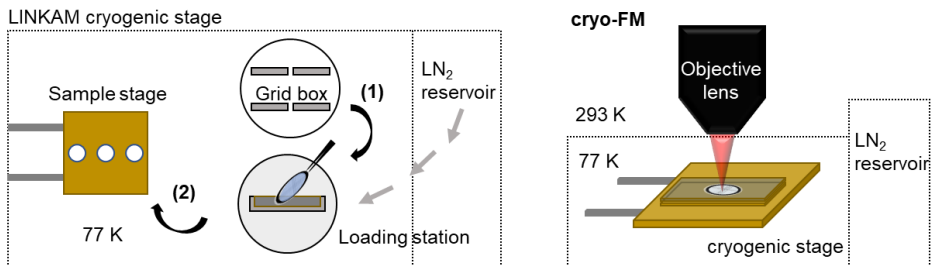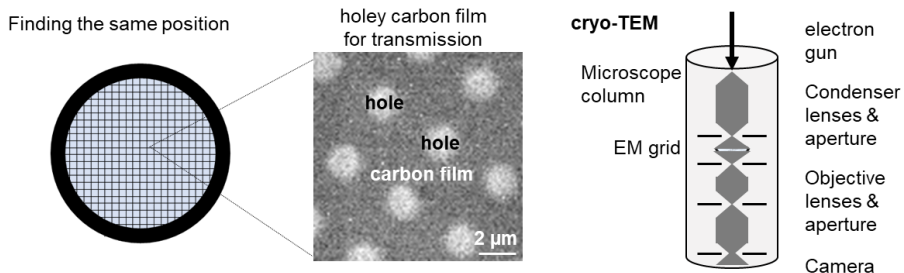
a cryo-sample preparation

b cryo-FM

c cryo-TEM

Figure 6.1. The general framework of cryogenic correlative light and electron microscopy (cryo-CLEM). (**a**) Fluorescence-labeled samples were first diluted and vitrified using plunge vitrification. Prior to the vitrification, the EM grid is first glow-discharged using plasma to make the hydrophobic surface. Then the diluted sample was applied, blotted with the filter paper, and plunged into liquid ethane. These steps were conducted using a Vitrobot (**section 6.2.3**). The vitrified samples were stored in the grid box at 77 K in liquid nitrogen before the cryo-FM measurements. (**b**) The cryo-sample is loaded and kept at the cryogenic temperature using the LINKAM stage during cryo-FM measurements. After fluorescence imaging at 77 K, sample positions are mapped to retrieve the same position in cryo-TEM later. (**c**) The cryo-sample is loaded in cryo-TEM, and high-resolution images of the targeted area are obtained. To achieve better contrast, holey carbon film was used. In cryo-TEM, accelerated electrons first pass the three sets of electromagnetic lenses. Then the transmitted signals of the sample are obtained.

6.3 Result and Discussion

6.3.1 Design of the correlative cryo-FM and cryo-TEM platform

For correlative imaging of cryogenic fluorescence microscopy (cryo-FM) and cryogenic transmission electron microscopy (cryo-TEM), we developed the following workflow (**Figure 6.1**). First, we prepared the vitrified samples described in **section 6.2.3** (**Figure 6.1a**). Then, we transferred the vitrified specimen to the LINKAM cryo-stage and obtained cryo-FM images (**Figure 6.1b**). The sample loading step is conducted in the LINKAM cryo-stage, from a grid box to the loading station, then to the sample stage. The EM grid is inserted into the sample magnet clamp in the loading station, which is then loaded on the sample stage. The liquid nitrogen (LN_2) reservoir is connected to the stage, keeping the temperature of the sample stage at 77 K. A detailed explanation of the optical components of cryo-FM is described in **section 6.2.4,** and the optical setup will be elucidated in the next section. After the measurements in cryo-FM, we transferred the sample to cryo-TEM. Cryo-TEM is conducted on the same regions identified by cryo-FM. We used the holey carbon film to increase the contrast, and a brief explanation of cryo-TEM is described in **Figure 6.1c**. Accelerated electron beams travel through three sets of electromagnetic lenses, and the magnified image of a specimen is obtained[23].

6.3.2 Implementation of a cryogenic fluorescence microscopy (cryo-FM) platform

Standard fluorescence microscopy is often performed on inverted microscopes since this improves the stability of the optical setup and does not impose limitations on sample weight or height. Here, due to the need for liquid nitrogen to reach the cryogenic temperature, an upright configuration has been built up with a LINKAM cryo-stage (**Figure 6.2a**). The laser is coupled in a square-core multimode fiber to obtain a homogeneous intensity beam distribution. After this square-core multimode fiber, the Iris was placed to adjust the beam size. The laser beam is collimated with a lens and reflected by mirrors to an additional lens, which is inserted for beam expansion and wide-field imaging. Then, the laser beam is reflected via the dichroic mirror with the holder to the objective lens (100 X, NA 0.90, WD 2.0 mm). We choose an air-immersion objective lens minimizing heat transfer between the objective and the sample held at cryogenic temperatures, noting that a water or oil immersion objective lens would provide a higher numerical aperture (NA), resulting in better optical resolution. For a detailed explanation of NA, see **Chapter 2**. In our experiments, we selected the objective with a relatively high NA and a long working distance to reach the samples through the cryo-chamber (**Figure 6.2b**). Focusing along the Z direction is controlled by the motorized translation stage. The XY position is controlled by an internal motorized stage implemented in the LINKAM cryo-stage. The emission beam is collected with the same objective lens and passes through the dichroic mirror. A rubber tube needed to be inserted between the sample and the covering part of the objective

to minimize the temperature difference between the contact part with liquid nitrogen and the top side of the objective lens (**Figure 6.2c**). Without inserting this rubber tube, the objective lens's top side was fogged due to the temperature difference, which led to dimmed fluorescence signal over time in the detection path. Finally, the beam is focused onto an IDS camera using a tube lens.
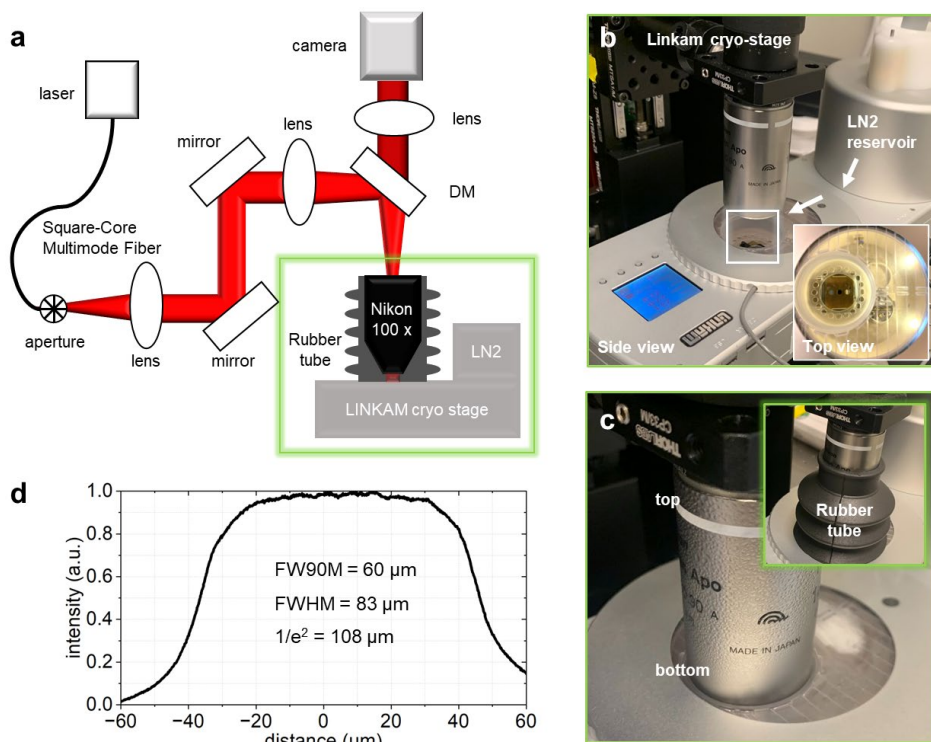

Figure 6.2. Optical setup of cryogenic fluorescence microscopy (cryo-FM). (**a**) Schematic representation of cryo-FM. The laser was coupled in a square-core multimode fiber, and the Iris was inserted after the fiber to adjust the beam size. Then the beam is collimated with the lens and reflected by mirrors to the additional lens inserted for beam expansion and wide-field imaging. The beam is reflected via a dichroic mirror to the objective lens and illuminates the samples. The signal from samples is collected with the same objective lens and passes through the dichroic mirror. Then the beam is focused onto the IDS camera using a tube lens. (**b**) The overview of the LINKAM cryo-stage and air type long-working distance (WD = 2.0 mm) objective lens. Dewar is filled with liquid nitrogen (LN$_2$) and supplies LN$_2$ to the sample stage. (**c**) The rubber tube was inserted to minimize the temperature difference between the contact part with liquid nitrogen (bottom) and the top side of the objective lens (top). (**d**) Homogeneous laser beam intensity distribution generated by a square-core multimode fiber. The beam distribution has 60 μm of full width at 90% of the maximum intensity (FW90M), which is smaller than the size of a single grid square.

For the measurements of the intensity beam distribution in the absence of the cryo-stage, we used a fluorescence dye (Cy3). 1 μM of fluorescence dye solution was dropped on a cover glass, and a second cover glass was placed on top of the dye solution. The solution was excited using

40 W/cm^2 laser intensity and 520 nm excitation. The uniform spatial distribution of the laser beam intensity was achieved by mode mixing in the fiber with a small coin motor. Our homogeneous beam distribution has a width of 60 µm at FW90M (full width at 90% of the maximum intensity) and 83 µm at FWHM (full width at half-maximum), thereby smaller than the size of a single grid square (**Figure 6.2d**). The 1/e^2 width is 108 µm, slightly larger than a single grid. The illumination area does not extend over the metal grid bar, ensuring that the beam effectively illuminates only a single grid square.

In cryo-FM, the laser illuminates the samples on an EM grid via the objective lens (**Figure 6.3a**). The EM grid is fixed in the metal grid holder connected to the metal bridge to maintain the cryogenic temperature. The EM grid consists of many grid squares (**Figure 6.3b**), covered with a carbon film that contains further holes where the samples are located (**Figure 6.3c**). The width and height of a single EM grid square is 90 µm, with the spacing of the metal grid being 30 µm wide. A side view of the EM grid shows the grid bar, the holey carbon film and the position of the vitreous ice layer containing the sample (**Figure 6.3d**). The laser beam is illuminated on the sample layer, where care should be exerted so that heat transfer does not cause local devitrification of samples.
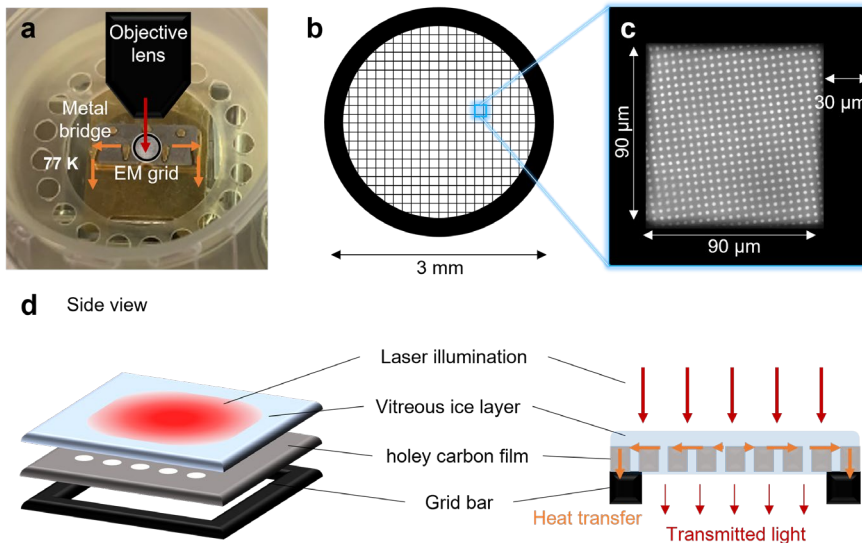
Figure 6.3. Description of EM grid and expected partial heat transfer from laser illumination to the sample and EM grid. (**a**) Picture of the EM grid with the metal grid holder on the metal bridge. The temperature of the samples during the measurements can be maintained at cryogenic temperature (77 K) because the metal bridge is connected to liquid nitrogen. (**b**) Schematic drawing of the EM grid which consists of many grid squares on the carbon film, has a diameter of 3 mm. (**c**) One square grid has multiple empty holes with a 2 µm-diameter. The size of single grid is 90 by 90 µm, and the width of a grid bar is 30 µm. (**d**) Side view of one square in an EM grid. The laser beam (red) illuminates the vitreous sample (light blue), which is placed on the holey carbon film (grey) that is located on the top of the grid bar (black). The expected partial heat transfer from the laser illumination (red) to the grid bar is schematically presented with orange arrows.

Based on the laser beam intensity distribution (**Figure 6.2d**), the expected heat transfer can be estimated. Here, we have a homogenous beam distribution which is convenient for estimating the total impact of heat on the samples. With a typical Gaussian beam profile, the region of high laser intensity is confined to the central area, which limits the field of view (FOV) to that area where fluorophores can be effectively illuminated. In contrast, with a homogeneous beam distribution, the laser intensity is uniform across the entire FOV, allowing for a larger area to be illuminated effectively. It was previously shown that high laser power could lead to the devitrification of the cryo samples[24–26]. The authors numerically calculated the expected temperature distribution using a finite element method (FEM)[27]. Together with the notion that devitrification of samples occurs at local temperatures above 136 K[18] the authors showed that devitrification for samples is more dependent on laser power than the illumination time. To prevent the devitrification of the ice layer and damage from the local heat induced by the laser, we experimentally determined the optimal condition for our cryo-upright microscopy setup (**Figure 6.4**). The cryo-prepared acetate buffer was illuminated at 638 nm excitation for 1 min at different laser intensities calculated using the FW90M area square shape of 60 by 60 µm. The occurrence of devitrification (cubic/hexagonal ice crystal formation) was examined in cryo-TEM to verify the maximum allowable laser intensity. Additionally, the damage in cryo-bright field microscopy with the internal LED lamp of the LINKAM cryo-stage was assessed before and after laser illumination.

After the 1 min illumination at 55 W/cm², the samples still had the vitreous ice layer intact (**Figure 6.4a**). There was no devitrification and structural damage visible in cryo-TEM. Also, no difference was found in cryo-bright field before and after the illumination. At 330 W/cm² laser illumination, devitrification of the ice layer was observed in cryo-TEM, indicated by contaminated ice crystal (**Figure 6.4b**). Also, in the cryo-bright field, we saw the disappearance of small particles, likely due to the local devitrification of the ice layer after laser illumination. Especially the damage on the edge of the laser spot was clearly visible. The spot size was approximately 60 by 60 µm, which matches the measured FW90M of 60 µm (**Figure 6.4b**). After the illumination with 1700 W/cm² for one minute, damage to the carbon films was seen, both in cryo-TEM and cryo-bright field microscopy (**Figure 6.4c**). Further experiments were therefore done under the vitreous condition (< 55 W/cm²) to prevent damage and devitrification of samples.
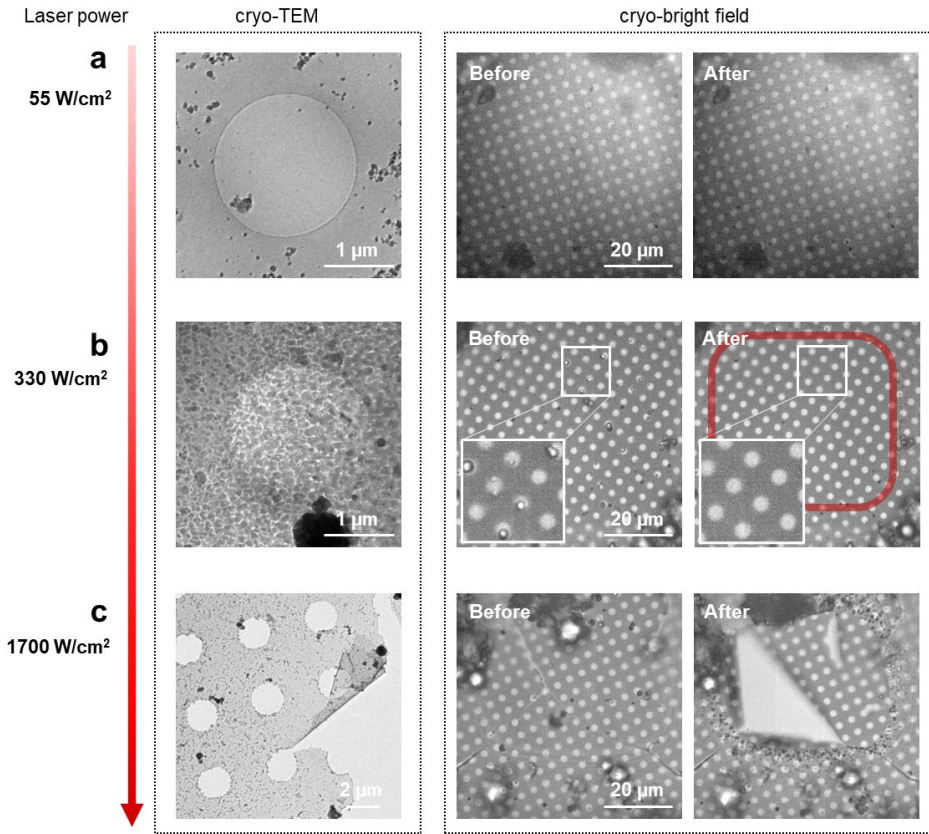
Figure 6.4. Optimization of the laser illumination intensity in cryo-FM. Acetate buffer (pH 3.8) is illuminated with a laser at 638 nm for 1 min. (**a**) Images of vitreous ice layer after the illumination with 55 W/cm^2. We found no signs of devitrification at high magnification in cryo-TEM and no visible damage to the ice layer in cryo-bright field microscopy (cryo-bright field) before and after laser illumination. (**b**) Images after the illumination with 330 W/cm^2. The devitrified ice layer is visible, indicated by contaminating ice crystals in cryo-TEM. In cryo-bright field, we noticed that the particles (see white boxes) moved away after the laser illumination. The red box indicates the damaged spot from the laser, approximately the same size as the measured FW90M (60 by 60 μm). (**c**) Damaged samples after the illumination with 1700 W/cm^2. The carbon film damage was clearly visible in cryo-TEM and cryo-bright field microscopy.

6.3.3   Fluorescence imaging at cryogenic temperature

Prior to the measurements of samples at 77 K, we first validated our microscopy setup by detecting fluorescence signals from fluorescently labeled beads of two different sizes (**Figure S6.1**). Fluorescent beads were prepared on the EM grid using plunge-freezing (**section 6.2.3**). We confirmed that both 780 nm and 200 nm-sized FL beads were detectable in our cryo-FM image when illuminated with 40 W/cm^2 at 520 nm laser excitation.

For fluorescence microscopy measurements at cryogenic temperature, it is required to carefully select fluorescent dyes as they can show different behaviors at temperatures lower than room temperature[24]. For instance, cryogenic temperatures can reduce the photo-bleaching of fluorophores due to the lack of diffusion of small reactive molecules such as oxygen and/or hamper transformational changes of fluorophores which are often considered crucial steps of photodecomposition[28].

We prepared a model food emulsion incorporating the oxidation-sensitive dye, BODIPY 665/676, which we used earlier for studying lipid oxidation in food emulsions[29]. BODIPY 665/676 shifts its emission wavelength from red to green upon reaction with lipid peroxyl radicals. As the dye has so far only been used at room temperature, its applicability for monitoring oxidation at cryogenic conditions (77 K) has to be proven. To test this, we prepared model system emulsions with a microfluidizer and performed cryo-sample preparation. The fresh and oxidized emulsions were illuminated at 638 nm with 14 W/cm^2 and 520 nm with 40 W/cm^2, respectively, to detect non-oxidized and oxidized lipid droplets. Oxidization was induced by incubating 1 mL of emulsions at 40 °C with 5 mM of the radical initiator (AAPH) in the dark over two days. First, we measured the non-induced samples without dilution to check the appearance of fluorescence from BODIPY 665/676 at 77 K.

In non-diluted emulsions, the packing of droplets is too dense to distinguish individual droplets (**Figures 6.5a & b**). However, we could see a general decrease in red fluorescence (excitation at 638 nm) and an increase in green fluorescence (excitation at 520 nm) of BODIPY 665/676 in oxidized emulsions at the cryogenic temperature. To observe the effect in individual droplets, we prepared tenfold diluted samples using the acetate buffer. Under the same laser excitation conditions, we could detect the BODIPY 665/676 signals in individual droplets with non-oxidized (ex 638 nm) and oxidized (ex 520 nm) channels in the fresh (**Figure 6.5c**) and oxidized emulsions (**Figure 6.5d**). The data shows that the shifted emission wavelength of BODIPY 665/676 upon oxidation can be measured not only at room temperature but also at cryogenic temperature. We note that droplet elongations originate from squeezing during the cryo-sample preparation due to the presence of droplets larger than 500 nm. This observation will be discussed in a later section.
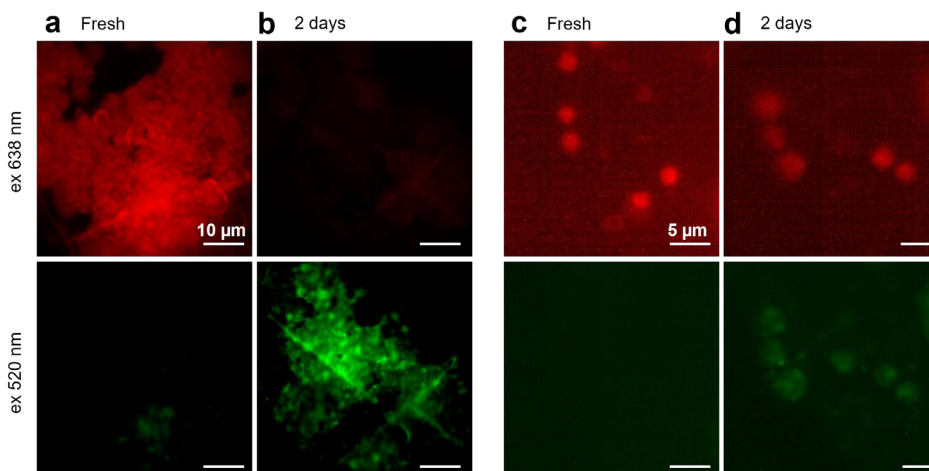
Figure 6.5. Detection of BODIPY 665/676 signals at cryogenic temperature (77 K) in non-diluted (**a-b**) and tenfold diluted emulsions (**c-d**). Samples are excited at 638 nm (14 W/cm^2) and 520 nm (40 W/cm^2) to detect non-oxidized and oxidized droplets. For obtaining oxidized emulsions, the samples were incubated at 40 °C over two days in the presence of 5 mM AAPH.

6.3.4   Interfaces of fresh and oxidized emulsions in cryo-TEM

In **Chapter 4**, we showed increasing protein aggregation upon oxidation in the continuous phase separated from whole emulsions[21]. Specifically, we observed oxidation of low-density lipoproteins (LDLs), which is the main ingredient of egg yolk, by confocal microscopy at μm-scale and cryo-TEM at nm-scale. Here, we want to understand (1) whether proteins at the interface also aggregate upon oxidation and (2) whether this protein aggregation at the interface reflects the lipid oxidation of droplets or follows an independent mechanism.

We first measured fresh and diluted emulsions in cryo-TEM (**Figure 6.6**). The oil droplets show a smooth surface with LDLs (with a diameter of ~ 40 nm)[30,31] and granules from egg yolk being visible (**Figure 6.6a**). We note that the phospholipids originating from LDLs are not observable since they are too thinly dispersed at the interface upon emulsification[32]. Upon oxidation, more aggregates and granules were observed at droplet interfaces (**Figure 6.6b**). This indicates that proteins in the emulsions not only aggregate in the continuous phase, as described in **Chapter 4** but also at the oil-water droplet interface, as shown in **Figure 6.6**. We note that droplets larger than 1 μm exist in the emulsions, but small droplets (< 500 nm) were predominantly selected for TEM imaging due to the effects of sample preparation using EM grids.
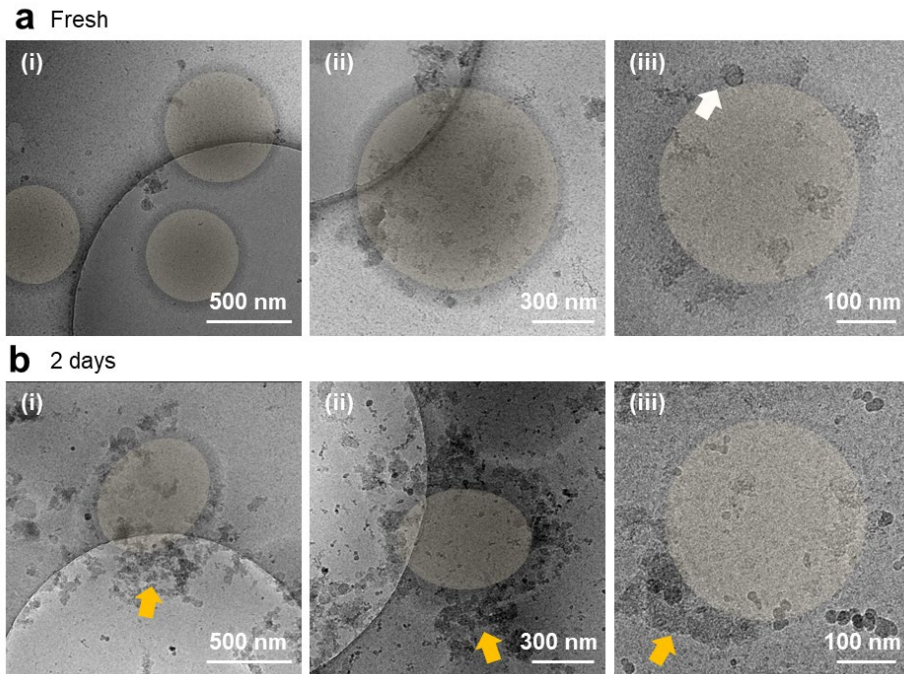
Figure 6.6. Cryo-TEM images of fresh (**a**) and oxidized (**b**) model food emulsions. For visual guidance, the oil droplets are marked in yellow. LDL particles and their aggregates are indicated by white and yellow arrows, respectively. For the oxidized samples, the emulsions were incubated at 40 °C for 2 days with 5 mM of AAPH. Cryo-TEM images in fresh and oxidized emulsions were acquired at magnifications of 6500× (i and ii) and 24000× (iii). A nominal defocus of -20 and -5 μm was applied for magnifications of 6500× and 24000×, respectively. Contrast and brightness were adjusted for visibility.

6.3.5 Feasibility of cryo-correlative imaging in food oxidation studies

Cryo-fluorescence microscopy (cryo-FM) can provide functional information such as lipid and protein oxidation[29], whereas cryo-transmission electron microscopy (cryo-TEM) provides structural information of proteins and potential aggregation upon oxidation[21]. Correlating the information from cryo-FM and cryo-TEM is, however, not trivial[33]. A major challenge is to find the same location in emulsions from cryo-FM and cryo-TEM. One way to find the same position is by using finder grids that have specific letters as markers; thus, the same sample positions can be monitored in both cryo-FM and cryo-TEM. An alternative approach is to generate markers on the EM grid by devitrifying the ice on purpose using high laser intensities. This approach has the advantage that markers are made on standard grids.

To show the feasibility of cryo-correlative imaging in food oxidation studies, the dilute emulsions were prepared on either a Finder/Au or a Copper/Quantifoil EM grid. We first measured the fluorescence images of emulsions using BODIPY 665/676 in cryo-FM before

imaging the same droplets in cryo-TEM. With the Finder/Au EM grid (**Figure 6.7a**), the droplets could be easily tracked based on the letter markers (i). Then, the droplets are correlated in cryo-FM with the fluorescence signals (ii) and cryo-TEM (iii). With the Copper/Quantifoil EM grid (**Figure 6.7b**), a damaged artifact was intentionally made with high laser power (1700 W/cm^2 at 638 nm excitation) on the grid. This approach enables tracking in cryo-TEM with an asymmetric center mark of the EM grid. Again, this method could also correlate the same oil droplets in cryo-FM and cryo-TEM. We confirmed that both methods are applicable for finding the same position in cryo-FM and cryo-TEM.

a Finder/Au EM grid

b Copper/Quantifoil EM grid
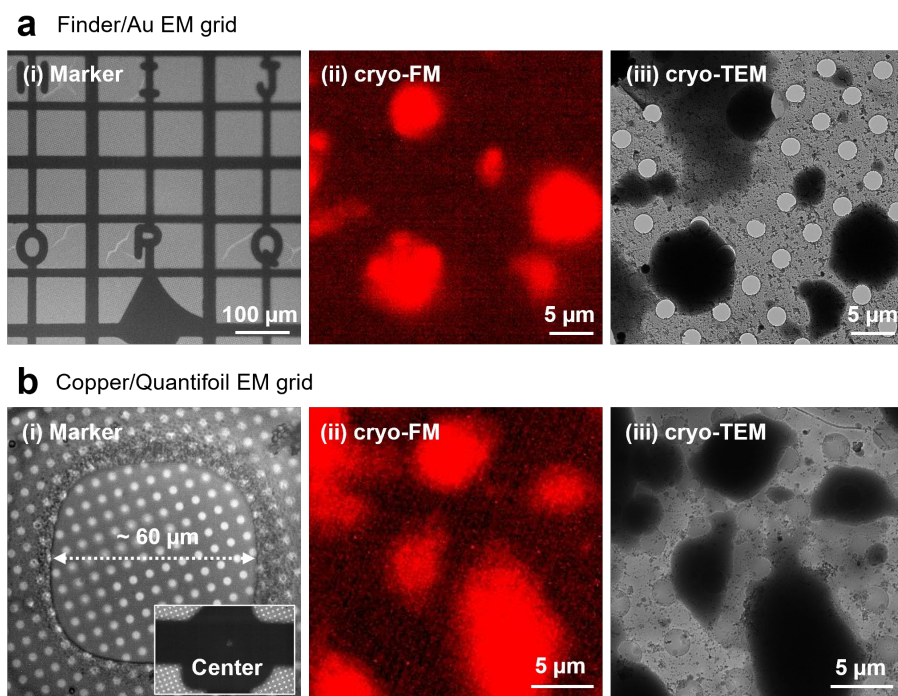
Figure 6.7. Cryo-correlative light and electron microscopy (cryo-CLEM) images of fresh emulsion samples on Finder/Au (**a**) and Copper/Quantifoil EM grids (**b**). (a) The letters on Finder/Au EM grid (i) were used to track oil droplets with native fluorescence of BODIPY 665/676 in cryo-FM (ii) and in cryo-TEM (iii). (b) The markers on the Copper/Quantifoil EM grid were made with the illumination at 1700 W/cm^2 of 638 nm excitation for 1 min (i). The size of the markers indicates the laser spot, approximately the same size as the full width at 90% of the maximum intensity (FW90M). The same droplets were co-localized in cryo-FM (ii) and cryo-TEM (iii).

We could detect individual oil droplets using BODIPY 665/676 in cryo-FM and observe the same droplets in cryo-TEM (**Figure 6.7**). However, resolving droplet interfaces consisting of protein granules was not possible in cryo-TEM due to the thickness of the droplet size, which is larger than 500 nm. With common lab-scale emulsification methods, such as colloid mills, microfluidizers, and high-pressure homogenizers, polydisperse emulsions are obtained that include droplets that are ten times larger than small ones within the emulsions. In the presence

of these large droplets, the fluorescence signals in small droplets are relatively dim; for instance, we could not detect small droplets in the polydisperse system using cryo-FM even though 200 nm beads of a monodisperse system can be easily visualized (**Figure S6.1**). This limitation calls for a sample preparation procedure where for polydisperse emulsions, small droplets are separated from larger ones. An assumption of adopting such a procedure would be that small droplets have a similar coverage of proteins as larger ones. Alternatively, microfluidic emulsification[34] can be used since it provides monodisperse emulsions, as we introduced in **Chapter 5**. In that chapter, we observed that the interfacial coverage of droplets prepared with microfluidic emulsification differed from that of conventional emulsification using a colloid mill. We hypothesized there that microfluidic and colloid mill emulsification, respectively, results in homo- and heterogeneous coverage of droplet interfaces. This opens an experimental route to investigate the effect of homo- and heterogeneous protein coverage of droplet interfaces on lipid oxidation. Our cryo-CLEM approach introduced here opens experimental avenues to investigate the relation between protein coverage of droplet interfaces and the interplay of lipid and protein oxidation.

6.4   Conclusions

We demonstrated the first implementation of correlative imaging of cryo-FM and cryo-TEM for use in food oxidation studies. Significant experimental improvements in cryo-CLEM have been achieved, including the prevention of fogging and controlling the size of the laser beam, thereby achieving a homogenous laser intensity distribution over the field of view of interest. Using cryo-TEM, we could observe more aggregates at the interface of oxidized emulsions than in fresh emulsions. Moreover, we observed lipid oxidation in cryo-condition by monitoring the spectral shift of BODIPY 665/676, thus opening the way for future cryo-correlative oxidation studies. We showed the feasibility of correlative imaging for lipid oxidation and protein structure changes at the oil-water interface upon oxidation. A current limitation of cryo-CLEM is that only small (< 500 nm diameter) droplets can be studied and that fluorescence originating from nearby larger droplets needs to be avoided. Follow-up work on polydisperse emulsions will therefore require a procedure to obtain a fraction of small droplets, likely with a heterogeneous interfacial coverage. Such a procedure will not be required for mono-disperse small droplets obtained by microfluidic emulsification. By comparing both types of emulsion, cryo-CLEM will enable the establishment of the interplay between nanoscale droplet coverage and lipid-protein oxidation. Unraveling this interaction will enable us to effectively engineer the oxidative stabilization of food emulsions, for instance, by manipulating the arrangement of emulsifiers at the interface.

References

1. McClements, D. J. Food emulsions: principles, practices, and techniques. CRC press (2015).
2. McClements, D. J. & Decker, E. A. Lipid oxidation in oil-in-water emulsions: Impact of molecular environment on chemical reactions in heterogeneous food systems. *J Food Sci* **65**, 1270–1282 (2000).
3. Berton-Carabin, C. C., Ropers, M. H. & Genot, C. Lipid Oxidation in Oil-in-Water Emulsions: Involvement of the Interfacial Layer. *Compr Rev Food Sci Food Saf* **13**, 945–977 (2014).
4. Berton-Carabin, C. C., Sagis, L. & Schroën, K. Formation, Structure, and Functionality of Interfacial Layers in Food Emulsions. *Annu Rev Food Sci Technol* **9**, 551–587 (2018).
5. Berton, C., Ropers, M. H., Viau, M. & Genot, C. Contribution of the interfacial layer to the protection of emulsified lipids against oxidation. *J Agric Food Chem* **59**, 5052–5061 (2011).
6. Zhu, Z. *et al.* Impact of Interfacial Composition on Lipid and Protein Co-Oxidation in Oil-in-Water Emulsions Containing Mixed Emulisifers. *J Agric Food Chem* **66**, 4458–4468 (2018).
7. Yang, J. & Xiong, Y. L. Inhibition of Lipid Oxidation in Oil-in-Water Emulsions by Interface-Adsorbed Myofibrillar Protein. *J Agric Food Chem* **63**, 8896–8904 (2015).
8. Giepmans, B. N. G. Bridging fluorescence microscopy and electron microscopy. *Histochemistry and Cell Biology* vol. 130 211–217 (2008).
9. Mironov, A. A. & Beznoussenko, G. v. Correlative microscopy: A potent tool for the study of rare or unique cellular and tissue events. *Journal of Microscopy* vol. 235 308–321 (2009).
10. Brown, E. & Verkade, P. The use of markers for correlative light electron microscopy. *Protoplasma* vol. 244 91–97 (2010).
11. van Elsland, D. M., Bos, E., Overkleeft, H. S., Koster, A. J. & van Kasteren, S. I. The potential of bioorthogonal chemistry for correlative light and electron microscopy: a call to arms. *Journal of Chemical Biology* vol. 8 153–157 (2015).
12. Muller-Reichert, T. & Verkade, P. *Correlative light and electron microscopy II.* (2014).
13. de Boer, P., Hoogenboom, J. P. & Giepmans, B. N. G. Correlated light and electron microscopy: Ultrastructure lights up! *Nature Methods* vol. 12 503–513 (2015).
14. Wolff, G., Hagen, C., Grünewald, K. & Kaufmann, R. Towards correlative super-resolution fluorescence and electron cryo-microscopy. *Biology of the Cell* vol. 108 245–258 (2016).
15. Ayache, J., Beaunier, L., Boumendil, J., Ehret, G. & Laub, D. Physical and Chemical Mechanisms of Preparation Techniques. *Sample Preparation Handbook for Transmission Electron Microscopy* 83–123 (2010).
16. Murk, J. L. A. N. *et al.* Influence of aldehyde fixation on the morphology of endosomes and lysosomes: quantitative analysis and electron tomography. *J Microsc* **212**, 81–90 (2003).
17. Schnell, U., Dijk, F., Sjollema, K. A. & Giepmans, B. N. G. Immunolabeling artifacts and the need for live-cell imaging. *Nature Methods 2012 9:2* **9**, 152–158 (2012).
18. Schultz, P. Cryo-electron microscopy of vitrified specimens. *Q Rev Biophys* **21**, 129–228 (1988).
19. Dahl, R. & Staehelin, L. A. High-pressure freezing for the preservation of biological structure: Theory and practice. *J Electron Microsc Tech* **13**, 165–174 (1989).
20. Steinbrecht, R.A. and Zierold, K. eds., Cryotechniques in biological electron microscopy. *Springer Science & Business Media.* (2012)
21. Yang, S., Takeuchi, M., Friedrich, H., van Duynhoven, J. P. M. & Hohlbein, J. Unravelling mechanisms of protein and lipid oxidation in mayonnaise at multiple length scales. *Food Chem* **402**, 134417 (2023).
22. Berton, C., Genot, C. & Ropers, M. H. Quantification of unadsorbed protein and surfactant emulsifiers in oil-in-water emulsions. *J Colloid Interface Sci* **354**, 739–748 (2011).
23. Kuo, J. *Electron microscopy: methods and protocols.* vol. 369. Springer Science & Business Media. (2007).
24. Tuijtel, M. W., Koster, A. J., Jakobs, S., Faas, F. G. A. & Sharp, T. H. Correlative cryo super-resolution light and electron microscopy on mammalian cells using fluorescent proteins. *Sci Rep* **9**, 1–11 (2019).
25. Chang, Y. W. *et al.* Correlated cryogenic photoactivated localization microscopy and cryo-electron tomography. *Nat Methods* **11**, 737–739 (2014).
26. Liu, B. *et al.* Three-dimensional super-resolution protein localization correlated with vitrified cellular context. *Sci Rep* **5**, (2015).
27. Coady, J. Finite Element Method in MATLAB. Particle in Cell. Preprint at https://www.particleincell.com/2012/matlab-fem/ (2012).
28. Kaufmann, R., Hagen, C. & Grü Newald, K. Fluorescence cryo-microscopy: current challenges and prospects. (2014).
29. Yang, S., Verhoeff, A. A., Merkx, D. W. H., van Duynhoven, J. P. M. & Hohlbein, J. Quantitative Spatiotemporal Mapping of Lipid and Protein Oxidation in Mayonnaise. *Antioxidants 2020, Vol. 9, Page 1278* **9**, 1278 (2020).

30. Anton, M. Egg yolk: structures, functionalities and processes. *J Sci Food Agric* **93**, 2871–2880 (2013).

31. Anton, M. *et al.* Chemical and structural characterisation of low-density lipoproteins purified from hen egg yolk. *Food Chem* **83**, 175–183 (2003).

32. Sirvente, H. *et al.* Structuring and functionalization of dispersions containing egg yolk, plasma and granules induced by mechanical treatments. *J Agric Food Chem* **55**, 9537–9544 (2007).

33. van Driel, L. F., Valentijn, J. A., Valentijn, K. M., Koning, R. I. & Koster, A. J. Tools for correlative cryo-fluorescence microscopy and cryo-electron tomography applied to whole mitochondria in human endothelial cells. *Eur J Cell Biol* **88**, 669–684 (2009).

34. ten Klooster, S., Berton-Carabin, C. & Schroën, K. Design insights for upscaling spontaneous microfluidic emulsification devices based on behavior of the Upscaled Partitioned EDGE device. *Food Research International* 112365 (2022).
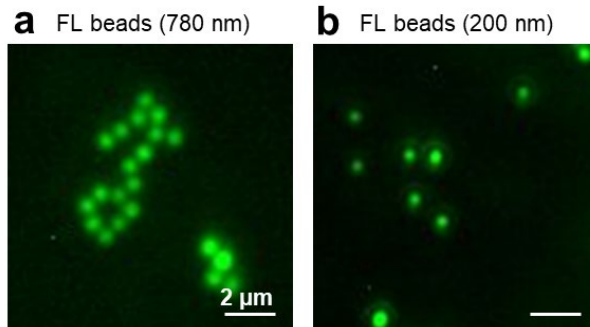
6.5   Appendix

Figure S6.1. Fluorescent beads in cryogenic fluorescence microscopy (cryo-FM). 780 nm (**a**) and 200 nm (**b**) diameter sized-fluorescent beads are visible in cryo-FM. The samples were illuminated at 520 nm (50 W/cm^2).

7

General Discussion

7.1 Main findings and outline of the discussion

In oil-in-water food emulsions, lipid oxidation is initiated at the oil droplet interface, where lipids are in close contact with pro- and anti-oxidants. In addition, reactive oxidation intermediates may exchange between droplets via a transport mechanism, thus adding another level of complexity. Even though the role of the interfacial area is of importance, it can yet not properly be examined due to a lack of suitable experimental and analytical frameworks. To date, most studies have been conducted with bulk measurements, thus neglecting the role of colloidal interfaces and transport mechanisms in lipid and protein oxidation. In this thesis, we implemented and applied a range of microscopy techniques to localize protein and lipid oxidation at multiple length scales. We first demonstrated localization in a droplet specific manner (**Chapter 3**) and next in a multi-scale manner (**Chapter 4**) in mayonnaise, a complex food emulsion. Next, in a model emulsion, the impact of emulsification and droplet sizes on oxidation was visualized as different length scales (**Chapter 5**). Finally, we were able to demonstrate the potential of correlative multiscale imaging to link oxidation with events at nanoscale droplet interfaces (**Chapter 6**). In this chapter, we will discuss these newly developed methods for quantifying local lipid and protein oxidation from microscopy data. Then, we will elaborate on the current challenges in unraveling lipid and protein co-oxidation. Furthermore, we will discuss the differences between real and model systems used in oxidation studies. Finally, we will outline future work toward achieving a quantitative multiscale view of lipid oxidation using additional super-resolution techniques.

7.2 Quantifying lipid and protein oxidation using fluorescence microscopy

As fluorescence microscopy is not yet commonly used to study oxidation in food systems, its potential in this area has yet to be realized. Consequently, there is a need to develop methods for accurately interpreting the extent of lipid and protein oxidation from imaging data. Further development is also required to clarify the role of co-oxidation of lipids and proteins. Here, we will discuss the quantification methods we developed and suggest further improvements.

7.2.1 Quantification of lipid oxidation

Choosing a suitable fluorescence probe is important for studying lipid oxidation with microscopy. BODIPY 665/676, a lipophilic oxidation-sensitive dye, has been widely used as a marker to localize lipid oxidation in food emulsions[1–4]. Oxidation of BODIPY 665/676 is detected by the shift of the emission spectrum from longer (680 - 750 nm) to shorter wavelengths (580 - 660 nm) upon reaction with peroxyl radicals[5,6]. The use of BODIPY 665/676 for studying lipid oxidation is based on these spectral intensity changes. The changes in fluorescence

emission upon oxidation lead to a decrease in intensity at longer wavelengths and an increase in intensity at shorter wavelengths. However, these intensity changes are not linearly corresponding to each other due to the different fluorescence quantum yields of each state and other effects, such as the loss of BODIPY 665/676 in droplets by diffusion. This could lead to the over- or underestimation of lipid oxidation extent in individual single droplets.

In **Chapter 5,** we evaluated lipid oxidation with BODIPY 665/676 in whey protein isolate (WPI)-stabilized emulsions via the decrease of red fluorescence. The (average) intensity decrease of red fluorescence from BODIPY 665/676 could be correlated with the simulation data of native BODIPY 665/676 concentration (**Figure 7.1a**). We also could further simulate the formation of lipid peroxyl radicals which was inversely correlated with the red fluorescence intensity. However, in the case of Tween 20-stabilized emulsions, the emulsions showed a fast decrease in red fluorescence (**Figure 7.1b**), whereas there was no increase in green fluorescence (**Figure 7.1c**). We did not observe this phenomenon in protein-stabilized emulsions. Therefore, the expected effects of oxidation on the fluorescence spectrum of BODIPY 665/676 should be verified before imaging is conducted for oxidation studies.
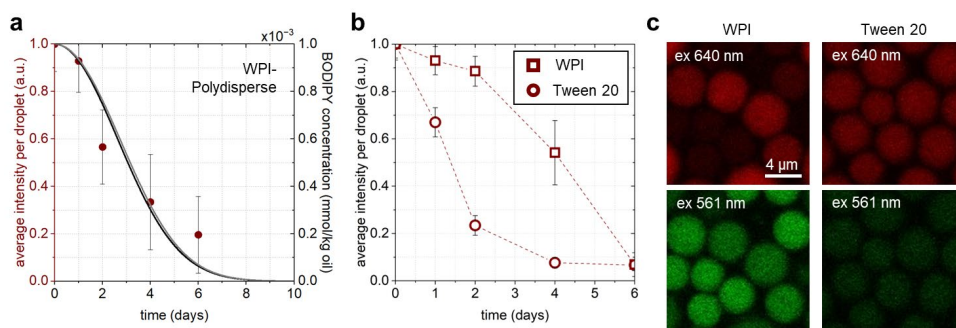

Figure 7.1. The changes in red fluorescence intensity of BODIPY 665/676 as a lipid oxidation marker (adapted from **Chapter 5**). (**a**) The decrease of red fluorescence from experimental data and native BODIPY 665/676 concentration from simulation in WPI-stabilized polydisperse emulsions. (**b**) The decreased red fluorescence of BODIPY 665/676 in WPI- and Tween 20-stabilized monodisperse emulsions. (**c**) Images of BODIPY 665/676 fluorescence, excited at 640 and 561 nm in monodisperse WPI-stabilized emulsions after four days and monodisperse Tween 20 emulsions after one day of oxidation.

Then, the question remains how to quantify lipid oxidation using BODIPY 665/676 more systematically. The last section of this chapter will address this and other concerns with a recommended workflow for achieving a quantitative multiscale view of lipid and protein oxidation.

7.2.2   Evaluating the dependency of lipid and protein oxidation on droplet size

In **Chapter 3**, we imaged lipid oxidation in droplets using BODIPY 665/676 and segmented the individual droplets for analysis. The level of lipid oxidation in individual droplets was fitted

with a modified Gompertz curve, and the growth rate obtained from the fitting was plotted against the inverse of the droplet radius. However, as the Gompertz curve is a semi-descriptive function, it is difficult to accurately define the obtained growth rate in chemical terms. To overcome the limitation of fitting with a semi-descriptive function, we propose a mechanistic kinetic model as used in **Chapter 5**, which comprises the kinetics of relevant oxidation reactions. This would allow us to assess the impact of the droplet size on defined kinetic reaction parameters, thus resulting in a better interpretation of chemical terms.

7.3   New tools for protein and lipid oxidation studies

The two main chemical phenomena in protein-stabilized emulsions are lipid peroxidation and chemical protein modifications, including protein oxidation. Although the effect of protein oxidation on emulsion stability and interfacial properties has been intensively investigated, little attention has been devoted to lipid and protein co-oxidation [7–10]. It has been previously reported that lipid and protein oxidation are linked, but it has remained difficult to measure which of the phenomena first is taking the lead [11,12]. To answer this question, it is essential to detect the early stage of protein oxidation. Furthermore, the acquisition of lipid oxidation data that covers all size ranges of droplets is required. Here, we will first discuss the challenges of detecting protein oxidation at an early stage, and we will then continue to address the challenges of capturing lipid oxidation over the full range of droplet sizes.

7.3.1   Methods for the early detection of protein oxidation

To measure whether lipid or protein oxidation comes first, early detection of protein oxidation is necessary. Protein radicals are the earliest products to be formed during oxidation, but they are too short-lived to accumulate in steady-state concentrations. Hence spin traps need to be used to form stable radical adducts. In **Chapter 4**, we introduced fluorescently labeled spin traps (CAMPO-AFDye 647) to detect early-stage protein oxidation. We observed an accumulation of CAMPO-AFDye 647 at the oil droplet interface in emulsions over time, indicating that protein radicals had been formed. The next step is quantifying the accumulated spin trap adducts, which is difficult to perform in imaging mode. Spin trap adducts of CAMPO-AFDye 647 can be detected and quantified by ESR spectroscopy as DMPO, the original structure of CAMPO, has been used to detect free protein radicals [13–15]. However, spin trap adducts of protein radicals typically appear with broad and overlapped signals and extensive method development will be required to achieve their quantification using ESR [15].

7.3.2   Capturing different droplet sizes in polydisperse emulsions

High-shear emulsification, such as colloid mills and high-pressure homogenizers, typically results in polydisperse droplet size distributions in oil-in-water food emulsions. Small droplets

7

can oxidize faster than larger ones and can produce reactive intermediates. These intermediates, such as radicals and hydroperoxides, can be transported to larger droplets where they can initiate oxidation. Therefore, to fully understand oxidation in whole emulsions, it is necessary to capture oxidation for all droplet sizes in a time-dependent manner. A current bottleneck is to capture droplets with sub-micron diameters.

In **Chapter 2**, we discussed the achievable resolution in optical and electron microscopy. Confocal laser scanning microscopy (CLSM) and re-scan confocal microscopy (RCM) can be easily applied to conventional oil-in-water emulsions, for instance, milk, cream, dressings, mayonnaise, and sauces which have a feature size of 250 nm – 100 μm. However, with the resolution limit of confocal microscopy being around 200 nm, droplets smaller than around < 200 nm might be overlooked, thereby leading to the potential misinterpretation of the total extent of lipid oxidation. Alternatively, fluorescence based super-resolution microscopy, which allows resolving features around 50 nm and below, could be applied to study lipid and protein oxidation of smaller droplets.

Cryo-CLEM is another option to visualize small droplets, as introduced in **Chapter 6**. For the application of cryo-CLEM, small droplets (< 200 nm) can be separated from the conventional oil-in-water emulsions using centrifugation and imaged in cryo-CLEM. At the same time, the larger droplets (> 200 nm) can be imaged in confocal microscopy as conducted in **Chapter 3**, **4** and **5**. We expect that combining information on lipid oxidation in large droplets obtained with CLSM and on small droplets with either super-resolution microscopy or cryo-CLEM will reveal the mechanisms of inter-droplet transport of reactive lipid oxidation intermediates by capturing time-dependent oxidation in all ranges of droplet sizes.

7.4   Closing the gap between model systems and real food emulsions

The ultimate goal of food oxidation studies is to understand the exact oxidation mechanism to develop strategies that delay food deterioration in real food systems. Many studies focus on model systems, which are simpler and more applicable to the measurements[16,17]. In this thesis, we encountered several cases where oxidation localization methods revealed the limitations of using model systems. These will briefly be discussed in the next sections.

7.4.1   Enhancing oxidation rates with oxidation initiators and temperature

To promote lipid oxidation under experimental conditions, oxidation initiators like 2,2'-Azobis (2-amidinopropane) dihydrochloride (AAPH) or azobis (4-methoxy-2,4-dimethylvaleronitrile) (AMVN) can be used. The addition of initiators makes it easier to conduct faster experiments but is also adding additional complexity to the oxidation system. For instance, oxidation initiators not only cause lipid oxidation but can also promote protein oxidation in the continuous

phase[12]. Adding AAPH to the system can also amplify the impact of droplet sizes on the lipid oxidation rate because a water-soluble initiator will initiate the lipid oxidation at the interface, favoring oxidation in small droplets over large ones. This amplification effect may not necessarily reflect conditions in real food emulsions.

In this thesis, we accelerated lipid oxidation by incubating samples at elevated temperatures ranging from 30 to 40 °C. Changing temperatures will change lipid oxidation rates by enhancing diffusion coefficients and reaction rates[18,19]. These kinetics enhancements may blur heterogeneity in lipid oxidation that is present at ambient conditions. Hence, it is recommended that findings on the heterogeneity of lipid oxidation are validated at multiple temperatures.

7.4.2   Oil phase concentration

In oil-in-water (O/W) food emulsions, the oil concentration can vary from a fraction of a percent, like fruit beverages, to more than 80%, like mayonnaise[20]. In this section, we will discuss the effect of oil density with mass transport phenomena of reactive intermediates on lipid oxidation[21]. In our experiments, we varied the oil fraction from 78 wt.% for the real mayonnaise system (**Chapter 3**) to 10 wt.% for the model system (**Chapter 6**). Changing the oil concentration, however, alters the distances between the oil droplets, which can affect the inter-droplet mass transfer. In O/W emulsions, three mechanisms of mass transfer exist[21]; (1) diffusion, (2) collision-exchange-separation, (3) micelle-assisted transfer. In emulsions containing a high oil concentration, the distance between the droplets becomes shorter (when the droplet size remains the same), resulting in more effective mass transport (2 & 3). Especially, hydroperoxide molecules (LOOH) have a longer half-life than peroxyl radicals (LOO*) that can transfer between oil droplets[22]. This effect may influence the initiation stage, which is a transfer-controlled rate meaning that the rate of lipid oxidation is limited only by how fast oxidants can transfer from the oxidized oil droplet to the others. Consequently, it is also necessary to consider the changes in mass transport mechanisms to interpret the data at different oil concentrations. The interpretation can be further resolved by observing time-dependent lipid oxidation in individual droplets using microscopy with varying oil concentrations in the emulsion.

7.4.3   The role of emulsifiers

In the real food and model systems, emulsifiers are often present in concentrations exceeding the coverage required for the oil droplet interface[18], resulting in unadsorbed emulsifiers in the continuous phase. The role of unadsorbed emulsifiers can differ depending on their type and concentration. For instance, surfactants can form micelles that will help exchange lipid hydroperoxides, antioxidants, and metal ions if the concentration exceeds its critical micelle concentration (CMC) value. Consequently, emulsifiers can cause an increase or decrease in lipid oxidation rate by participating in the mass transport mechanism[22]. Unadsorbed proteins are also

involved in the mechanisms of lipid oxidation. This has been shown in experimental studies where unadsorbed proteins in the water phase either lowered[23] or enhanced[24] oxidation rates. The exact role of emulsifiers can be further resolved by localizing lipid oxidation with varying concentrations of emulsifiers.

In **Chapter 5**, we compared the lipid oxidation in Tween 20- and WPI-stabilized emulsions prepared with a microfluidic device that generates monodisperse droplets. One interesting result was that the formation of lipid hydroperoxides and aldehydes was faster in WPI-stabilized than in Tween 20-stabilized emulsions when conditions such as pH, the concentration of emulsifiers, and droplet size, were kept the same (**Figure 7.2a and b**). We attributed this to the densely packed interface stabilized by Tween 20 under mild emulsification, whereas WPI includes different types of proteins like β-Lactoglobulin and α-Lactalbumin, which can induce heterogeneity of the interfaces. These results highlight the importance of considering the droplet interfacial structure, for example, by using cryo-CLEM (**Chapter 6**).
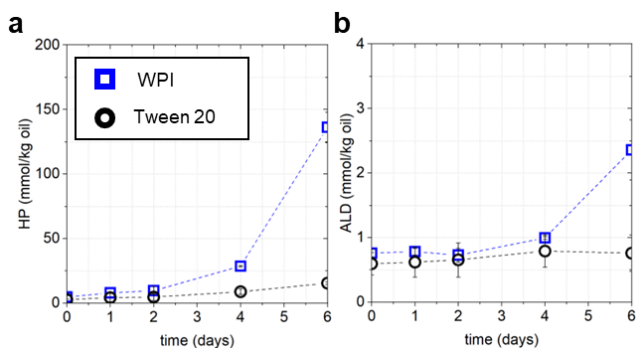

Figure 7.2. The role of emulsifiers on lipid oxidation. (**a-b**) The formation of hydroperoxides (a) and aldehydes (b) in WPI- and Tween 20-stabilized monodisperse emulsions. The figures are adapted from **Chapter 5**.

7.5   Outlook

7.5.1   The recommended workflow for localizing protein and lipid oxidation

For a solid understanding of interpreting lipid oxidation from imaging data, we recommend a comprehensive and structured approach for future imaging studies (**Figure 7.3**). As we showed in **Chapter 5**, low concentrations (< 50 µM) of BODIPY 665/676 do not perturb the lipid oxidation mechanism. Thus, we can use the same sample tube where BODIPY 665/676 has been added for oxidation localization purposes and bulk NMR-based assessments of primary (hydroperoxides) and secondary (aldehydes) oxidation products. After taking a small amount (< 10 µL) for imaging, the samples can be frozen and thawed for additional measurements. In most cases, the freeze-thaw step is effective in breaking the emulsion. Hence the oil phase can be obtained in a straightforward manner for bulk NMR and fluorescence spectroscopic assessment. This allows for comparing the local characteristics of lipid oxidation with bulk quantification by NMR and spectrophotometry. Lipid and protein oxidation in droplets with diameters larger than

146

1 µm can be assessed by CLSM, and smaller droplets (< 1 µm) are accessible via super-resolution microscopy[25] (next section) or cryo-CLEM (**Chapter 6**). Access to quantitative bulk (NMR and fluorescence spectroscopy) and semi-quantitative local information (microscopy) on lipid oxidation provides parameters that can be combined with mechanistic modeling, as demonstrated in **Chapter 5**. We foresee that this combination will enable researchers to gain an unparalleled understanding of lipid and protein oxidation in food emulsions, including aspects of interfacial and transport mechanisms.
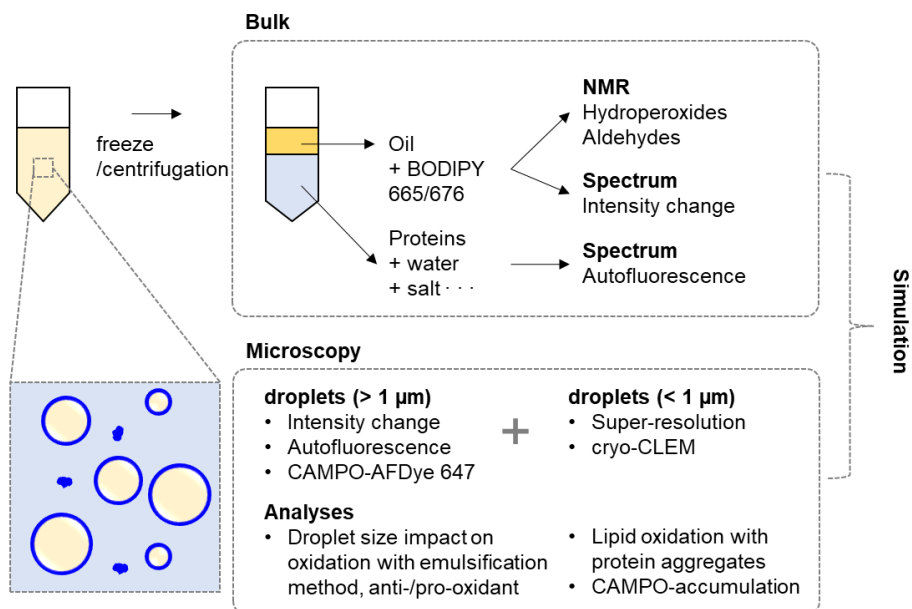

Figure 7.3. Schematic of recommended workflow for assessment of local lipid and protein oxidation. The prepared emulsions can be measured in bulk by NMR and fluorescence spectroscopy and by microscopy for local assessment of protein (autofluorescence, CAMPO-AFDye 647 spin trapping) and lipid oxidation (BODIPY 676/665).

7.5.2 Localizing oxidation events with super-resolution microscopy

Fluorescence super-resolution microscopy is widely used in the life sciences yet rarely in the food sciences[25–27]. A frequently used super-resolution microscopy technique is stochastic optical reconstruction microscopy (STORM)[28], which uses the blinking of fluorophores such as Alexa Fluor647[29]. The details about STORM are described in **Chapter 2**. Here, we briefly demonstrate the feasibility of monitoring protein oxidation at sub-diffraction limited resolution by STORM with the fluorescently labeled spin trap CAMPO-AFDye647. For STORM imaging, we used a home-built microscope[30]. We implemented CAMPO-AFDye 647 in two protein-stabilized emulsions, using egg yolk and whey protein isolate (WPI) as emulsifiers. For egg yolk stabilized

emulsions, heterogeneous accumulation of CAMPO-AFDye 647 at the interface was observed (**Figure 7.4a**). This indicates a heterogeneous formation of protein radicals which can be explained by multiple emulsifiers being adsorbed at the droplet interface in a heterogeneous manner during high-shear emulsification. The interfacial complexity is due to the composition of egg yolk, which introduces apoproteins, phospholipids and phosvitin during emulsification[31]. As apoproteins and phosvitin are immobilized at the interface, their radicals can be localized with spin traps. This immobilization does not occur for phospholipids, as their radicals can diffuse within the droplets or in the water phase as micelles. The empty patches at the interface are, therefore, likely covered with phospholipids. On the other hand, WPI-stabilized emulsions showed relatively homogeneous protein oxidation (**Figure 7.4b**), which can be attributed to the simpler composition of WPI (beta-lactoglobulin and alpha-lactalbumin) compared to the egg yolk.
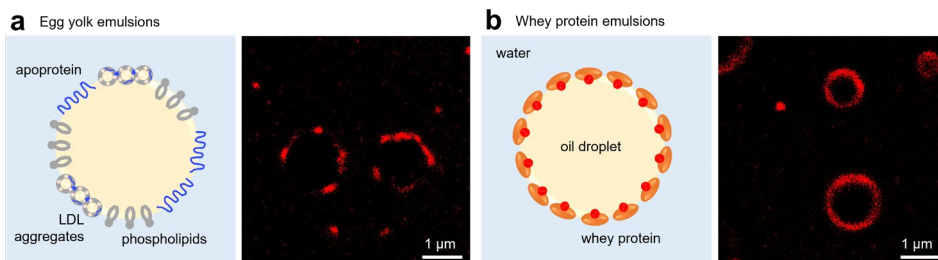

Figure 7.4. 2D dSTORM images of fluorescently labeled spin traps (CAMPO - AFDye 647) in egg yolk (**a**) and WPI (**b**)-stabilized emulsions. The red color indicates the localization of CAMPO-AFDye 647, indicating protein oxidation at interfaces. Due to the complexity of the emulsifier, egg yolk-stabilized emulsions show more heterogeneous oxidation at the interface than WPI-stabilized emulsions.

In our application of STORM, it is required to remove unadsorbed proteins by washing the continuous phase, including unadsorbed proteins, three times with a buffer. These washing steps improved the localization of CAMPO-AFDye 647, but we note that aggregates of proteins at the interface might also have been removed during the washing steps. Oil-in-water (O/W) food emulsions often contain a high concentration of emulsifiers which cause high background signals due to unadsorbed emulsifiers in the continuous phase. The unadsorbed emulsifiers in the continuous phase can react with spin-trap molecules and diffuse during the measurements. Even though dSTORM requires additional washing steps, this super-resolution technique allowed us to detect the heterogeneous protein oxidation at the interface and enabled us to resolve droplets smaller than the 1 µm range (**Figure 7.4**).

Another emerging SMLM approach is point accumulation in nanoscale topography (PAINT)[32], which does not require photo-switching but relies on fluorophores reversibly binding to a target. The most prominent variant of PAINT is DNA-PAINT[33,34], where transient immobilization is

achieved by the hybridization of DNA strands. DNA-PAINT gives a longer binding event than STORM due to the programmable DNA sequence, resulting in high localization precision. Additionally, DNA-PAINT does not suffer from photobleaching as imaging strands get consciously renewed. DNA-PAINT, in combination with spin traps, therefore holds a promise in oxidation studies, with single radical detection as a unique advantage.

To achieve this, we designed the CAMPO-DNA PAINT to localize free radical spin traps. CAMPO can be trapped in the presence of protein-free radicals, as described in **Chapter 4**. Here, we conjugated CAMPO to a 9-mer of ssDNA (3'-TTG GGA GGA-5'), including two-steppers (TT). The CAMPO-DNA will be added to the sample and bind to oxidized proteins. Then, excess strands will be washed away. For imaging, the complementary ssDNA sequence (5'-C CCT CCT-3' labeled with a fluorophore) is added and then able to colocalize with the immobile CAMPO-DNA (**Figure 7.5**). A prerequisite for the PAINT approach is that the DNA conjugate can diffuse freely, and we successfully verified the self-diffusion behavior of the DNA-fluorophore conjugate in a complex emulsion like dilute mayonnaise. We recommend further PAINT experiments to assess single radical formation at droplet interfaces.
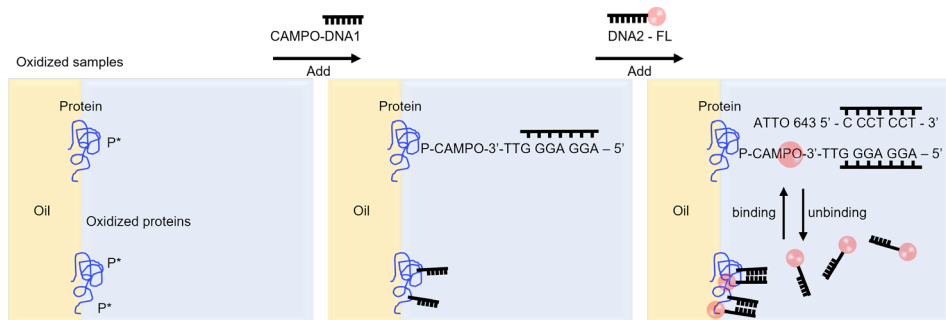

Figure 7.5. Schematic of CAMPO-DNA PAINT. In the presence of protein-free radicals, the CAMPO-DNA sequence can trap the protein-free radicals at the interface. With the addition of another sequence of DNA pair conjugated with a fluorophore (DNA2-FL), CAMPO can be localized by binding and unbinding of DNA2-FL. CAMPO-DNA was synthesized by SyMO-Chem B.V. (Eindhoven, the Netherlands).

References

1.   Li, P., McClements, D. J. & Decker, E. A. Application of flow cytometry as novel technology in studying the effect of droplet size on lipid oxidation in oil-in-water emulsions. *J Agric Food Chem* **68**, 567–573 (2019).

2.   Li, P., McClements, D. J. & Decker, E. A. Application of flow cytometry as novel technology in studying lipid oxidation and mass transport phenomena in oil-in-water emulsions. *Food Chem* **315**, 126225 (2020).

3.   Banerjee, C., Breitenbach, T. & Ogilby, P. R. Spatially resolved experiments to monitor the singlet oxygen initiated oxidation of lipid droplets in emulsions. *ChemPhotoChem* **2**, 586–595 (2018).

4.   Yang, S., Verhoeff, A. A., Merkx, D. W. H., van Duynhoven, J. P. M. & Hohlbein, J. Quantitative spatiotemporal mapping of lipid and protein oxidation in mayonnaise. *Antioxidants* **9**, 1–13 (2020).

5.   Naguib, Y. M. A. Antioxidant activities of astaxanthin and related carotenoids. *J Agric Food Chem* **48**, 1150–1154 (2000).

6.   Raudsepp, P., Brüggemann, D. A. & Andersen, M. L. Detection of radicals in single droplets of oil-in-water emulsions with the lipophilic fluorescent probe BODIPY665/676 and confocal laser scanning microscopy. *Free Radic Biol Med* **70**, 233–240 (2014).

7.   Zhu, Z. *et al.* Impact of Interfacial Composition on Lipid and Protein Co-Oxidation in Oil-in-Water Emulsions Containing Mixed Emulisifers. *J Agric Food Chem* **66**, 4458–4468 (2018).

8.   Yi, J. *et al.* Impact of interfacial composition on co-oxidation of lipids and proteins in oil-in-water emulsions: Competitive displacement of casein by surfactants. *Food Hydrocoll* **87**, 20–28 (2019).

9.   Gürbüz, G. *et al.* Protein–lipid co-oxidation in emulsions stabilized by microwave-treated and conventional thermal-treated faba bean proteins. *Food Sci Nutr* **6**, 1032–1039 (2018).

10.   Li, Q., Zheng, J., Ge, G., Zhao, M. & Sun, W. Impact of heating treatments on physical stability and lipid-protein co-oxidation in oil-in-water emulsion prepared with soy protein isolates. *Food Hydrocoll* **100**, 105167 (2020).

11.   Lund, M. N., Heinonen, M., Baron, C. P. & Estévez, M. Protein oxidation in muscle foods: A review. *Mol Nutr Food Res* **55**, 83–95 (2011).

12.   Berton, C., Ropers, M. H., Guibert, D., Solé, V. & Genot, C. Modifications of interfacial proteins in oil-in-water emulsions prior to and during lipid oxidation. *J Agric Food Chem* **60**, 8659–8671 (2012).

13.   Taniguchi, H. & Madden, K. P. An in Situ Radiolysis Time-Resolved ESR Study of the Kinetics of Spin Trapping by 5,5-Dimethyl-1-pyrroline-N-oxide. (1999) doi:10.1021/ja993140l.

14.   Mason, R. P. Using anti-5,5-dimethyl-1-pyrroline N-oxide (anti-DMPO) to detect protein radicals in time and space with immuno-spin trapping. *Free Radic Biol Med* **36**, 1214–1223 (2004).

15.   Davies, M. J. & Hawkins, C. L. EPR spin trapping of protein radicals. *Free Radic Biol Med* **36**, 1072–1086 (2004).

16.   Villeneuve, P. *et al.* Lipid oxidation in emulsions and bulk oils: a review of the importance of micelles. *Critical Reviews in Food Science and Nutrition* Preprint at https://doi.org/10.1080/10408398.2021.2006138 (2021).

17.   Laguerre, M., Tenon, M., Bily, A. & Birtić, S. Toward a Spatiotemporal Model of Oxidation in Lipid Dispersions: a Hypothesis-Driven Review. *European Journal of Lipid Science and Technology* **122**, 1900209 (2020).

18.   Berton-Carabin, C. C., Ropers, M. H. & Genot, C. Lipid Oxidation in Oil-in-Water Emulsions: Involvement of the Interfacial Layer. *Compr Rev Food Sci Food Saf* **13**, 945–977 (2014).

19.   Jacobsen, C. Oxidative Stability and Shelf Life of Food Emulsions. *Oxidative Stability and Shelf Life of Foods Containing Oils and Fats* 287–312 (2016) doi:10.1016/B978-1-63067-056-6.00008-2.

20.   McClements, D. J. & Decker, E. A. Lipid oxidation in oil-in-water emulsions: Impact of molecular environment on chemical reactions in heterogeneous food systems. *J Food Sci* **65**, 1270–1282 (2000).

21.   Laguerre, M., Bily, A., Roller, M. & Birtić, S. Mass Transport Phenomena in Lipid Oxidation and Antioxidation. *Annu Rev Food Sci Technol* **8**, 391–411 (2017).

22.   Keramat, M., Ehsandoost, E. & Golmakani, M.-T. Recent Trends in Improving the Oxidative Stability of Oil-Based Food Products by Inhibiting Oxidation at the Interfacial Region. *Foods 2023, Vol. 12, Page 1191* **12**, 1191 (2023).

23.   Ries, D., Ye, A., Haisman, D. & Singh, H. Antioxidant properties of caseins and whey proteins in model oil-in-water emulsions. *Int Dairy J* **20**, 72–78 (2010).

24.   Faraji, H., Julian, D. & Decker, E. A. Role of Continuous Phase Protein on the Oxidative Stability of Fish Oil-in-Water Emulsions. (2004) doi:10.1021/jf035346i.

25.   Hohlbein, J. Single-molecule localization microscopy as an emerging tool to probe multiscale food structures. *Food Structure* **30**, 100236 (2021).

26.   Glover, Z. J. *et al.* Super-resolution microscopy and empirically validated autocorrelation image analysis discriminates microstructures of dairy derived gels. *Food Hydrocoll* **90**, 62–71 (2019).

27. Jabermoradi, A., Yang, S., Gobes, M. I., Van Duynhoven, J. P. M. & Hohlbein, J. Enabling single-molecule localization microscopy in turbid food emulsions. *Philosophical Transactions of the Royal Society A* **380**, (2022).

28. Rust, M. J., Bates, M. & Zhuang, X. Sub-diffraction-limit imaging by stochastic optical reconstruction microscopy (STORM). (2006) doi:10.1038/NMETH929.

29. Heilemann, M. *et al.* Subdiffraction-Resolution Fluorescence Imaging with Conventional Fluorescent Probes. *Angewandte Chemie International Edition* **47**, 6172–6176 (2008).

30. Martens, K. J. A. *et al.* Visualisation of dCas9 target search in vivo using an open-microscopy framework. *Nat Commun* **10**, 1–11 (2019).

31. Anton, M. Egg yolk: structures, functionalities and processes. *J Sci Food Agric* **93**, 2871–2880 (2013).

32. Sharonov, A. & Hochstrasser, R. M. Wide-field subdiffraction imaging by accumulated binding of diffusing probes. *Proc Natl Acad Sci U S A* **103**, 18911 (2006).

33. Jungmann, R. *et al.* Single-molecule kinetics and super-resolution microscopy by fluorescence imaging of transient binding on DNA origami. *Nano Lett* **10**, 4756–4761 (2010).

34. Nieves, D. J., Gaus, K. & Baker, M. A. B. DNA-Based Super-Resolution Microscopy: DNA-PAINT. (2018) doi:10.3390/genes9120621.

7

Summary

Lipid oxidation is a major cause of product deterioration in oil-in-water food emulsions. However, the current methods used to evaluate lipid oxidation in food products are limited as they only focus on one aspect of the process and do not fully capture its complexity. Additionally, protein emulsifiers that are utilized to stabilize oil-in-water emulsions may either promote or delay lipid oxidation, and the effects of these protein emulsifiers at the interface on lipid oxidation are poorly understood. The complex nature of food emulsions necessitates further investigation into how the composition of the interface interacts with lipid and protein oxidation in a spatiotemporal manner, which has remained challenging to observe using traditional methods. Understanding the co-oxidation of lipids and proteins is also critical for understanding how and when they can act as pro- or anti-oxidants at the droplet interfaces.

In this thesis, we developed and applied a range of fluorescence microscopy techniques to obtain a spatiotemporal view of lipid and protein oxidation in food emulsions. Microscopy offers the advantage that lipid and protein oxidation can be studied locally and in a time-dependent manner without requiring additional extraction steps. Therefore, microscopy should also enable unraveling of lipid and protein co-oxidation mechanisms. Before demonstrating the application of microscopy techniques and specific fluorophores for food oxidation studies, **Chapter 2** explains the fundamental methodological principles of fluorescence microscopy and the use of fluorophores and autofluorescence, respectively, as a marker for lipid and protein oxidation.

A CSLM method for tracking the same oil droplets in mayonnaise over 14 days was developed to map local lipid and protein oxidation (**Chapter 3**). Local lipid oxidation was monitored via changes in the fluorescence spectrum of BODIPY 665/676. An increase in protein oxidation was observed by measuring changes in autofluorescence intensity. The study investigated how oxidation rates varied depending on droplet sizes by segmenting and tracking the same oil droplets during incubation. This approach also allowed for unraveling the pro- and anti-oxidant roles of L-ascorbic acid and α-tocopherol on lipids and proteins. The removal of the lipid antioxidant (α-tocopherol) promoted not only lipid oxidation but also protein oxidation, indicating that lipid oxidation can promote protein oxidation at the interface.

The localization of protein oxidation at the interface was further investigated in **Chapter 4**. The water-soluble fluorescent labeled spin-trap (CAMPO-AFDye 647) was introduced to detect the early stage of protein oxidation in dilute mayonnaise. Autofluorescence was used as a marker of oxidized proteins and was co-localized with accumulated spin traps after five days of oxidation in both the continuous phase and at the oil droplet interface. The results showed that CAMPO-AFDye 647 accumulation could detect protein oxidation at the early stage, whereas protein autofluorescence is only detectable at a much later stage. Additionally, the study observed the oxidation-induced aggregation of low-density lipoprotein particles (LDLs) using cryo-transmission electron microscopy (cryo-TEM). These findings provide valuable information on

the mechanisms of protein oxidation at the interface and highlight the potential of the CAMPO-AFDye 647 spin trap as a tool for detecting early-stage protein oxidation.

Chapter 5 continued with the localization of lipid and protein oxidation in mono- and poly-disperse whey protein isolate (WPI)-stabilized model emulsions. This study validated the use of lipid oxidation-sensitive fluorescent dye (BODIPY 665/676) as a marker for lipid oxidation by mechanistic modeling of primary and secondary oxidation kinetics without and with BODIPY 665/676. The kinetics of lipid oxidation in the WPI-stabilized emulsions could be explained by differences in droplet size distribution and heterogeneous packing of proteins at the droplet interfaces. The accumulation of the CAMPO-AFDye 647 spin trap revealed differences in the packing of proteins at the droplet interfaces of mono- and polydisperse WPI-stabilized emulsions. Moreover, this study showed that both lipid and protein oxidation proceeded in highly heterogeneous fashions in WPI-stabilized emulsions, which cannot be observed by bulk measurements of lipid oxidation products.

In **Chapter 6**, we showed the feasibility of correlative imaging for studying lipid oxidation and protein structure changes at the oil-water interface upon oxidation. We demonstrated the first implementation of correlative imaging with cryo-fluorescence microscopy (cryo-FM) and cryo-transmission electron microscopy (cryo-TEM) for food oxidation studies. Experimental improvements in cryo-correlative light and electron microscopy (cryo-CLEM) have been achieved for further stable measurements. Aggregates of protein granules at the interface upon oxidation were observed in cryo-TEM, and it was demonstrated that the wavelength shift of the lipid oxidation-sensitive dye BODIPY 665/676 could be measured at 77 K (-196 °C) by cryo-FM thus opening the way for future cryo-correlative oxidation studies.

The challenges and prospects of using microscopic techniques for localizing lipid and protein oxidation were discussed in **Chapter 7**. Based on the findings in this thesis, a workflow was recommended for obtaining localized information on proteins and lipid oxidation in a robust manner. Furthermore, we outlined the feasibility of localizing oxidation events at the interface with super-resolution microscopy using dSTORM and CAMPO-DNA PAINT.

Appendix

Acknowledgements

List of publications

Overview of completed training activities

About the author

Acknowledgements

I would like to extend my sincere thanks to all those who have taken the time to read my thesis. Whether we have worked together, shared enjoyable moments, or supported each other during my time in the Netherlands, I am genuinely grateful for the people I have encountered here. I hope we can stay connected and continue to cherish the relationships we have built. Thank you for being a part of my life in the Netherlands.

John, thanks for your continuous interest and involvement in my PhD project. Your contribution has been incredibly valuable, and I genuinely appreciate it. Your passion for the work has been inspiring and has kept me motivated throughout these past four years. Thank you for sharing your passion and for being a constant source of motivation. I also want to thank you for always staying positive and supportive, no matter what results I brought to the table.

Johannes, thanks for your invaluable guidance in my journey to becoming an independent researcher. I appreciate how you helped me adapt to the new environment here. Without your support, I would have struggled a lot. I also want to thank you for teaching me how to speak up and share my opinions. Additionally, thanks for encouraging me to stay positive about my research and myself. I appreciate you for cheering me up, especially during the last moments of my PhD.

Abbas, I couldn't handle my stress without your support. I am grateful for you being my colleague and friend. Our discussions about culture, food, gender, religion, and of course, research have been truly enjoyable, and I appreciate your honesty, which allows me to be completely open as well. I also appreciate Sana for all the amazing Iranian food and thoughtful presents. I am looking forward to hanging out with you, Sana and Mohammad Hasan more often! Thanks for being my paranymphs. **Mariska**, I appreciate your kindness and respectful attitude. As part of the same Mayo team, I have gained a lot of positive energy from you. I sincerely enjoyed the jokes and discussions we had. I hope we have more opportunities to meet in Ede as Ede residents. Thanks for being my paranymphs. **Martjin**, it was great fun to have group activities and dinner together. Thanks for all the helpful discussions during Friday's food microscopy meeting.

Project LICENSE members, I feel incredibly fortunate to have met all of you. **Lia**, thank you for conducting the first preliminary experiments on lipid oxidation with microscopy, which contributed to Chapter 3. **Sten**, your expertise in lipid oxidation taught me so much, and your motivation inspired me throughout our collaboration. I genuinely enjoyed working together, which resulted in Chapter 5. **Machi**, it's hard to believe that it has already been three years since that emotional moment in Utrecht when we cried together after our consortium meeting. All our memories have brought me so much joy, and I appreciate all the work-related discussions we had, which resulted in Chapters 4 & 6. **Vincent** (Boerkamp), thanks for our countless discussions and the long distances we walked together. My favourites were our never-ending conversations about philosophical topics, even more than discussing lipid oxidation. **Khoa**, thanks for our wonderful collaboration, which led to Chapter 5.

Looking forward to trying out recipes for Vietnamese cuisine. **Katherina**, I enjoyed our small talk in the FPE laboratory. Thanks for all your support related to experiments in FPE. I sincerely appreciated that we could share our feeling about PhD life during the last year. **Marie**, **Claire**, and **Karin**, thanks for all your support and kindness during the project meetings. I sincerely appreciate your positive attitude towards our research. **Heiner**, thanks for the nice collaboration and the fruitful feedback related to cryo-measurements. Also, thanks to **Eleni**, **Rayo**, **Silvia**, **Leonardo**, **Donny**, **Jianli**, **Remco**, **Peter**, **Hans-Gerd**, and **Jean-Paul** for the great discussions and support during the consortium.

Former BIPers, **Ahmad**, in the end, I didn't quit my PhD. Thanks for listening to my complaints during the first year of my PhD. I could enjoy my office life because of you. I always enjoyed the conversation during our walking journey from the office to home. Remember, Albert Heijn is too far. **Christo**, you were such a good office mate! Thanks for always welcoming me with your lively noise. It made me excited and gave me the energy to start my work. **Tanya**, I appreciate that we could share our thoughts, feeling, and experiences over the past four years. I will never forget the kindness you showed as a colleague, flatmate, and friend. **Netty**, I still deeply appreciate all the assistance you provided during my move from Korea to the Netherlands. It was a pleasure that everything went smoothly, quickly, and clearly. I hope you are currently enjoying your life after retirement. **Rob**, having a kind colleague like you was such a pleasure. Thank you for helping me use spectrometry during my first year. **Wouter**, **Henk**, **Koen**, **Mattia**, and **Du**, thanks all for making a good environment at BIP.

Current BIPers, **Sonja**, thanks for all the nice and fruitful discussions during the single molecule microscopy meeting. I was impressed by your passion for the work, which motivated me as well. **Benjamin**, thanks for being my experimental mate in room 0090. I enjoyed all of the random and philosophic conversations we had. **Chenyu** and **David**, it was a pleasure to have you as colleagues in room 0041 and every Wednesday meeting. **Emile**, thanks for organizing lab activities and making a good environment at BIP. **Peter**, **Klaudia**, and **Ludo**, thanks for organizing the nice lab activities. Our group become very active since you joined! I appreciate that I also could be motivated to exercise and run. **Laavanja**, our running period was relaxing and unforgettable. I still miss your previous house with my favourite balcony. The trip to Belgium was still thankful! Looking forward to travelling to many other places together. I also would like to thank our office mates, **Keshav**, **Sam**, **Lily**, and **Cleo**, for making the nice and cosy atmosphere. Of course, to the neighbour office mates, **Francesco**, **Dmytro**, **Dana**, and **Jarne**. **Lennart**, thanks for asking how many pages I wrote for my thesis several times. **John** (Philippi), thanks for all your technical support! You are the best technician in BIP. **Arjen**, thanks for your support related to microscopy. I could easily get used to using confocal microscopy, thanks to you. **Cor**, thanks for your support during my PhD. It was really helpful and saved my time a lot. You are one of the kind people in BIP who helped me feel comfortable at BIP. **Brenda**, thanks for all your support related to PhD graduation, visa, and my contract extension. I could manage things easily, thanks to you. **Ian**, thanks for making a good environment in the

laboratory. **Herbert**, I would like to thank you for signing off on the paperwork during the last four years. I also would like to thank **Frank**, **Morwarid**, **Camilla**, **Yanzhang**, **Annelies**, and **Jeremy** for making a nice atmosphere in BIP.

I would like to thank the people who guided my research life. **Geon sang Jeon**, thanks for guiding my research life first. I could get more interest in physics during my Bachelor's thanks to your excellent supervision during the course and research. **Yong-hee Lee**, thanks for suggesting my study in the Netherlands. I could get nice opportunities during my master's, and I sincerely appreciated all your advice in research and life. **Je-kyung Ryu** and lab members of the **Nano-photonics group**, thanks for your support during my master's. The optics-related techniques I learned from you led me to finish this journey.

I would sincerely appreciate all Koreans who visited Wageningen and also the Korean science community in the Netherlands. Thanks for your mental and physical support. Especially visiting researchers, **Minwoong Jung**, **Kwangsoo Jo**, and **Kongtae Lee**.

Dayoung, thanks for all the good memories we made together in Wageningen and Germany. I miss the period when we met almost every day and watched all the Harry Potter movies during Christmas. Looking forward to your PhD defense, and let's hang out more often after you're done. **Dawn**, Wageningen jumin! Thanks a lot for supporting me mentally and physically. I sincerely enjoyed our conversations and all the walking trips. **Jason**, you are the one who helped me a lot from the beginning of my PhD. Your kindness and humour bring happiness to people, including myself. Looking forward to seeing you in Korea. **Lim & Elias**, thanks for always supporting me. I could honestly share my feelings and thoughts with you. Biang Biang noodle is the best when we make the sound of biang biang. I sincerely appreciate your encouragement throughout my PhD journey.

Sander, **Fieke**, and **Thijmen**, thanks for always welcoming me when we visit Haren. I hope we can meet more often and do some fun activities together in the future with Thijmen! **Harm & Alja**, it was the first time I truly felt at home-home in the Netherlands. I sincerely enjoyed the weekends we spent together, which always made me feel so relaxed. Thanks for your kindness and all your support. **Vincent** (Paas), thanks for understanding my situation, even though you still haven't answered whether I was grumpy during my writing period. I was able to balance my work and life, even during my last year of the PhD, because you always cared for me. Thanks for your support and encouragement. I am looking forward to visiting Korea together.

Wageningen, *Su*

I also would like to thank the people in Korea who supported me a lot during my PhD. Since I moved to the Netherlands, I would appreciate having you in my life even more. **Haelim**, I enjoyed our monthly update call, which often exceeds easily 2 hours. I appreciate all your mental support. **Jisun**, you believe in me more than I actually do, and it makes me have my own belief in myself as well. Thanks for always boosting my confidence. **Yoon-a**, thanks for all the good memories we had during our time in Daejeon. I appreciate having many calls during my PhD as well. I would like to thank team Epikhigh, **Tablo**, **Mithra**, and **Tukutz**. I could live in a more lively way thanks to your music. The concert in Europe was one of the best moments I had.

Thanks to my high school friends who always supported me during my PhD. **Para**, thanks for calling immediately and listening to all my complaints when I have a hard time in the Netherlands. I still cannot forget our trips to Jeju, where both of us said that this was real happiness. **Eunji**, the period we lived as neighbours in Hangyang apartment during high school, texting every day during our Bachelor's, and when you lived in Canada, the frequency we talked was different, but it was always the same that we thought about each other. **Seoeun**, thanks for being there during awkward moments, like sleeping on the desk at school on the weekend. I still don't know you well, but I like you just as you are. **Juyeon**, thanks for always making me laugh. I appreciate your big heart and kindness even though you don't seem like that.

Minjoon, I am sometimes surprised by how many changes we have had since we first met in 2007. The funniest fact is that we are both in the Netherlands now. Living together with you during my writing period helped me a lot mentally and physically. Thanks a lot! **Boa**, since the time we were classmates in 2004, you always make me laugh, no matter what we do or where we are. I don't know how this is possible. I wouldn't be the current version of me if you were not in my life. Thanks for always being there for the events in my life. Lucky you, and lucky me!

Grandparents, thanks for taking care of me and my brother during our childhood. The love you gave us taught me how to love others. I feel sorry about my move. Please stay healthy and give me more time to see and love you. **Daeho**, you are my best friend and teacher during my childhood. Thanks for always being on my side when I need support. I appreciate all the good memories we had together, and it is the biggest luck in my life to have you as my brother. Looking forward to seeing your amazing new career. **Yeoju**, thanks for always welcoming me whenever I visit you. I hope we can spend more time together in the future. I am looking forward to meeting you and Daeho more often! **Father**, I appreciate that you always listen to me and are willing to change your attitude. I still cannot forget the moments when we sincerely start to share our experiences as adults. Thanks for considering me as an adult, not only your child. The memories we lived together in Daejeon, just you and me, are still greatly appreciated. **Mom**, I love you. Thanks for always being the biggest supporter in my life. You taught me how to be an independent person. Thanks for teaching me what the most important things in life are. I appreciate that I can share my day with you. I sincerely hope you enjoy life after retirement, and I will be your biggest supporter.

Seoul, 양수연

List of publications

This thesis:

(Chapter 2) ten Klooster, S.*, Boerkamp, V.*, Lazaridi, E.*, **Yang, S.***, Takeuchi, M.*, Berton-Carabin, C., Schroën, K., Janssen, H.G., Friedrich, H., Hohlbein, J., van Duynhoven, J., & Hennebelle, M. (2022). Lipid oxidation in food emulsions: Analytical challenges and recent developments. Lipid Oxidation in Food and Biological Systems: A Physical Chemistry Perspective, 3-29.

(Chapter 3) **Yang, S.**, Verhoeff, A. A., Merkx, D. W., van Duynhoven, J. P., & Hohlbein, J. (2020). Quantitative spatiotemporal mapping of lipid and protein oxidation in mayonnaise. Antioxidants, 9(12), 1278.

(Chapter 4) **Yang, S.***, Takeuchi, M.*, Friedrich, H., van Duynhoven, J. P., & Hohlbein, J. (2023). Unravelling mechanisms of protein and lipid oxidation in mayonnaise at multiple length scales. Food Chemistry, 402, 134417.

(Chapter 5) **Yang, S.***, ten Klooster, S.*, Nguyen, K.A., Hennebelle, M., Carabin, C., Schroën, K., van Duynhoven, J. P., & Hohlbein, J. Droplet size dependency and spatial heterogeneity of lipid oxidation in WPI-stabilized emulsions (to be submitted)

(Chapter 6) **Yang, S.***, Takeuchi, M.*, Friedrich, H., van Duynhoven, J. P., & Hohlbein, J. Adapting cryogenic correlative light and electron microscopy (cryo-CLEM) for food oxidation studies (to be submitted)

Other publication:

Lee, J.*, **Yang, S.***, Lee, J., Choi, J. H., Lee, Y. H., Shin, J. H., & Seo, M. K. (2020). Extraordinary optical transmission and second harmonic generation in sub–10-nm plasmonic coaxial aperture. Nanophotonics, 9(10), 3295-3302.

Martens, K. J., Jabermoradi, A., **Yang, S.**, & Hohlbein, J. (2021). Integrating engineered point spread functions into the phasor-based single-molecule localization microscopy framework. Methods, 193, 107-115.

Jabermoradi, A., **Yang, S.**, Gobes, M. I., Van Duynhoven, J. P., & Hohlbein, J. (2022). Enabling single-molecule localization microscopy in turbid food emulsions. Philosophical Transactions of the Royal Society A, 380(2220), 20200164.

* These authors contributed equally

Overview of completed training activities

Discipline specific activities	Organizer	Year
Advanced Food Analysis	VLAG	2019
Applied Biocatalysis	VLAG	2019
SMLMs 2019	Delft	2019
Spray drying	Danone	2019
Dutch biophysics	NWO	2020
3rd International Symposium on Lipid Oxidation and Antioxidants	EFL	2020
Multiscale workshop	WUR	2021
Reaction kinetics in food science	VLAG	2021
Les Houches winter school "Fluorescence Markers for advanced microscopy"	Les Houches School of Physics	2022
Europe-Korea Conference on Science and Technology	EKC	2022
Single Molecule Localization Microscopy Symposium	SMLMS	2022

General courses	Organizer	Year
VLAG PhD Week	VLAG	2019
The essentials of Scientific writing & Presenting	WGS	2019
Competence Assessment 3	WGS	2019
Scientific Writing	WGS	2020
An Introduction to LaTeX	VLAG	2020
Introduction to R	VLAG	2021
The Choice: Un-box your PhD process & take charge of your performance	WGS	2021
Career Orientation	WGS	2022

Other activities	Organizer	Year
Preparation of research proposal	WUR - BIP	2019
Work package 3 group meetings	WUR, TU/e	2019-2022
Food microscopy group meeting	WUR - BIP	2019-2022
Single molecule microscopy group meeting	WUR - BIP	2021-2022
LICENSE project consortium	WUR, Unilever, Danone, TU/e	2018-2021
Danone project meeting	WUR, Danone	2021

About the author

Suyeon Yang was born on the 17th of September, 1992, in Jeolla-do, South Korea. In 2016, she obtained her BS in Physics at Ewha Womans University in Seoul, South Korea, after completing her graduation project on 'Calculating the edge effect on the bending of graphene nanoribbons by in-plane bending' under the supervision of Prof. Dr. Gun Sang Jeon.

She continued her studies with an MSc in Physics at KAIST in Daejeon, South Korea. During her studies, she worked on fabricating a 3D plasmonic nano-antenna and building a free-space optical setup for measuring second harmonic generation and transmission signals from a nano antenna. In 2018, she completed her MSc thesis entitled 'Optical trapping of nanometer-sized particles using a 3D plasmonic cavity' under the supervision of Prof. Dr. Yong-Hee Lee.

In November 2018, Suyeon moved to the Netherlands to start her PhD project at the Laboratory of Biophysics (BIP) under the supervision of Prof. Dr. John PM van Duynhoven and Dr. Johannes Hohlbein, and the results of this project are presented in this dissertation.